Spectroscopy of neutron-rich germanium and krypton isotopes - A quest of triaxiality

Spektroskopie neutronenreicher Germanium- und Kryptonisotope - Eine Suche nach Triaxialität
Zur Erlangung des Grades eines Doktors der Naturwissenschaften (Dr. rer. nat.)
genehmigte Dissertation von Marc Lettmann, M.Sc. aus Darmstadt
Tag der Einreichung: 01. Februar 2018, Tag der Prüfung: 16. April 2018
2018 — Darmstadt — D 17

1. Gutachten: Prof. Dr. Dr. h.c. Norbert Pietralla
2. Gutachten: Prof. Dr. Thomas Aumann

TECHNISCHE
UNIVERSITÄT
DARMSTADT

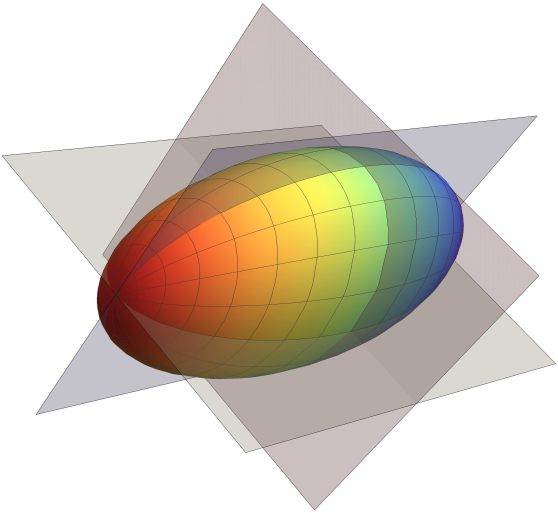

Fachbereich Physik
Institut für Kernphysik
AG Pietralla

Bundesministerium
für Bildung
und Forschung

under grant No.
05P15RDFN1

Spectroscopy of neutron-rich germanium and krypton isotopes - A quest of triaxiality
Spektroskopie neutronenreicher Germanium- und Kryptonisotope - Eine Suche nach Triaxialität

Genehmigte Dissertation von Marc Lettmann, M.Sc. aus Darmstadt

1. Gutachten: Prof. Dr. Dr. h.c. Norbert Pietralla
2. Gutachten: Prof. Dr. Thomas Aumann

Tag der Einreichung: 01. Februar 2018
Tag der Prüfung: 16. April 2018

Darmstadt — D 17

Version: 27. April 2018

Bitte zitieren Sie dieses Dokument als:
URN: urn:nbn:de:tuda-tuprints-73821
URL: http://tuprints.ulb.tu-darmstadt.de/7382

Abstract

This work covers the spectroscopic analysis of ^{84,86,88}Ge and ^{94,96}Kr isotopes populated by different reactions within the SEASTAR campaign 2015. The experimental setup and the data analysis are described in detail. This analysis includes necessary functionality checks and calibrations of the detectors along the beam line.
In-flight γ-ray spectroscopy of ^{84,86,88}Ge was performed after various knock-out reactions. γ-spectroscopy of neutron-rich ^{88}Ge was performed for the first time. The Doppler-corrected γ-ray spectra are analyzed with simulated lineshapes of occurring transitions. In total 16 transitions are observed ten of which so far unknown. New level schemes for ^{86,88}Ge are proposed based on the observed transition intensities and systematics of neighboring Ge isotopes.
The obtained level schemes are compared to state-of-the-art theoretical calculations. The assignment of a 3^+ state of ^{86}Ge agrees with new shell model and SCCM predictions. The agreement to the level orderings from the collective model by Davydov and co-workers points to an amount of rigid triaxiality in ^{86}Ge. This is the first indication of rigid triaxiality in an unstable, neutron-rich nucleus.
In addition, an analysis of reaction cross sections, as well as cross sections for the excitation of a particular state is performed. This data set represents one of the first results for this newly-accessible region of the nuclear chart.
Furthermore, ^{84,86}Ge and ^{94,96}Kr are investigated after (p,p') reactions, which excite different states than the knock-out reactions. These states are candidates for octupole 3^- states, which are the first benchmark for the octupole degree of freedom in this exotic region. The obtained (p,p') cross sections of the 2_1^+ states from ^{94,96}Kr are compared to the transition strength known from literature based on the deformation length.

Zusammenfassung

Diese Arbeit behandelt die spektroskopische Analyse von ^{84,86,88}Ge und ^{94,96}Kr Isotopen, die durch verschiedene Reaktionen im Rahmen der SEASTAR Kampagne 2015 bevölkert wurden. Der experimentelle Aufbau und die Analyse werden detailliert beschrieben. Diese Analyse beinhaltet die nötigen Funktionstests und Eichungen der Detektoren entlang der Strahlführung.
γ-Spektroskopie von ^{84,86,88}Ge wurde nach verschiedenen Knock-Out-Reaktionen im Flug durchgeführt. Zum ersten Mal wurde neutronenreiches ^{88}Ge spektroskopiert. Die Doppler-korrigierten γ-Spektren wurden durch simulierte Linienformen der auftretenden Übergänge analysiert. Insgesamt wurden 16 Übergange beobachtet, zehn dieser Übergänge waren bisher unbekannt. Begründet durch die beobachteten Intensitäten und die Systematiken der benachbarten Germaniumisotope werden neue Levelschemata für ^{86,88}Ge vorgeschlagen.
Die erhaltenen Levelschemata werden mit modernsten theoretischen Berechnungen verglichen. Die Zuweisung eines 3^+ Zustands von ^{86}Ge stimmt mit neuen Schalenmodell- und SCCM-Vorhersagen überein. Die Übereinstimmung zu den Zustandsanordnungen des kollektiven Modells von Davydov und Kollegen weist auf einen Grad der Triaxialität in ^{86}Ge hin. Dies ist der erste Hinweis auf starre Triaxialität in einem instabilen, neutronenreichen Kern.
Zusätzlich wird eine Analyse der Reaktionswirkungsquerschnitte und der Wirkungsquerschnitte für die Anregung eines bestimmten Zustands durchgeführt. Dieser Datensatz repräsentiert eine der ersten Ergebnisse in dieser neu zugänglichen Region der Nuklidkarte.
Außerdem werden ^{84,86}Ge und ^{94,96}Kr nach (p,p')-Reaktionen, die im Vergleich zu Knock-Out-Reaktionen andere Zustände anregen, untersucht. Diese Zustände sind Kandidaten für 3^- Oktupolzustände, die der erste Bezugspunkt für den Oktupolfreiheitsgrad in dieser exotischen Region sind. Die erhaltenen (p,p')-Wirkungsquerschnitte der 2_1^+ Zustände von ^{94,96}Kr werden mit den aus der Literatur bekannten Übergangsstärken mit Hilfe der Deformationslänge verglichen.

Contents

1 Introduction

Rutherford discovered a massive nucleus in the center of the atom in 1911 [1]. This nucleus covered less than 0.001% of the atoms volume and had $99,9\%$ of its mass. Nowadays it is known that the word "nucleus" describes an object composed of one up to ~ 300 protons and neutrons with varying composition. The size of a nucleus is in the order of $1\text{ fm} = 10^{-15}$ m, way beyond the scale of every days life and difficult to comprehend. All the nuclear components, up to some hundred protons and neutrons, interact primarily via the Coulomb and nuclear force. The prepended description illustrates the complexity of the task nuclear physics accepted. Consequently, it is hardly surprising that no uniform, reliable description of this complex many-body problem on small scale is available.

In order to solve the many-body problem it is essential to describe the nuclear force acting between the nucleons. Today it is a well established fact that the nuclear force is a residual part of the strong force. Considerable progress in deriving the nuclear force from the theory of quantum chromodynamics (QCD) [2], covering the regime of quarks and gluons, is made. The nuclear force is obtained from QCD within the lattice QCD [3] or the chiral effective field theory (χEFT) [4]. One advantage of these theories is that they allow to derive theoretical uncertainties. In contrast to this, the nuclear force can be derived from phenomenological potentials extracted from experimental nucleon-nucleon scattering data [5, 6]. As soon as the nuclear force is defined, the nuclear many-body problem can be calculated. At this point theories apply different approaches discussed in the following.

For small nucleon number ($A \lesssim 16$) the many-body problem can be solved using ab initio methods without approximations [7]. No exact description of the many-body problem is possible for medium-mass nuclei, therefore a renormalisation [8] of the interaction and importance truncation [9] or coupled cluster methods [10] are introduced to reduce the Hilbert space. The shell model applying phenomenological interactions extracted from experimental data is capable of a good description of nuclei near closed shells [11].

Different approaches to the many-body problem are phenomenological models like the Quasiparticle Phonon Model (QPM) [12], the self-consistent mean-field approach[13], collective geometrical models (e.g. by Bohr and Mottelson [14] or Davydov and co-workers [15]), or the algebraic Interacting Boson Model (IBM) [16]. These models are applied to describe specific phenomena of nuclear matter.

To ensure the validity and the good predictive power of theoretical calculations comparisons to experimental results are crucial. Different phenomena have been discovered, serving as a promising test ground for nuclear models, e.g., the collective behavior of nuclei in general [14, 15], and the formation of mixed symmetric states by an out-of-phase motion of protons and neutrons [17]. Furthermore, even-even nuclei possess an ordinary sequence of their first excited states, which are mostly $J = 2^+$ and $J = 4^+$. Remarkable results are obtained regarding the energy of the 2^+ state and the ratio $R_{4/2}$ of the 2^+ and 4^+ level energies. Both quantities are shown in figure 1.1 across the nuclear chart. Clear patterns of the underlying shell structure arise, which lead to the well-known "magic numbers" (2,8,20,28,50,82) for protons and neutrons [19, 20]. This basic information allows for important conclusions on nuclear properties, e.g., an increase of collectivity and an onset of deformation is reflected by a drop of 2_1^+ energies and a rise of $R_{4/2}$ ratios.

New Radioactive Ion Beam (RIB) facilities allow to investigate nuclear properties of exotic nuclei far from the valley of stability, formed by those isotopes which are stable with respect to β decay. A broad variety of RIBs are produced by different facilities, e.g., GSI (Germany), RIKEN (Japan), ISOLDE/HIE-ISOLDE (Switzerland), GANIL (France), or NSCL (USA) while additional facilities aiming for higher RIB intensities and energies are under construction, e.g., FRIB (USA), SPES (Italy), or FAIR (Germany). These RIBs are obtained either by ISOL or in-flight production techniques. However, the production rate of RIBs decreases strongly for increasing isospin. Therefore, the first nuclear spectroscopy measurements of exotic nuclei are commonly limited to the first few excited states.

An example for a large-scale experimental campaign aiming to measure the low-spin spectra of various exotic nuclei is the Shell Evolution And Search for Two-plus energies At RIBF (SEASTAR) campaign [21]. It intends to measure all 2_1^+ energies up to $Z = 40$ (Zr) with presently available ^{70}Zn and ^{238}U primary beam intensities, as shown in figure 1.2. Thus, the SEASTAR campaign covers many different topics focused on neutron-rich nuclei. The central questions addressed are [21]:

- the significance of the $N = 34$ shell gap below ^{54}Ca (^{52}Ar) and the correlations beyond (^{56}Ca),
- exploring the low-Z shore of the $N = 40$ "Island of Inversion" (^{60,62}Ti) and the evolution of collectivity beyond $N = 40$ (^{66}Cr, ^{72}Fe),
- the question if ^{78}Ni is doubly-magic,
- the orbital migration beyond $N = 50$ (^{82,84}Zn, ^{86,88}Ge, ^{90,92}Se) and the domination of collectivity at $N \geq 60$ (^{94}Se, ^{98,100}Kr)
- and the evidence for a $N = 70$ sub-shell effect (^{110}Zr).

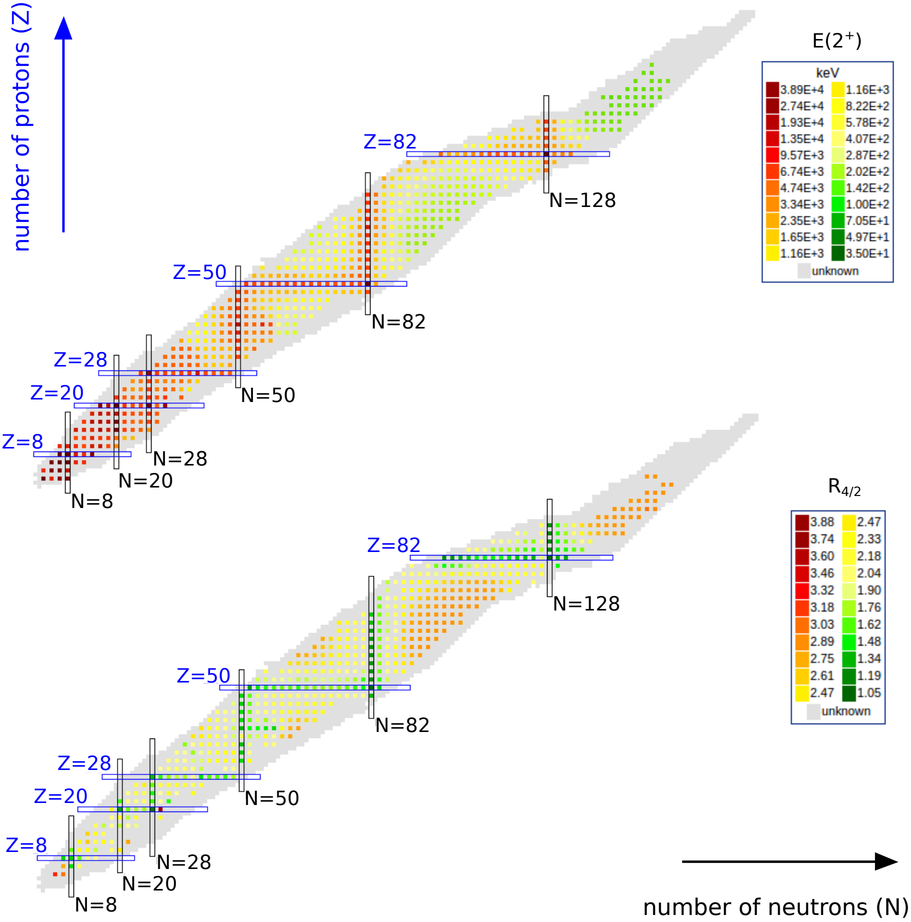

Figure 1.1.: Illustration of the $E(2^+)$ (top) and $R_{4/2} = E(4^+)/E(2^+)$ (bottom) across the nuclear chart. The image is taken from [18] and slightly modified.

The SEASTAR campaign was split up in three sub-campaigns treating various mass regions conducted in three different years. The first sub-campaign took place in May 2014 and focused on the spectroscopy of ^{66}Cr, ^{70,72}Fe and ^{78}Ni. In April and May 2015 the second sub-campaign took place focusing on the spectroscopy of ^{82,84}Zn, ^{86,88}Ge, $^{90-94}$Se, ^{98,100}Kr and ^{110}Zr. This sub-campaign is referred to as SEASTAR 2015 in the following work. Finally, the third sub-campaign took place

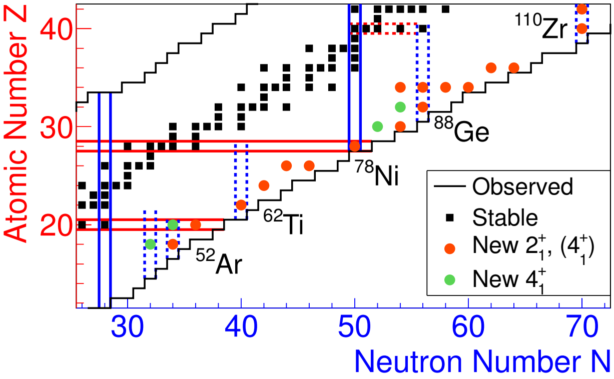

Figure 1.2.: $E(2^+)$ and $E(4^+)$ measurements foreseen within the SEASTAR campaign.

in May 2017 and focused on the spectroscopy of ^{52}Ar, ^{56}Ca and ^{62}Ti. The spectroscopic data of ^{84,86,88}Ge and ^{94,96}Kr analyzed in this work was collected in the SEASTAR campaign 2015.

As mentioned before the orbital migration beyond $N = 50$ and the onset of collectivity are central questions which need to be answered for the germanium isotopic chain. Furthermore, triaxial nuclear features are expected for ^{86,88}Ge. A short introduction into both topics is given in the following.

Evolution of the $N = 56$ sub-shell closure

The N_pN_n scheme [22, 23] describes the collectivity- and deformation-driving part of the valence proton-neutron interaction by the product of the valence protons (N_p) and valence neutrons (N_n). This simple relation allows to compare systematic behavior, e.g., the first 2^+ level energies $E(2_1^+)$, in a given mass region. A strong onset of collectivity is expected beyond the shell closures $Z = 28$ and $N = 50$ for an increasing number of valence nucleons within the N_pN_n scheme.

It was previously explained that shell closures are characterized by a large $E(2_1^+)$ compared to the neighboring isotopes. The evolution of $E(2_1^+)$ from $Z = 32$ (Ge) to $Z = 40$ (Zr) for $N = 50$ towards $N = 60$ is shown in figure 1.3. For the zirconium isotopes, the $N = 50$ shell closure and the $N = 56$ sub-shell closure are well pronounced, as is evident by the large $E(2_1^+)$, in contrast to the strontium isotopes where no increased $E(2_1^+)$ is observed at $N = 56$. For both isotopes the dominance of collectivity is at $N = 60$. For the krypton isotopic chain a slight increase in 2_1^+

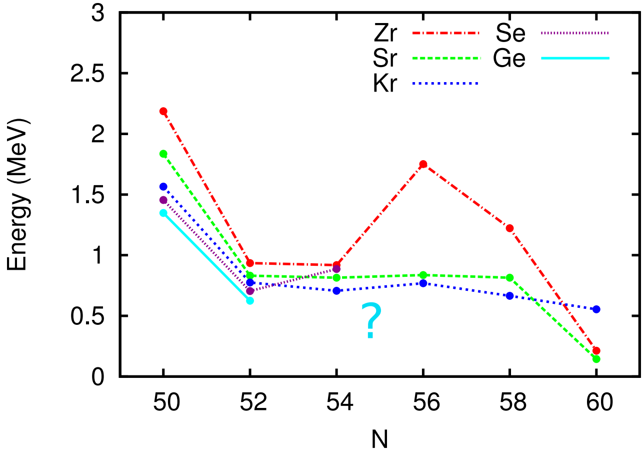

Figure 1.3.: Behavior of the 2_1^+ level energies for the isotopic chains of Zr ($Z = 40$) [24, 25, 26, 27, 28, 29], Sr ($Z = 38$) [24, 25, 26, 27, 28, 30], Kr ($Z = 36$) [24, 25, 26, 27, 30, 31, 32], Se ($Z = 34$) [31, 33] and Ge ($Z = 32$) [31, 34].

energy is observed at the sub-shell closure. Afterwards $E(2_1^+)$ decreases systematically leading to a continuous increase of collectivity.

Open questions which need to be addressed are whether the sub-shell closure remains for the lighter selenium and germanium isotopes and where the dominance of collectivity arises. Within this work $N = 56$ for germanium is reached and its stability is directly tested.

Triaxiality

The spectroscopic results and predictions from theory for the Ge isotopic chain inspire lively discussions of the triaxial features [35, 36, 37, 38, 39]. Two different collective models which included a breaking of axial symmetry of the Bohr Hamiltonian [14] are competing in this region. These models introduce the triaxial deformation parameter γ, ranging from 0° (prolate shape) to 60° (oblate shape), and the axial elongation β. A deformation parameter $\gamma = 30°$ reflects the maximum of triaxiality. On one hand, the rigid triaxial rotor model by Davydov and co-workers [40] considers a potential energy surface with a well-defined minimum for a certain value of γ. On the other hand, the model by Wilets and Jean [41] treats the potential energy surface independent of γ, which is referred to as the γ-soft case.

Triaxiality is a well known feature, which covers various regimes of angular momentum. At high spin-quantum number, quasiparticle configurations lead to the formation of triaxial superdeformed bands that exhibit so-called wobbling modes [42, 43, 44]. For intermediate spin-quantum number, discussions are stimulated by chirality of odd-odd nuclei, based on the spin of the unpaired proton and neutron and the rotational axis of the remaining core which needs to be triaxial [45, 46, 47]. At low spins, the nuclei are typically described by a broad minimum in γ, corresponding to the before mentioned γ-soft case. This type of nuclei are closely related to the $O(6)$ dynamical limit of the IBM, with the best known example being ^{196}Pt [48, 49, 50].

The low-spin spectra formed by γ-soft nuclei and rigid triaxial rotors have rather similar characteristics (compare figure 1.4). However, significant differences occur for the energy spacing between the odd and even members of the γ band (blue states in figure 1.4). In the case of a γ-soft nucleus, the odd-spin levels are closer to the higher-lying even-spin levels, while the odd-spin levels are closer to the lower-lying even spin levels in the case of a rigid triaxial rotor. This relative location of odd and even spin levels is usually referred to as staggering [21,22]. So far, the only experimental evidence for a significant degree of rigid triaxiality in the ground state, for medium-heavy $A < 100$ nuclei, is provided by Toh *et al.* [51] for ^{76}Ge. This work aims at providing additional insights into the rare phenomenon of rigid triaxiality in nuclear matter.

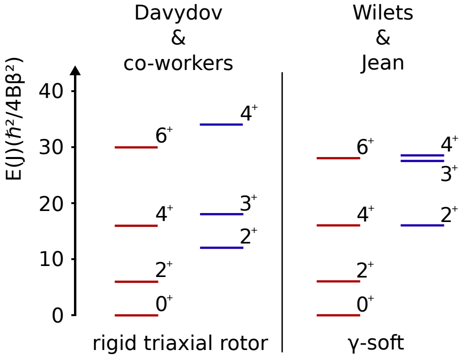

Figure 1.4.: Comparison of the low-spin spectra within the model of Davydov and the model of Wilets and Jean.

In the following, the basic principles and a brief introduction to the theoretical models needed for the interpretation of the data are given in sections 2 and 3. The experimental setup of the SEASTAR campaign 2015 is described in section 4. Section 5 presents required operational checks and the calibration of the setup. Furthermore, important analysis steps, e.g., the applied Doppler correction, the simulation of the lineshape, or the fitting procedure, are described. The obtained experimental results are shown in section 6, while a comparison to theoretical predictions and a discussion of the findings is presented in section 7. Finally, a summary of the work and an outlook are given in section 8.

2 Basic principles

The content of the following section is described in many text books like [52, 53, 54, 55, 56]. The information, especially the mathematic descriptions, are taken from these references and modified to suit the main emphasis of this work.

2.1 Nuclear reactions

Considering energetic particles from an accelerator impinging on target material, various nuclear reactions can take place. Commonly, such reactions are denoted as

$$X(a,b)Y. \tag{2.1}$$

Here, X, a denote incident particles and Y, b describe the outgoing particles. If Y and b are in their ground state and $X = Y$, $a = b$ *elastic scattering* takes place. This is the simplest nuclear reaction in which the projectiles interact with a localized force field, while the particles do not lose kinetic energy. Beside such reactions *direct* or *compound reactions* may occur. A *compound reaction* is characterized by an intermediate nucleus, which is formed out of X and a. The resulting outgoing channel differs from the incident channel and is populated when the compound nucleus de-excites. In contrast to such a multi-step reaction a *direct reaction* can also take place. *Direct reactions* occur in a short period of contact between the particles in a peripheral collision. An example for this reaction type is *inelastic scattering*. Here, one of the outgoing particles Y, b is in an excited state. In principle any state can be populated by *inelastic scattering*, but the excitation of collective states is strongly favored [54]. Another example for a *direct reaction* is a *transfer reaction*. The knock-out or pickup of a small number of nucleons characterize these reactions. In contrast to equation 2.1 more than two reaction products are observed in the outgoing channel of a *knock-out reaction*. In case of a *pickup reaction* a nucleon from X or a is transfered to Y or b. The latter two processes selectively excite states that are related to initial states of X or a by adding or subtracting nucleons.

Excited nuclei considered in this work are populated by *inelastic scattering* off a proton target or by *knock-out reactions* of different type.

2.1.1 Proton inelastic scattering

The characteristics of proton inelastic scattering become rather evident when comparing it to Coulomb excitation [57]. Coulomb excitation describes the interaction of nuclei within their reaction partner's electromagnetic field, which is created by the protons inside the target and the projectile nucleus. Since neutrons do not carry electrical charge the Coulomb interaction is only sensitive to the protons inside the nuclei. To investigate the neutrons of the target and the projectile a different scattering process has to be considered. This scattering process is the inelastic scattering. As mentioned before it is a peripheral collision involving neutrons and protons. Therefore, both nuclei interact with the electromagnetic and the nuclear force. While the electromagnetic force is well known and can be described precisely, the description of the nuclear force relies on nuclear models of the interaction potential. A common approach is the optical model which is described in the following.

The optical model

The optical model describes the scattering potential by a complex nucleon optical potential. Many different expressions are used for this nucleon optical potential. This chapter is based on [58], while some alternative descriptions can be found in literature [59, 60, 61, 62].

Over the years, a standard form of the optical potential was formed. This potential consists of

$$
\begin{aligned}
U_{opt}(r) = & \\
& + V_C(r) && \text{the Coulomb term,} \\
& - V f_V(r) && \text{the real volume term,} \\
& - 4 a_i V_s \frac{d}{dr} f_V(r) && \text{the real surface term,} \\
& + d_{so} \vec{l} \cdot \vec{s} V_{so} \frac{1}{r} \frac{d}{dr} f_V(r) && \text{the real spin-orbit term} \\
& - i W_v f_W(r) && \text{the imaginary volume term,} \\
& + 4 a_i i W_s \frac{d}{dr} f_W(r) && \text{the imaginary surface term, and} \\
& - d_{so} \vec{l} \cdot \vec{s} W_{so} \frac{1}{r} \frac{d}{dr} f_W(r) && \text{the imaginary spin-orbit term.}
\end{aligned}
\tag{2.2}
$$

Here, $d_{so} = (\hbar/m_\pi c)^2 \approx 2\ \mathrm{fm}^2$ denotes the spin-orbit constant and m_π is the pion mass. $V_C(r)$ is described by a point charge with a uniformly charged sphere of the radius R_C:

$$V_C(r) = \begin{cases} \left(\frac{3}{2} - \frac{r^2}{2R_C^2}\right) \frac{Z_p Z_t e^2}{R_C} & , r \leq R_C, \\ \frac{Z_p Z_t e^2}{r} & , r > R_C, \end{cases} \tag{2.3}$$

where Z_t and Z_p are the charge of the target and the projectile, respectively. The form factors $f_i(r)$ are described by a Woods-Saxon function

$$f_i(r) = \frac{1}{1 + e^{\frac{r-R_i}{a_i}}} \qquad , i = V, W, \tag{2.4}$$

with the radii R_i and the diffuseness parameter a_i. The index V denotes the real part of the optical potential describing the elastic scattering of the particles, while the imaginary part indicated by the index W considers inelastic scattering by absorption.

The parameters of the optical potential can be obtained by a fit of experimental cross sections from elastic scattering. Since small changes of the parameters have been observed for varying proton and neutron number, comprehensive analyses have been performed. Examples for such a parametrization is the Beccheti-Greenless model [63] and the Koning-Delaroche model (KD02) [64]. While the Beccheti-Greenless model is restricted to $A > 40$ and energies < 50 MeV, the Koning-Delaroche model is valid for $24 \leq A \leq 209$ and energies between 1 keV and 200 MeV.

2.2 Excited nuclear states

A physical systems prefers its energetic lowest states. For this reason, an excited nucleus wants to release energy, which can be attained by the emission of massive particles (proton, neutron, α, ...) and (or) γ radiation. In the following, only the de-excitation via γ-ray emission is considered. This is illustrated in figure 2.1. The initial (i) and final (f) states are characterized by their spin J and parity π. After a distinctive time the de-excitation of the state J_i^π takes place. For this characteristic time two notations are used. The mean-lifetime τ and the half-life $T_{1/2}$ of the state, which are connected by $T_{1/2} = \tau \ln 2$. The energy of the emitted γ radiation is given by $E_\gamma = E_i - E_j$. The emitted photon is characterized by its multipole order l and if its nature is magnetic (M) or electric (E). The underlying radiation field

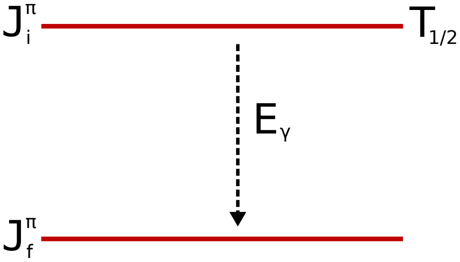

Figure 2.1.: Simple level scheme.

corresponds to an oscillating classical 2^l pole. The possible l and the radiation character σ of a transition are defined by the quantum-mechanical selection rules:

- multipole order l: $|J_i - J_f| \leq l \leq J_i + J_f$, with $l > 0$
- electric character $\sigma = E$: $\pi_i \cdot \pi_f = (-1)^l$
- magnetic character $\sigma = M$: $\pi_i \cdot \pi_f = (-1)^{l+1}$

If a γ-ray transition is forbidden due to the quantum-mechanical selection rules, the excitation energy can be transfered to the shell electrons, which are than emitted instead of the photon. This process is called internal conversion.

In the following, it is demonstrated why such γ radiation is nearly always characterized by low multipoles. Here the intrinsic spin of the photon is neglected. The angular momentum is given by $\vec{l} = \vec{r} \times \vec{p}$, while the linear momentum carried by a photon is $p = E_\gamma/c$. Thus, the maximum angular momentum in units of $\hbar$ is given by $l = E_\gamma R/\hbar c$. Considering γ radiation of typical low-spin spectra with a transition energy of 1 MeV and $l = 1$. With $\hbar c \approx 200$ MeV fm the γ radiation is emitted at a distance of $R \approx 200$ fm from the center of the nucleus. Since the nuclear radius $R \approx 1.3$ fm $A^{1/3}$ is ~ 6 fm for a medium-mass nucleus with $A = 100$ it follows that the electromagnetic de-excitations seem to occur on the tail of nuclear wave functions extending out to large distances. Furthermore this illustrates, that higher multipoles ($l > 2$) are extremely unlikely. Beside this, the transition probability for electric radiation is roughly an order of magnitude higher than the probability of magnetic radiation. Therefore, it is generally assumed that transitions are $E1$, $M1$, and $E2$ if the multipolarities are unknown [55].

The transition probability $\lambda(\sigma l)$ assuming that the de-excitation takes place only by photon emission of multipole l and radiation character σ is given by:

$$\lambda(\sigma l) = \frac{8\pi(l+1)}{\hbar l\left[(2l+1)!!\right]^2}\left(\frac{E_\gamma}{\hbar c}\right)^{2l+1} B\left(\sigma l; J_i \rightarrow J_f\right) \tag{2.5}$$

with

$$B\left(\sigma l; J_i \rightarrow J_f\right) = \frac{1}{2J_i+1}\left|\langle\Psi_f||\mathscr{O}_{\sigma l}||\Psi_i\rangle\right|^2. \tag{2.6}$$

The reduced transition strength $B\left(\sigma l; J_i \rightarrow J_f\right)$ represents a central quantity to characterize γ-ray transitions. It is proportional to the reduced matrix element $\langle\Psi_f||\mathscr{O}_{\sigma l}||\Psi_i\rangle$ between the i and f states. $\mathscr{O}_{\sigma l}$ denotes the transition operator for σl radiation.

It is beneficial to define a standard such that the magnitude of a $B(\sigma l)$ can be assessed to be strong (collective) or not. Introducing the Weisskopf unit (W.u.) [65] achieves this standard. It is an estimate for a transition involving only one particle whose radial wave function is approximated by a constant. Values which are large compared to 1 W.u. are considered to correspond to transitions in which many particle participate, thus they are called collective. The Weisskopf estimations for $B(E1)$, $B(M1)$, and $B(E2)$ are given in table 2.1.

Table 2.1.: Weisskopf estimates for low multipole orders. The information is taken from [66]

σl	$B_W(\sigma l)$
$E1$	$6.446 \times 10^{-2} A^{2/3}\ \mathrm{e}^2\mathrm{fm}^{2\lambda}$
$M1$	$1.790\ (\mu_N/c)^2\mathrm{fm}^{2\lambda-2}$
$E2$	$5.940 \times 10^{-2} A^{4/3}\ \mathrm{e}^2\mathrm{fm}^{2\lambda}$

2.3 Neutron and proton transition matrix elements

The concept of different matrix elements for neutrons M_n and protons M_p and their ratio is described in [67, 68, 69] and the following description is based on this literature. Each of the matrix elements for protons and neutrons can contribute differently to the excitation of a nuclear state. Since, hadronic scattering probes both the neutrons and the protons, while Coulomb scattering only probes

the protons (as discussed in section 2.1.1) the difference of M_n and M_p can be obtained by comparison of a Coulomb measurement and e.g. a (p,p') experiment.
In order to compare the quota of M_n and M_p, the ratio M_n/M_p is calculated, while

$$M_{n(p)} = \int \rho_{n(p)}(r) r^{l+2} dr. \tag{2.7}$$

Here, $\rho_{n(p)}(r)$ denote the neutron and proton transition densities and l is the multipole order. Furthermore, the matrix element is related to the $B(El)$ value by

$$B(El; J_i \rightarrow J_f) = \frac{(M_{n(p)})^2}{2J_i + 1}. \tag{2.8}$$

As shown later, the $B(E2)$ can be related to the deformation length $\delta = \beta R_0 A^{1/3}$ (compare equation 3.12) within a collective model. By comparison of the deformation length obtained from a Coulomb excitation experiment δ_{em} and a (p,p') experiment $\delta_{p,p'}$ the M_n/M_p ratio is given by [68]

$$\frac{M_n}{M_p} = \frac{N}{Z}\left(\frac{\delta_{p,p'}}{\delta_{em}} + \frac{Z b_p^p}{N b_p^n}\left(\frac{\delta_{p,p'}}{\delta_{em}} - 1\right)\right), \tag{2.9}$$

where b_p^p and b_n^p denote the proton-proton and proton-neutron interaction strength. Equation 2.9 shows that M_n/M_p is equal to $N/Z \times \delta_{p,p'}/\delta_{em}$ corrected by a factor dependent on the sensitivity of the scattering process. This correction depends on the projectile energy and varies between $b_p^p/b_p^n = 3$ for $10-50$ MeV protons and $b_p^p/b_p^n = 0.95$ for 1 GeV protons [68].
If the nucleus is considered as a homogeneous proton-neutron liquid, an isoscalar excitation is expected with $M_n/M_p = N/Z$. This simple picture may not hold for nuclei with closed proton (neutron) shell, since the protons (neutrons) forming a closed shell have $M_p(M_n) = 0$. However, it is observed that core polarization weakens the effective isovector excitations [70]. If a significant difference of the ratios M_n/M_p to N/Z is observed this is anyhow an evidence that shell effects are substantial.

3 Theories

This section provides the basic ideas from different nuclear models, which will be applied in the discussion of this work. Starting with the shell model described in section 3.1. Its great success is the explanation of nuclear structure around closed shells. Afterwards, two collective models are introduced. These models are the first attempts to explore nuclear structure between nuclear shell closures, in a region were collective phenomena become more important and the shell model valence space is limited due to computational limits. Two examples are given, namely the models by Bohr and Mottelson in section 3.2.1 and the model by Davydov and co-authors in section 3.2.2. Section 3.3 describes a state-of-the-art mean-field calculation. This chapter closes with the description of the IBM-2, which is a different attempt to tackle the question of nuclear structure by an approach based on group theory.

3.1 Shell model

This section is close to the description of the shell model by [55]. For more detailed informations the author refers to this reference.
Starting from the central problem of nuclear physics, which is the description of the individual nucleons motion and interactions between pairs of nucleons in such way that it is capable to describe the observed nuclear excitation from this basis, an exemplary Hamiltonian is given by

$$H = T + V = \sum_{i=1}^{A} \frac{\vec{p}_i^{\,2}}{2m_i} + \sum_{i>k=1}^{A} V_{ik}(\vec{r}_i - \vec{r}_k). \tag{3.1}$$

Here, V has the form of a nucleon-nucleon interaction and is a function of the three relative position coordinates of each of the particles. Therefore, it has $3A$ position coordinates and becomes extremely complex for large nuclei. To solve this, the issue is approached by a different manner. Instead of a 2-body interaction, a 1-body potential U is considered, which is acting on the A-th nucleon and is generated by the $(A-1)$ other nucleons. The resulting Hamiltonian is given by:

$$H = \sum_{i=1}^{A} \left[\frac{\vec{p}_i^{\,2}}{2m_i} + U_i(\vec{r}) \right] + \sum_{i>k=1}^{A} V_{ik}(\vec{r}_i - \vec{r}_k) - \sum_{i=1}^{A} U_i(\vec{r}) = H_o + H_{residual}. \quad (3.2)$$

If U, which is experienced by all nucleons, approximates the 2-body interaction V the last term $H_{residual}$ becomes negligible. Because of the short range character of the nucleon-nucleon interaction the potential U is typically approximated by the nuclear density $\rho(r)$. A simple approximation is the harmonic oscillator

$$U(\vec{r}) = \frac{1}{2} m \omega^2 \vec{r}. \quad (3.3)$$

The goal of the theoretical description is to reproduce experimental findings. In particular the magic numbers: 2, 8, 20, 28, 50, 82, and 128. Figure 3.1 shows the energy level of the harmonic oscillator potential. Two things become evident. The first three magic numbers are reproduced, but the energy levels form degenerated multiplets, which contain generally more than one value of the principle quantum number n and the orbital angular momentum l. It has been substantial when Goeppert-Mayer [19] and independently Haxel, Jensen and Suess [20] introduced a spin-orbit term

$$H = \sum_{i=1}^{A} \left[\frac{\vec{p}_i^{\,2}}{2m_i} + U_i(\vec{r}) \right] + V_{ls}(r) \vec{l} \bullet \vec{s}. \quad (3.4)$$

The energy levels calculated with the spin-orbit term and a more realistic potential U, namely a Woods-Saxon potential, are presented in figure 3.1. The levels are labeled with nl_j, where n is the radial quantum number and $j = l \pm 1/2$ is the total angular momentum. Since, V_{ls} is defined to be negative the levels with $j_> = l + 1/2$ are lowered in energy, while the levels with $j_< = l - 1/2$ are raised in energy. According to the Pauli principle each level can be populated by $2j+1$ nucleons. The presented energy levels show significant gaps, yielding the magic numbers known from nuclei at stability. Apparently, the presented model is only a rough estimate. The individual consideration of protons and neutron, as well as the region of the nuclear chart require adjustments of the presented model.

The model described so far is referred to as the independent-particle model. Due to the Pauli principle the completely filled orbits nl_j couple to $J = 0$, therefore the spin and parity of a state is given by the last unpaired particle. This model predicts the ground state properties of spherical nuclei. However, if excited states

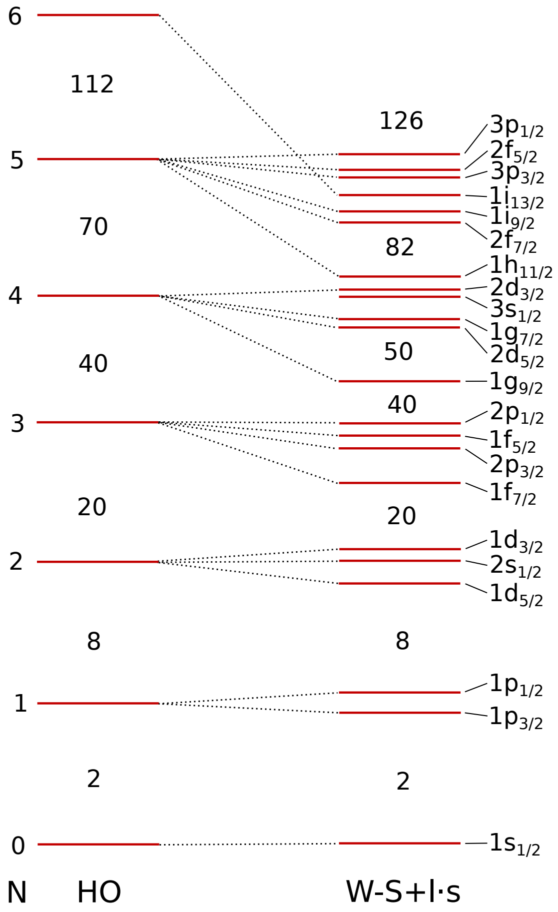

Figure 3.1.: Resulting orbits from shell model calculations, using a harmonic oscillator (HO) only (left) and using a Woods-Saxon potential together with a spin-orbit (l·s) term (right). N labels the oscillator shell: $N = 2(n-1)+l$.

are considered, combinations of multi-particle configurations have to be treated. The nuclear structure is determined by the partially filled orbits and $H_{residual}$ among them. These particles are called valence nucleons and they can couple to different total angular momentum J. A demonstrative example of such a potential is the δ interaction

$$V_{12}(\delta) = V_0\delta(\vec{r}_1 - \vec{r}_2). \tag{3.5}$$

The δ interaction has a short-range character like the nuclear force. Obviously, it can only be large when there is large spatial overlap between the orbits of the particles. The δ interaction favors low seniorities v, which is defined by the number of nucleons not paired to $J = 0$. As a consequence of this 0^+ states are lowered in energy the most, while states with increasing $J = 2, 4, \ldots$ are less affected. This prediction, especially the ground state of 0^+ in even-even nuclei, agrees very well with experimental observations.

The shell model is particularly suitable for light nuclei or nuclei close to shell closures. These nuclei are characterized by small valence spaces. Prediction for heavier mid-shell nuclei are limited by computational power, since the valence space increases rapidly.

3.2 Collective models

The shell model discussed in the previous section is reliable for the description of nuclei around closed shells. But significant deviations occur the further one goes from closed shells. In these mid-shell regions collective models allow a better description of the observed phenomena. Two examples of such collective models are given in this section. The best-known collective model is the liquid drop model by Bohr and Mottelson [14] described in section 3.2.1. The characteristics of rigid, axially asymmetric nuclei are described afterwards within the model of Davydov and co-authors (section 3.2.2).

3.2.1 Model by Bohr and Mottelson

In the model of Bohr and Mottelson the nucleus is treated as a drop of a liquid comprised of nucleons. The simplest nuclear excitation modes, within this model are nuclear vibrations and rotations. The basic principles of both excitation modes are discussed in the following.

The content of this section can be found in many text books, though the description and formulas are taken from [14, 52, 53, 55, 56].

Nuclear Vibrations

Near closed shells nuclei are spherical in their ground state. Excitations of such nuclei are commonly expressed by oscillations in their shape. These oscillations can be pictured as surface vibrations, where the nuclei are oscillating through a series of shapes with multipole order l. The radii of such nuclei are described by

$$R = R_0 \left(1 + \sum_{l,m} \alpha_{lm} Y_{lm}(\vartheta, \phi) \right), \tag{3.6}$$

where $R_0 = 1.2A^{1/3}$ is the radius of a spherical nucleus, Y_{lm} are spherical harmonics and α_{lm} denotes the amplitude of the vibration. Vibrational modes can be interpreted by phonon excitations. This notation explains the expected level schemes of vibrational nuclei in a simple way. A vibrational mode corresponding to $l = 2$ is interpreted as a quadrupole phonon, while a vibrational mode of $l = 3$ is described by an octupole phonon. Thus, an excitation of a quadrupole phonon forms a 2^+ state and 3^- states are expressed by an octupole phonon excitation.

Beside one-phonon excitations, multi-phonon excitations are possible. The excitation of two quadrupole phonons can generate a triplet of 0^+, 2^+, and 4^+ states and three-quadrupole excitations yield a quintuplet of 0^+, 2^+, 3^+, 4^+, and 6^+ states. From this description is becomes evident that the energy of an excited state goes linear with the number of quadrupole phonons contributing to the excitation. Therefore, this model predicts an $R_{4/2} = 2$ while experimental results are $R_{4/2} = 2.2$ [55]. This shows that the described model is an idealization, but reflects the underlying mechanism.

Nuclear Rotations

Rotational motion can only be observed if the nuclear shape has a substantial deformation. A common description of a quadrupole-deformed nuclear shape is given by

$$R(\vartheta, \phi) = R_0 \left(1 + \sum_{m=-2}^{2} \alpha_m Y_{2m}(\vartheta, \phi) \right), \tag{3.7}$$

where R_0 is the radius of a spherical nucleus, Y_{lm} are spherical harmonics and α_m are expansion coefficients. Conventionally, the five α_m are defined by

$$\alpha_0 = \beta \cos\gamma, \quad \alpha_{\pm 2} = \frac{1}{\sqrt{2}} \beta \sin\gamma, \quad \alpha_{\pm 1} = 0, \quad \text{with } \beta \geq 0. \tag{3.8}$$

Here, β denotes the strength of the deformation, whereby $\beta = 0$ corresponds to a spherical nucleus. If $\beta > 0$, the nucleus is deformed, while the nuclear shape

is defined by γ. For $\gamma = 0°$ the shape is prolate like an American football. $\gamma = 60°$ corresponds to an oblate nucleus formed like a discus. A γ value in between describes a triaxial nucleus, with a maximum of triaxiality at 30°. Another common notation of the quadrupole deformation is δ, which is related to β by $\delta = \beta R$.
If a nucleus is deformed, its charge distribution is distinct from that of a sphere. This causes an arising quadrupole moment with increasing deformation, which is connected to β by

$$Q_0 = \frac{3}{\sqrt{5\pi}} R_0^2 Z\beta(1 + 0.16\beta \cdots), \tag{3.9}$$

with the intrinsic quadrupole moment Q_0. It is important to note the difference between the intrinsic quadrupole moment Q_0 and the experimentally observed spectroscopic quadrupole moment Q, which is given by

$$Q = \frac{3K^2 - J(J+1)}{(J+1)(2J+3)} Q_0, \tag{3.10}$$

with K, the projection of the total angular moment J on the symmetry axis of the nucleus. It becomes evident that the spectroscopic quadrupole moment vanishes for $K = J = 0$. Furthermore, the intrinsic quadrupole moment is related to the transitions strength $B(E2)$. In case of a 2^+ state of the ground state band with $K = 0$ the relation is given by

$$B(E2; 0_1^+ \rightarrow 2_1^+) = \frac{5}{16\pi} e^2 Q_0^2. \tag{3.11}$$

For a rigid deformed nucleus, equation 3.11 and equation 3.9 in first order of β can be combined to relate the deformation parameter β to the transition strength $B(E2)$

$$\sqrt{B(E2, 0_1^+ \rightarrow 2_1^+)} = \frac{3}{4\pi} ZeR_0^2\beta. \tag{3.12}$$

Assuming that the nucleus is a rigidly rotating object with a moment of inertia I, the Hamiltonian can be written by

$$H_{rot} = \frac{\hbar^2}{2I}\vec{R}^2, \tag{3.13}$$

with the rotational angular momentum vector $\vec{R}^2$. Assuming that the ground state is $J^\pi = 0^+$, $K = 0$ and that all angular momentum is attributed to rotation, then

$\vec{J} = \vec{R}$. This leads to the expression of the rotational energies dependent on the total angular momentum

$$E_{rot}(J) = \frac{\hbar}{2I} J(J+1). \tag{3.14}$$

Note, only even J are allowed. Equation 3.14 results in an energy ratio $E_{4_1^+}/E_{2_1^+} = 3.33$. This ratio is one of the best signatures for rigid axially symmetric deformation and rotational motion.

3.2.2 Davydov model

In the 1950s Davydov and co-workers derived a model approximating the equilibrium shape of a nucleus by a rigid, stable, triaxial ellipsoid [15, 40, 71, 72, 73, 74, 75]. The nuclear radius within this model is equal to the description of the radius by Bohr and Mottelson (see equation 3.7). An example for a triaxial nucleus for $\gamma = 30°$, $\beta = 0.4$ and $R_0 = 6$ fm is given in figure 3.2. The energies of the excited states of the rigid triaxial ellipsoid are obtained by solving the Schrödinger equation

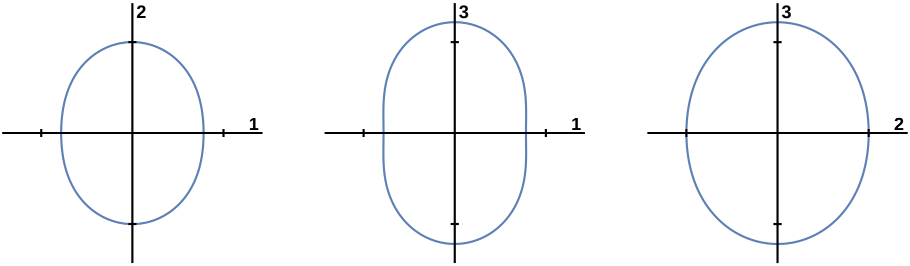

Figure 3.2.: Shape of a triaxial nucleus calculated with equation 3.7 for $\beta = 0.4$, $\gamma = 30°$ and $R_0 = 6$ fm. 1, 2, and 3 denote the symmetry axis.

$$H\Psi = E\Psi, \tag{3.15}$$

where E is measured in $\hbar/4B\beta^2$ and the Hamiltonian is given by

$$H = \frac{1}{2}\sum_{i=1}^{3} \frac{I_i^2}{\sin^2(\gamma - \frac{2}{3}\pi i)}, \tag{3.16}$$

with the projection of the total angular momentum I_i on the internal axes of the ellipsoid. The wave function corresponding to a state with total angular momentum J is defined by

$$\Psi_{JM} = \sum_K |JK\rangle A_K, \tag{3.17}$$

where

$$|JK\rangle = \sqrt{\frac{2J+1}{16\pi^2(1+\delta_{K0})}} \left(D^J_{MK} + (-1)^J D^J_{M-K} \right). \tag{3.18}$$

D^J_{MK} are functions of the Euler angles determining the orientation of the ellipsoidal axes in space and δ denotes a Kronecker delta. The derived Hamiltonian (equation 3.16) and the wave function (equation 3.17) are used to solve the Schrödinger equation (equation 3.15). This results in a set of algebraic equations for each value of J. The solution of this equations yields the energies of the states dependent on γ. Thus, two levels result for $J = 2$, defined by the expression

$$E_{J=2}(\gamma) = \frac{9(1 \pm \sqrt{1 - \frac{8}{9}\sin^2(3\gamma)})}{\sin^2(3\gamma)}. \tag{3.19}$$

Only one energy level with $J = 3$ is found:

$$E_{J=3}(\gamma) = \frac{18}{\sin^2(3\gamma)}. \tag{3.20}$$

Three $J = 4$ energy levels are obtained by the solutions of

$$E^3 - \frac{90}{\sin^2(3\gamma)}E^2 + \frac{48}{\sin^4(3\gamma)}\left(27 + 26\sin^2(3\gamma)\right)E - \frac{640}{\sin^4(3\gamma)}\left(27 + 7\sin^2(3\gamma)\right) = 0, \tag{3.21}$$

and two energy level for $J = 5$ are defined by

$$E_{J=5}(\gamma) = \frac{45 \pm 9\sqrt{9 - 8\sin^2(3\gamma)}}{\sin^2(3\gamma)}. \tag{3.22}$$

The solutions for higher J become more complex, hence the author refers to [75]. The behavior of the low-spin level for increasing γ within this model are depicted in figure 3.3. Clearly, two species of levels can be identified. The red levels are barely effected by a change of γ and correspond to the ground-state band. Whereas, the

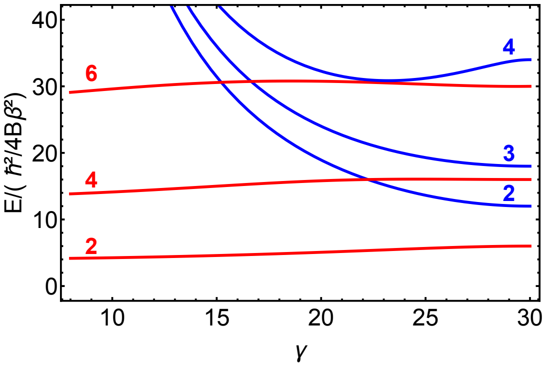

Figure 3.3.: Low-spin levels for increasing γ obtained within the model by Davydov and co-workers. The red lines show the trend for levels of the ground state band, while blue lines denote levels of the γ band.

blue levels decrease dramatically with increasing γ. They are typically referred to as γ-band members. The strong γ-dependence of the γ-band members can be used to calculate the deformation γ out of experimental results. Thus, the ratio of the 2_1^+ and 2_2^+ levels energies is described by

$$\frac{E_{2_2^+}}{E_{2_1^+}} = \frac{1+\sqrt{1+\frac{8}{9}\sin^2(3\gamma)}}{1-\sqrt{1-\frac{8}{9}\sin^2(3\gamma)}}. \tag{3.23}$$

By substituting $E_{2_2^+}/E_{2_1^+}$ with the experimental value and solving the equation one obtains the experimental γ. This can be used to make predictions within the model as e.g. ratios of $B(E2)$'s.
Additional information on this topic can be found in [55, 76].

3.3 Symmetry conserving configuration mixing-Gogny calculation

The beyond mean-field method described in this section is based on [77, 78, 79].
The symmetry conserving configuration mixing-Gogny (SCCM) calculation can be divided into three steps, which will be discussed in the following. However, before it is important to mention briefly the Hartree-Fock-Bogoliubov (HFB) theory, combining the achievements of the Bardeen-Cooper-Schrieffer (BCS) model and the Hartree-Fock (HF) method. The HF method extracts a single-particle potential

out of the sum of a two-body interactions by variational principle using Slater-determinants as trivial wave functions. Therefore, the HF method describes the long-range part of the force only. The special feature of the BCS model is to treat the correlations of independent particles in an average potential by quasi particles and the pairing field, which describes the short-range part of the force. The HFB theory finds the most general product wave function consisting of independently moving quasi particles. While staying within the static single particle picture the wave functions are obtained by a variational principle and take into account as many correlations as possible.

In a first step of the SCCM calculation, the HFB wave functions $|\Phi(\beta,\gamma)\rangle$ are determined by minimizing the particle number projected HFB energy. This is done by the particle number projection before the variation (PN-VAP) method [80]. If $|\Psi\rangle$ is a product wave function of the HFB type, an eigenstate $|\Phi(\beta,\gamma)\rangle$ can be obtained by the particle number projection technique

$$|\Phi(\beta,\gamma)\rangle = \hat{P}^N \hat{P}^Z |\Psi\rangle, \tag{3.24}$$

where P^N and P^Z are operators projecting on the particle number. The wave functions use the quadrupole degree of freedom and depend on the deformation parameters β and γ. Afterwards the wave function $|\Phi(\beta,\gamma)\rangle$ is determined by minimizing the projected energy

$$\begin{aligned} E_{proj} = & \frac{\langle\Phi(\beta,\gamma)|\hat{H}\hat{P}^N\hat{P}^Z|\Phi(\beta,\gamma)\rangle}{\langle\Phi(\beta,\gamma)|\hat{H}|\Phi(\beta,\gamma)\rangle} \\ & - \lambda_{q20}\langle\Phi(\beta,\gamma)|\hat{Q}_{20}|\Phi(\beta,\gamma)\rangle - \lambda_{q22}\langle\Phi(\beta,\gamma)|\hat{Q}_{22}|\Phi(\beta,\gamma)\rangle \end{aligned} \tag{3.25}$$

It can be seen that the minimization is performed under constrains on the quardupole deformation operators $\hat{Q}_{2\mu}$. Lagrange multipliers $\lambda_{q2\mu}$ ensure that the following conditions are fulfilled:

$$q_{20} = \frac{\beta\cos\gamma}{C}, \qquad q_{22} = \frac{\beta\sin\gamma}{\sqrt{2}C}, \qquad C = \sqrt{\frac{5}{4\pi}\frac{4\pi}{3r_0^2A^{5/3}}}, \tag{3.26}$$

with $r_0 = 1.2$ fm and the mass number A. These constrains allow to explore the (β,γ) plane to generate the wave functions, which are used in the configuration mixing calculation.

In a second step, a simultaneous particle number and momentum projection (after the variation) is performed. This process is described by

$$|JMK;NZ;\beta\gamma\rangle = P^J_{MK} P^N P^Z |\Phi(\beta,\gamma)\rangle, \tag{3.27}$$

with the operators P^J_{MK}, P^N, and P^Z that project onto good angular momentum and numbers of particles. N, Z, J, M, K denote the number of neutrons and protons, the total angular momentum and the angular momentum component on the z axes of the laboratory and intrinsic frames, respectively.

In the last step, the configuration mixing within the framework of the generator coordinate method (GCM) is performed. The final many-body wave function is defined by

$$|JM;NZ;\sigma\rangle = \sum_{\beta,\gamma,K} f^{J;NZ;\sigma}_{\beta,\gamma,K} |JMK;NZ;\beta\gamma\rangle, \tag{3.28}$$

where the coefficients $f^{J;NZ;\sigma}_{\beta,\gamma,K}$ of the linear combination are found by minimizing the energy within the nonorthogonal set of wave functions $\{|JMK;NZ;\beta\gamma\rangle\}$. This minimization is equivalent to solving the Hill-Wheeler-Griffin equation

$$\sum_{\beta',\gamma',K'} \left(\mathscr{H}^{J;NZ}_{\beta,\gamma,K;\beta'\gamma',K'} - E^{J;NZ;\sigma} \mathscr{N}^{J;NZ}_{\beta,\gamma,K;\beta'\gamma',K'} \right) f^{J;NZ:\sigma}_{\beta'\gamma',K'} = 0. \tag{3.29}$$

The solution of this equation gives directly the energy spectrum.

3.4 Interacting Boson Model 2

In order to understand the concept of the Interacting Boson Model (IBM)-2 it is beneficial to describe the basic ideas of the predecessor IBM-1 first and extend it to the IBM-2 afterwards. This section is close to the description in [16, 53, 55].

IBM-1

The IBM-1 considers valence nucleons outside of a doubly-magic core. These nucleons are coupled pairwise to $N = (N_\pi + N_\nu)/2$ bosons, where N_π and N_ν denote the number of protons and neutrons. Thereby, the model does not distinguish between particles and holes, in order to obtain the closest distance to a doubly-magic nucleus. In the simplest version of the IBM, s $(J = 0)$ and d $(J = 2)$ bosons are used. These bosons have creation and destruction operators

$$s^\dagger, s, \quad \text{and} \quad d^\dagger_\mu, \tilde{d}_\mu, \quad \text{with} \quad -2 \leq \mu \leq 2. \tag{3.30}$$

With these operators the Hamiltonian is given by

$$H = \epsilon'' n_d + a_0 P^\dagger P + a_1 J^2 + a_2 Q^2 + a_3 T_3^2 + a_4 T_4^2 \tag{3.31}$$

where

$$\begin{aligned} P &= \frac{1}{2}\left(\tilde{d}^2 - s^2\right) \\ T_{(J)} &= (d^\dagger \tilde{d})^{(J)}, \quad J = 0,1,2,3,4 \\ Q &= (d^\dagger s + s^\dagger \tilde{d}) - \frac{\sqrt{7}}{2} T_2 \\ n_d &= \sqrt{5} T_0 \\ J &= \sqrt{10} T_1 \end{aligned} \tag{3.32}$$

The six s and d boson operators from a six-dimensional Hilbert space. For the restriction that the total number of bosons is preserved 36 combinations of the operators exist, given by

$$s^\dagger s, \quad d_\mu^\dagger s, \quad s^\dagger \tilde{d}_\mu, \quad (d_\mu^\dagger \tilde{d}_\mu)^J, \tag{3.33}$$

where $J = 0,1,2,3,4$ and $|\mu| \leq J$. It can be shown that this operators are generators of the $U(6)$ Lie algebra, since they close under commutation. Further subgroups can be found, which them self close under commutation, and therefore, form a subgroup of $U(6)$. Three of this subgroups have a common reduction end in $O(3)$, which is the rotational group. These subgroups $U(5)$, $SU(3)$, and $O(6)$ represent important nuclear symmetries and can be written with their relevant quantum number by

$$\begin{array}{llllll} 1. & U(6) \supset & U(5) \supset & O(5) \supset & O(3) & U(5) \\ & N & n_d & \nu & n_\Delta J & \end{array} \tag{3.34}$$

$$\begin{array}{llllll} 2. & U(6) \supset & SU(3) \supset & O(3) & & SU(3) \\ & N & \lambda, \mu & KJ & & \end{array} \tag{3.35}$$

$$\begin{array}{llllll} 3. & U(6) \supset & O(6) \supset & O(5) & O(3) & O(6) \\ & N & \sigma & \tau & \nu_\Delta J & \end{array} \tag{3.36}$$

Regarding the group decompositions 1. to 3. Casimir operators can be found, which commute with all generators of the particular group. This Casimir operators have eigenvalues defined by a function of the conserved quantum number of the dedicated subgroup. The eigenvalues of the Hamiltonian are obtained by linear combinations of the component Casimir operator eigenvalues. Thus, the eigenvalues are functions of the quantum number characterizing each group and subgroup. The representation of the Hamiltonian by Casimir operators of the group chain is referred to as dynamical symmetry. The three dynamical symmetries of the IBM form the corners in the phase diagram shown in figure 3.4. The $U(5)$ symmetry corresponds to a vibrational nucleus with a ratio of the 4_1^+ to 2_1^+ level energy $R_{4/2} = 2$. A prolate rotor with an $R_{4/2} = 3.33$ is described by the dynamical symmetry $SU(3)$ and $O(6)$ corresponds to a γ-soft nucleus with an $R_{4/2} \simeq 2.5$. For more details on the dynamical symmetries the author refers to [16, 53, 55].

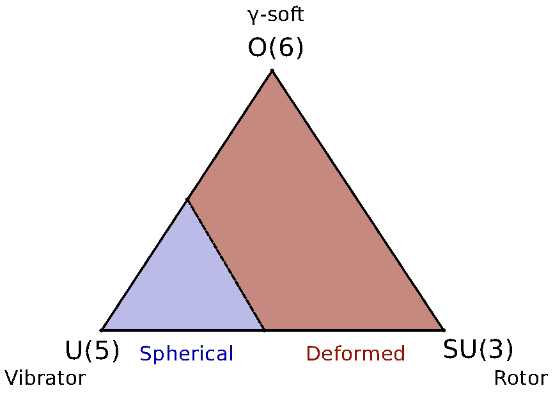

Figure 3.4.: Triangle showing the symmetries of the IBM. The dynamical symmetries $U(5)$, $SU(3)$, and $O(6)$ define the corners of the triangle.

IBM-2

The IBM-1 described before is further developed by considering the proton-neutron degree of freedom. This version of the IBM is called IBM-2, and its major success is the description of mixed-symmetric states.

The IBM2 distinguishes between neutron and proton bosons and their creation and destruction operators are given by

$$s_\rho^\dagger, s_\rho, \quad \text{and} \quad d_{\mu\rho}^\dagger, \tilde{d}_{\mu\rho}, \quad \text{with} \quad -2 \leq \mu \leq 2 \quad \text{and} \quad \rho = \pi, \nu. \tag{3.37}$$

Therefore, the basis of the IBM-2 is now spanned by a $U(6)\otimes U(6)$ Lie algebra. The Hamiltonian can be formulated by [81]

$$H = H_\pi + H_\nu + V_{\pi\nu}, \tag{3.38}$$

where H_π and H_ν are identical to the Hamiltonian of the IBM-1. The proton-neutron interaction $V_{\pi\nu}$ is a linear combination of scalar products of the creation and destruction operators for neutrons and protons given by equation 3.37. A frequently used form of the IBM-2 Hamiltonian is given by [17]

$$\begin{aligned} H = E_0 &+ \epsilon_\pi n_{d_\pi} + \epsilon_\nu n_{d_\nu} + \kappa_{\pi\pi} Q_\pi^{\chi_\pi} Q_\pi^{\chi_\pi} + 2\kappa_{\pi\nu} Q_\pi^{\chi_\pi} Q_\nu^{\chi_\nu} \\ &+ \kappa_{\nu\nu} Q_\nu^{\chi_\nu} Q_\nu^{\chi_\nu} + M(\xi_1, \xi_2, \xi_3), \end{aligned} \tag{3.39}$$

where n_{d_ρ} are d-boson number operators for protons and neutrons with the respective d-boson energy, $Q_\rho^{\chi_\rho}$ denotes the quadrupole operator for proton and neutron bosons and $M(\xi_1, \xi_2, \xi_3)$ is the Majorana interaction, which can be defined by [17]

$$\begin{aligned} M(\xi_1, \xi_2, \xi_3) = &\frac{1}{2}\xi_2 (s_\pi^\dagger d_\nu^\dagger - d_\pi^\dagger s_\nu^\dagger) \cdot (s_\pi \tilde{d}_\nu - \tilde{d}_\pi s_\nu) \\ &- \sum_{K=1,3} \left([d_\pi^\dagger d_\nu^\dagger]^{(K)} \cdot [\tilde{d}_\pi \tilde{d}_\nu]^{(K)} \right). \end{aligned} \tag{3.40}$$

The shown Hamiltonian reflects the nucleonic pairing-plus-quadrupole Hamiltonian and contains the proton-neutron quadrupole-quadrupole interactions and a symmetry energy term.

4 SEASTAR setup

The SEASTAR campaign aims to make the first spectroscopic measurement of exotic nuclei, which are near the limits of current accelerator capabilities. To access these rare isotopes the SEASTAR campaign was conducted at the Radioactive Beam Factory (RIBF) [21] in Tokyo. The RIBF is one of the unique accelerators, which allows to reach such exotic regions with high intensities. It uses the method of in-flight fission of a ^{238}U beam accelerated to an energy of 345 MeV/u by a sequence of different cyclotrons to produce an extremely neutron-rich medium mass secondary beam with an energy of $\sim$ 250 MeV/u. In order to increase the N/Z ratio $(p, 2p)$ reactions at a reaction target are used. Knocking out a proton from a neutron-rich nucleus leads to one with an even higher N/Z ratio than of the incident nucleus. These proton knock-out reactions arise from interactions with a 100 mm long LH_2 reaction target. The length of the target was chosen such that the luminosity becomes high. However, the secondary beam energies are considerably high, causing Doppler-shift of γ radiation emitted in flight. For a proper Doppler-correction the point of the γ-ray emission is needed. The LH_2 target is surrounded by a time projection chamber (TPC) to reconstruct the reaction vertex of the impinging nuclei and improve the Doppler-correction. This combination of a LH_2 target with a TPC is called MINOS (Magic Numbers Off Stability) [82]. An important advantage of MINOS is that it will cause less background from target reactions and atomic background compared to a target of higher mass. Furthermore, it can distinguish between reactions occurring in the target and background generated by reactions originating from upstream. The emitted γ radiation was detected by the NaI(Tl) scintillator array DALI2 (Detector Array for Low Intensity radiation 2) [83]. One of its special characteristics is the high efficiency, which is important for the spectroscopy of very neutron-rich nuclei produced with small statistics. The incoming and outgoing channels are selected by the excellent particle identification of the BigRIPS (Big RIKEN Projectile-fragment Separator) fragment separator and the ZeroDegree spectrometer [84].

In the following, the setup of the SEASTAR campaign 2015 is described. A detailed description of the ion production and acceleration is given in section 4.1 which is based on information taken from [85, 86]. Section 4.2 gives an overview of the BigRIPS fragment separator and the ZeroDegree spectrometer as well as their detector systems resting upon [84, 87, 88, 89, 90]. More precise information about the performance and structure of MINOS is given in section 4.3 which follows [82,

91, 92]. Section 4.4 that is based on information from [93] gives an overview on the DALI2 detector array. A description of the data acquisition and the trigger system used during the SEASTAR campaign 2015 is given in section 4.5.
Additional descriptions of the experimental setup can be found in [92, 94, 95].

4.1 Ion production and acceleration

The RIBF at Tokyo has three different acceleration modes [85], as shown in figure 4.1. Light ions such as the deuteron, nitrogen, oxygen etc. are accelerated in the azimuthally varying field (AVF) mode. In this mode, the beam is boosted by the RRC (RIKEN Ring Cyclotron) and the SRC (Superconducting Ring Cyclotron), as illustrated by the blue line. Indicated by the yellow line, the second mode is depicted which is applied to accelerate medium-mass ions like calcium, krypton, zinc, etc. The RILAC (RIKEN Heavy-ion Linac) pre-accelerates the ions and the three cyclotrons: RRC, IRC (Intermediate-stage Ring Cyclotron) and SRC accelerate them further. For heavy ions, such as uranium and xenon, the fixed-energy mode is used which is shown by the red line. This mode was exerted for the SEASTAR campaign 2015. ^{238}U is produced by the SC-ECR (superconducting electron cyclotron resonance) ion source. Afterwards, the ions are injected in the RILAC2 and are accelerated to 0.67 MeV/u. Passing the RRC, the ions reach an energy of $\sim$ 11 MeV/u. Cycling through the fRC (fixed-frequency Ring Cyclotron), IRC, and SRC, the ions' energy is further increased to $\sim$ 51 MeV/u, $\sim$ 114 MeV/u and $\sim$ 345 MeV/u, respectively [86]. Two charge strippers are installed in this mode. The first is located after RRC (ST3) while the second is placed behind the fRC (ST4). Having left the SRC, the ions impinge onto a 3 mm thick ^{9}Be target at the entrance of the BigRIPS separator whereby different fission fragments are formed.

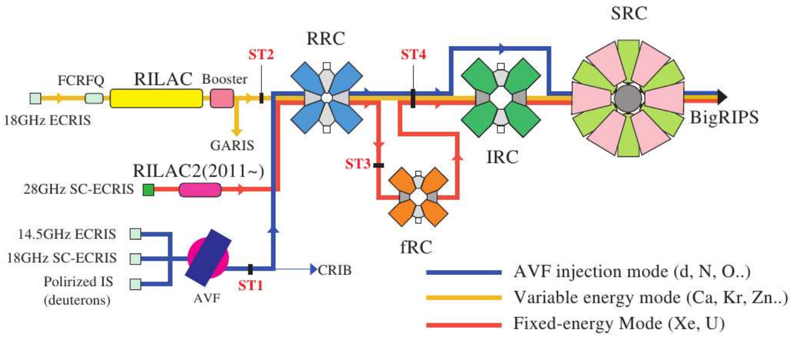

Figure 4.1.: Sketch of the ion production and the different acceleration modes at the RIBF. The acceleration mode used for the SEASTAR campaign 2015 is depicted in red. The figure is taken from [85].

4.2 BigRIPS fragment separator and ZeroDegree spectrometer

A schematic picture of the superconducting in-flight separator BigRIPS, followed by the forward spectrometer ZeroDegree, is shown in figure 4.2. The BigRIPS fragment separator has seven foci (F1-F7) along the beam line and a total length of 78.2 m. It is composed of fourteen superconducting triplet quadrupole magnets (blue) and six room-temperature dipole magnets (green) with a bending angle of 30°. Each superconducting triplet quadrupole magnet consists of three quadrupole magnets, beside the two superconducting triplet quadrupole magnets between the foci F2 and F3 where one of the three quadrupole magnets is equipped with a sextupole fraction. Furthermore, the large ion-optical acceptance and its two stage structure characterize the BigRIPS fragment separator. Allowing to have an efficient production of rare-isotopes by in-flight fission of a ^{238}U beam, the BigRIPS separator has an angular acceptance of ±40 mr horizontally and ±50 mr vertically and a momentum acceptance of ±3%. These acceptances ensure the collection of fission fragments with an efficiency of $\sim 50\%$. In order to allow the production of high purity rare-isotope beams, the BigRIPS fragment separator is structured in two stages. The first stage ranges from the production target to the achromatic focus F2 and forms a two-bend achromatic system with a momentum-dispersive focus at F1. In this stage the BigRIPS separator has a maximum magnetic rigidity ($B\rho$) of 9.5 Tm. In order to provide isotopic separation, a wedge-shaped degrader (orange) can be placed at F1. The second stage, which is located between the achromatic foci F3 and F7, forms a four-bend achromatic system with dispersive foci F4, F5 and F6. The maximum magnetic rigidity achieved in this stage is 8.8 Tm. During the

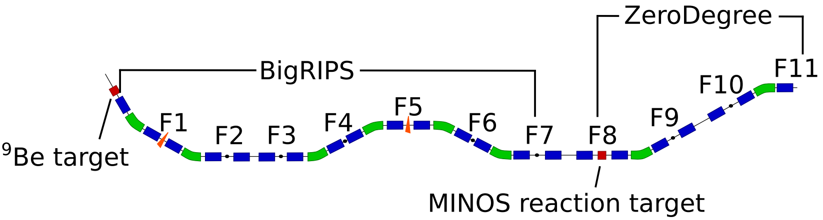

Figure 4.2.: Sketch of the BigRIPS fragment separator and the ZeroDegree spectrometer. Dipole magnets are depicted in green whereas quadrupole magnets are shown in blue. The two targets are indicated by the red squares. The ^{9}Be production target is shown at the entrance of the BigRIPS fragment separator. The liquid hydrogen reaction target MINOS is located at the focal point F8.

SEASTAR campaign 2015, a second degrader was placed at F5 to apply a two-stage isotopic separation. This operation of the BigRIPS fragment separator is referred to as the separator-separator mode. The two triplet quadrupoles after F7 are used to match the section between BigRIPS and the first focal point F8 of ZeroDegree where the liquid hydrogen reaction target MINOS was placed. The ZeroDegree spectrometer is a two-bend achromatic system composed of four foci F8, F9, F10 and F11 and a total length of 36.5 m. F9 and F10 are momentum dispersive while the final focus F11 is fully achromatic. The spectrometer uses two dipole magnets and six superconducting triplet quadrupole magnets with one sextupole fraction in each triplet magnet. Determined by the experimental needs, the ZeroDegree spectrometer can be operated in different ion-optic modes. The SEASTAR campaign 2015 made use of the large acceptance achromatic mode. In this mode, the ZeroDegree spectrometer has an angular acceptance of ±45 mr horizontally, ±30 mr vertically and a momentum acceptance of ±3%. The maximum magnetic rigidity in this mode is 8.1 Tm. During the SEASTAR campaign, isomer spectroscopy was performed at the final focus point of ZeroDegree. Therefore, the ions were stopped and delayed γ-ray emission was detected with EURICA [96]. Since this experiment is not part of this work, it will not be further discussed.

4.2.1 Particle identification

The particle identification in the BigRIPS fragment separator and the ZeroDegree spectrometer is performed by the TOF-$B\rho$-ΔE method. Using this method, the mass-to-charge ratio (A/Q) and the proton number Z are obtained by a measurement of the time of flight (TOF), the magnetic rigidity ($B\rho$) and the energy loss (dE/dx) of the ions. Considering an ion on a trajectory through a dipole magnet, the Lorentz force ($Q\vec{v} \times \vec{B}$) is acting as centripetal force (mv^2/ρ), which is leading to the mass-to-charge ratio [87]

$$\frac{A}{Q} = \frac{B\rho}{\beta\gamma}\frac{c}{m_u}. \tag{4.1}$$

The ratio of the velocity of the ion v to the speed of light c is given by $\beta = v/c$, $\gamma = 1/\sqrt{1-\beta^2}$ is the Lorentz factor and $m_u = 931.5$ MeV/c^2 is the atomic mass unit.

In order to obtain the ion's velocity, the flight time is measured using thin plastic scintillation counters placed at the achromatic foci F3 and F7 in BigRIPS, and F8 and F11 in ZeroDegree. The time of flight (TOF) is given by [87]:

$$TOF = \frac{L}{\beta c}, \tag{4.2}$$

where, L denotes the length of the flight path between F3 and F7 in BigRIPS or between F8 and F11 in ZeroDegree.
The value $B\rho$ is obtained by the reconstruction of the ions' trajectory in the sections F3-F5 and F5-F7 in BigRIPS, and F8-F9 and F9-F11 in ZeroDegree, respectively. The particle trajectories are derived with two sets of position-sensitive parallel plate avalanche counters (PPAC). The functionality of the PPACs is given in section 4.2.2. During the SEASTAR campaign 2015 a degrader is placed at F5. Using a degrader at F5, the mass-to-charge ratio A/Q in BigRIPS cannot be determined as described in equation 4.1. So it is necessary to apply a twofold $B\rho$ measurement. Therefore, equation 4.1 and 4.2 transform to [87]:

$$TOF = \frac{L_{35}}{\beta_{35} c} + \frac{L_{57}}{\beta_{57} c}, \tag{4.3}$$

$$\left(\frac{A}{Q}\right)_{35} = \frac{B\rho_{35}}{\beta_{35}\gamma_{35}} \frac{c}{m_u}, \tag{4.4}$$

$$\left(\frac{A}{Q}\right)_{57} = \frac{B\rho_{57}}{\beta_{57}\gamma_{57}} \frac{c}{m_u}. \tag{4.5}$$

The subscripts (35) and (57) indicate the different sections in BigRIPS. In order to avoid a separate measurement of β_{35} and β_{57}, it is assumed that the mass-to-charge ratio stays constant in both sections, since the ions are fully stripped. Hence, Equation 4.4 and Equation 4.5 can be combined to the following relation [87]:

$$\frac{\beta_{35}\gamma_{35}}{\beta_{57}\gamma_{57}} = \frac{B\rho_{35}}{B\rho_{57}}. \tag{4.6}$$

The obtained relation along with Equation 4.3 is used to derive both velocities β_{35} and β_{57} independently by measuring the TOF, as well as $B\rho_{35}$ and $B\rho_{57}$, which is leading to the determination of the absolute A/Q. To get a distinct identification of the nuclei of interest, the absolute proton number Z has to be obtained in addition. Two tilted electrode gas ionization chambers (TEGIC) are, for this purpose, installed at F7 and F11 to perform a measurement of the energy loss dE/dx. This component is further described in section 4.2.3. The energy loss of fast, charged particles in matter is given by the Bethe-Bloch formula [87]:

$$\frac{dE}{dx} = \frac{4\pi e^4 Z_p^2}{m_e v^2} N_t Z_t \left[\ln \frac{2m_e v^2}{I_t} - \ln(1-\beta^2) - \beta^2 \right]. \tag{4.7}$$

The electron mass and the elementary charge are represented by m_e and e. Furthermore, Z_t and N_t denote the atomic number and the density of the target. I_t is the average excitation potential of the target material. The energy loss dE/dx is proportional to the squared proton number of the projectile Z_p^2. The usage of β_{57}, derived as previously described, permits the absolute proton number Z. Finally, the ion identification can be ensured by a two-dimensional plot of the absolute proton number Z drawn against the mass-to-charge ratio A/Q. In section 5.1.4, this method is used for the particle identification.

4.2.2 Position-sensitive parallel plate avalanche counters (PPAC)

The delay line position-sensitive Parallel Plate Avalanche Counters (PPAC) serve to measure the ion trajectories through the BigRIPS fragment separator. A schematic picture of this detector system is shown in figure 4.3. The setup consists of three parallel mounted electrodes at a distance of 4.3 mm each. An anode electrode is placed between an x-axis and a y-axis cathode. The electrodes are produced by metal deposition on a thin polyester film. The films thickness is 2.5 μm for the anode and 4 μm for the cathodes. Both cover an area of 240 mm×150 mm. The anode electrode is covered with a thin film of metal on both sides. The metal is deposited in strips of 2.4 mm width with a spacing of 0.15 mm on one side of the cathode electrodes in contrast to the anode, which has no strips. The strips are attached to delay-lines. In order to get a higher detection efficiency, two sets of delay-line PPAC detectors are placed in one housing and the chamber is filled with C_3F_8 gas. This layout is referred to as double PPAC and provides a back up in case one of the PPAC detectors fails. Ions passing the double PPAC cause an ionization of the detector gas and the occurrence of an electron avalanche. The signals induced in the cathode enter the delay-line and split up in the signals X1, Y1, X2 and Y2, as shown in figure 4.3. The cathode signals serve as stop signal and are then forwarded, with the signal taken from the anode, to a TDC in order to obtain the delay times $T_{xi,yi}$. Based on the delay times the positions x, y can be determined to [88]

$$x = K_x \frac{T_{X1} - T_{X2}}{2} + X_{off}, \tag{4.8}$$

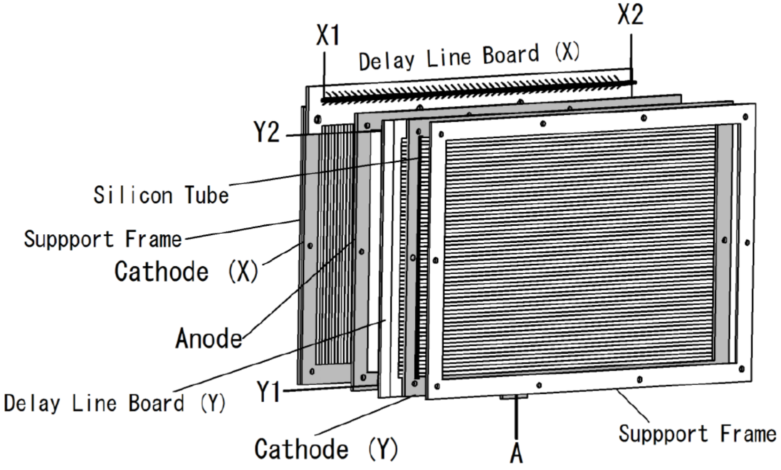

Figure 4.3.: Schematic picture of a PPAC detector. Three electrodes are shown. A cathode with Y strips in the front, whereas the components are spatially divided. The anode plane is shown in the middle and a second cathode with strips in X direction is located in the back. See text for more details. The picture is taken from [88].

$$y = K_y \frac{T_{Y1} - T_{Y2}}{2} + Y_{off}. \tag{4.9}$$

K_x and K_y denote position coefficients, while X_{off} and Y_{off} are offsets correcting for delay-line offsets or a misalignment of the detector system. To verify the consistency of the measured times, the sum of the delay times $T_{sum,X,Y}$ is used since its value is independent of the interaction position inside the PPAC [88].

$$T_{sum,X} = T_{X1} + T_{X2} \tag{4.10}$$

$$T_{sum,Y} = T_{Y1} + T_{Y2} \tag{4.11}$$

During the experiment, two double PPACs were used at the focal planes F3, F5, F7, F8, F9 and F11 in BigRIPS and ZeroDegree. At each of these focal planes, four independent measurements of the position (x, y) were performed for events with a consistent $T_{sum,X}$ and $T_{sum,Y}$. It was possible to reconstruct the focal points from this distinct ion path.

4.2.3 Tilted electrode gas ionization chamber (TEGIC)

Grid-less ionization chambers, robust enough to withstand the rapid beam bombardment, served to measure the energy loss dE/dx. A sketch of such a tilted electrode gas ionization chamber (TEGIC) is shown in figure 4.4. Twelve circular anode planes and thirteen circular cathode planes at a distance of 20 mm are placed in one chamber, resulting in a 48 cm long chamber consisting of 24 parallel plate ionization chambers one behind the other. The anode and cathode planes are conductive foils on which a 4 μm thick mylar layer is applied to each side. These foils are fixed on an aluminum ring with an inner diameter of 11.6 cm. In order to avoid recombination of occurring electrons and positive ions along the path of the impinging projectiles, the electrodes are tilted by 30°. Thus, the electrons and positive ions drift away from their place of origin in opposite directions. The whole setup is housed by an aluminum vessel with two Kapton sheets of 50 μm thickness located at the entrance and exit windows. The chamber was filled with a gas mixture of Ar$-$CH$_4$ (90%,10%) with a purity of $> 99.99\%$. As shown in figure 4.4, pairs of anodes are interconnected, forming six output channels. However, the cathodes are connected to the ground, while the anode voltage amounts to 500 V. In BigRIPS and ZeroDegree, two TEGICs were used to obtain the atomic number

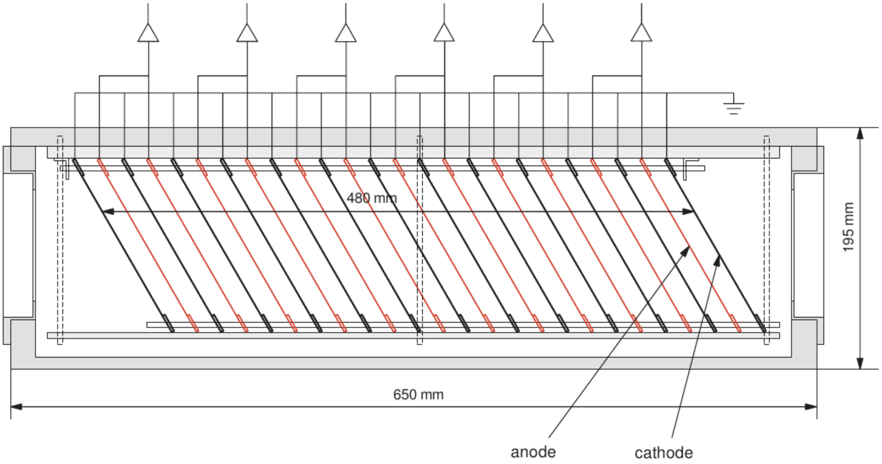

Figure 4.4.: Schematic rip cut of a TEGIC. Anode planes (red) are read out in pairs. Cathode planes (black) are connected to the ground. See text for more details. The picture is taken from [90].

of the impinging ions by a measurement of dE/dx. The first was placed at F7, the end of BigRIPS, and the second at F11, the end of ZeroDegree. The energy loss dE/dx was obtained by the geometrical average of the six output signals and then transformed to the atomic number with the Bethe-Bloch Equation 4.7.

4.3 MINOS

Experiments such as those from the SEASTAR campaign are limited by the energy and the position-resolution of the γ spectrometer and the choice of the target. Considering an ordinary target, one has to compromise between a thick target to increase luminosity and a thin target to reduce the velocity spread and therefore the quality of the Doppler correction. MINOS has been created in order to avoid this conflict. It consists of a thick liquid-hydrogen target surrounded by a proton tracker which measures the reaction-vertex position inside the target on an event-by-event basis. The precise knowledge of the reaction-vertex position allows a high-quality Doppler-correction although an extended target is used. The characteristics of the liquid-hydrogen target are described in section 4.3.1; the proton tracker is described in section 4.3.2. These sections are based on [82, 91, 92].

4.3.1 Liquid Hydrogen Target

The MINOS target cell consists of an entrance window and a cup-shaped exit window attached to a stainless steel target holder. A schematic picture of the target cell is shown in figure 4.5. The entrance and the exit window are made of polyethylene terephthalate, often known by its trade name Mylar. The entrance window has a thickness of 100 μm and an effective diameter of 38 mm. The cup-shaped exit window is 150 μm thick, it has a diameter of 52 mm and a length which can be adjusted to 150 mm or 100 mm. During the SEASTAR campaign, the length was set to 100 mm. Both windows are manufactured by mechanical stamping at 160 °C. Due to this reason, and given that the target is pressurized, both windows are slightly curved. The exit window can be assumed as rigid with a central deviation of 4 mm in comparison to a flat end cap, whereas the pressure inside the target cell dictates the bending of the entrance window. During the SEASTAR campaign, a curvature of 2.7 mm was observed [92]. Two tubes directed through the target holder permit to supply the liquid hydrogen and to lead the gas away. The hydrogen is liquefied in a cryostat equipped with a cryo-cooler placed above the target cell. By gravity, the liquefied hydrogen flows into the target cell through the pipe. Throughout the SEASTAR campaign, the target cell was placed in a beam pipe of 72 mm inner diameter and 2 mm thickness [92]. At each end of the beam

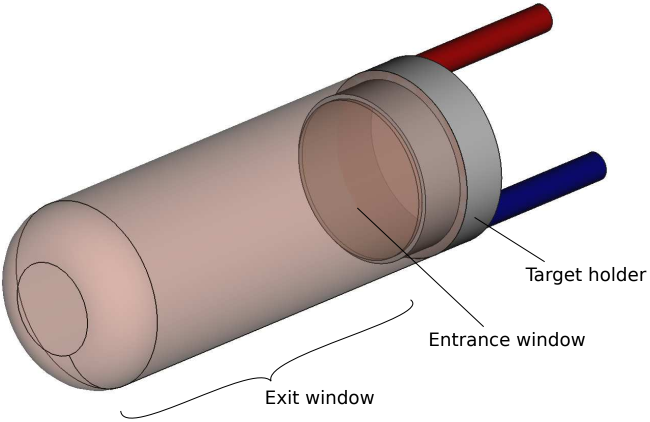

Figure 4.5.: Schematic picture of the MINOS target cell.

line, 150 μm thick Mylar windows were attached [92], by which the enclosed area could be evacuated to $\sim 10^{-6}$ mbar [92].

4.3.2 Vertex Tracker

The MINOS vertex tracker is an annular Time Projection Chamber (TPC) surrounding the liquid-hydrogen target cell. The gaseous TPC is read out on one side by a bulk-Micromegas detector which is segmented in pads. An external cylindrical bulk-Micromegas layer is surrounding the housing of the TPC [82]. A schematic picture of the vertex tracker is shown in figure 4.6.

The vertex tracker is used to reconstruct the outgoing proton tracks, occurring after e.g. a $(p, 2p)$ reaction, in three dimensions serving to localize the vertex position of the reaction inside the reaction target. The vertex tracker has a compact design limited by the space inside the DALI2 array and the size of the beam pipe. The TPC vessel is 300 mm long and has an internal diameter of 80 mm and an external diameter of 178.8 mm. The thickness of the internal and external concentric cylinders amounts to 2 mm. The TPC vessel is filled with a gas mixture of argon (82%), CF_4 (15%) and isobutane (3%). During experiments, a typical voltage of 6 kV is applied between the electrodes [92].

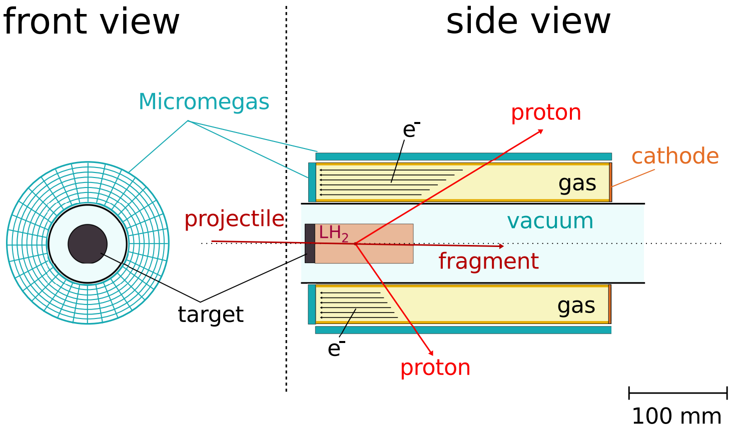

Figure 4.6.: Schematic picture of the MINOS device from front (left) and a side view (right). The picture is based on information from [82].

Micromegas detector

A simplified sketch of a Micromegas detector is shown in figure 4.7. A thin micro-mesh divides the detector in two regions [97, 98]. The first region, where the ionization of the gas and the drift of the electrons occur, is called the conversion gap. In case of the MINOS TPC, this region is defined by the TPC length of 300 mm. The simultaneous application of a negative voltage on the micro-mesh (HV2) and

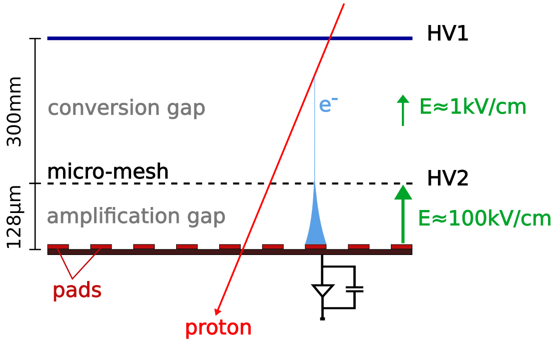

Figure 4.7.: Schematic picture of the Micromegas detector based on information of [97].

a slightly higher voltage on the second electrode (HV1) defines the electric field in the conversation gap. The second region referred to as the amplification gap has a length of 128 μm. By applying a voltage of a few hundred volts between the micro-mesh and the anode, a high field of 40 to 70 kV/cm is created in this region. The high field serves to collect the charge of the avalanche. The anode is segmented in pads of different areas, as shown on the left side in figure 4.6. The anode disc composes of 18 cylindrical rings with a thickness of 2 mm segmented in 256 sections. Therefore, the outer pads with bigger radii have a larger area than the inner pads. The MINOS Micromegas detector has 4608 channels in total.

Field cage

In order to ensure a precise vertex reconstruction, the uniformity, the stability, and the knowledge of the electric field lines inside the TPC volume has to be guaranteed. The reconstruction is achieved by TPC field cages defining the path of the electrons ionized along the proton tracks. One field cage is surrounding the inner concentric cylinder of the TPC vessel, a second is located at the inner side of the external concentric cylinder of the TPC vessel, as shown in figure 4.8b. The TPC field cages are designed with an uniform electric field ($E_z/E_x \leq 10^{-4}$) at the first pad location. The quality of the electric field is ensured by a field cage made of 1 mm thick strips with a gap of 1.5 mm on both sides of a 50 μm thick Kapton foil, as illustrated in figure 4.8a. This results in an equivalent 0.75 mm pitch between top

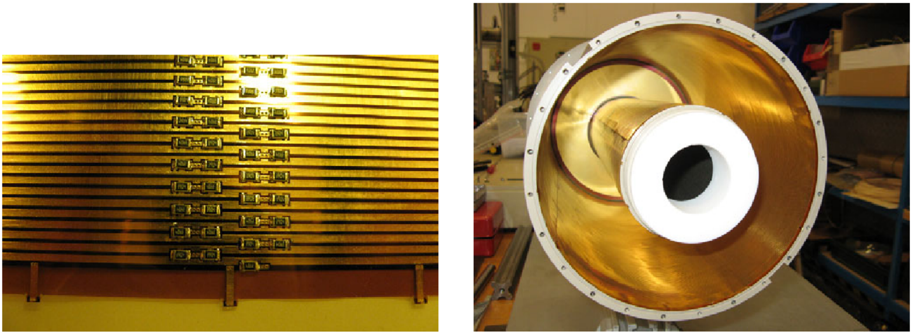

(a) The capton foil field cage of MINOS with copper strips and resistors in between.

(b) Opened MINOS TPC. Inner and outer field cages are visible.

Figure 4.8.: Pictures of the field cage of MINOS taken from [82].

and bottom strips, whereby the first strip of the field cage is located 4.5 mm below the cathode plane. The last strip has a distance of 1.5 mm to the Micromegas mesh. In total the field cage is composed of 196 (195) bottom (top) strips. As shown in figure 4.8a, two 3.9 MΩ surface mount resistors are connected in parallel between a top and its neighboring bottom strip. Both field cages are voltage supplied in parallel through the cathode high-voltage. A separate high voltage is applied on the last strip of the field cages to ensure a proper drift of the electrons in the region of the Micromegas.

Supplementary Micromegas detector

An external Micromegas detector has been designed to fit around the TPC vessel. It is composed of two half-cylinders with a radius of 92 mm [82]. The anode strips are oriented orthogonally to the length of the TPC. The principle design of the Micromegas is the same as described in section 4.3.2. It consists of an amplification gap of 128 μm and a more compact conversion gap of 3 mm. The detector is supplied with the same gas mixture as the TPC and it is connected to the same gas circuit. The detector enables to measure the z coordinate of each track independently of the TPC drift velocity. This allows to monitor the electron drift velocities during experiments and it offers the opportunity to take action in case the experimental conditions change. In addition, the external Micromegas detector can be used as an external trigger for MINOS. However, the external Micromegas detector has not been used for an experiment so far [92].

Reconstruction of the proton track

The following section treats the reconstruction of tracks from charged particles in three dimensions. The (x, y) position is defined by the spatial position of the Micromegas pads which registered a signal (see figure 4.9a for comparison). The z position has to be reconstructed in an indirect way. Parallel to the beam line, the occurring electrons drift towards the Micromegas pads, as shown in figure 4.6. Hence, the drift time the electrons take to reach the Micromegas pads is related to the z position of their creation. This time dependent charge deposition in each Micromegas pad can be described by [91]

$$q(t) = A \cdot \exp\left(-3\frac{t - t_{pad}}{\tau}\right) \cdot \sin\left(\frac{t - t_{pad}}{\tau}\right) \cdot \left(\frac{t - t_{pad}}{\tau}\right) + q_b, \tag{4.12}$$

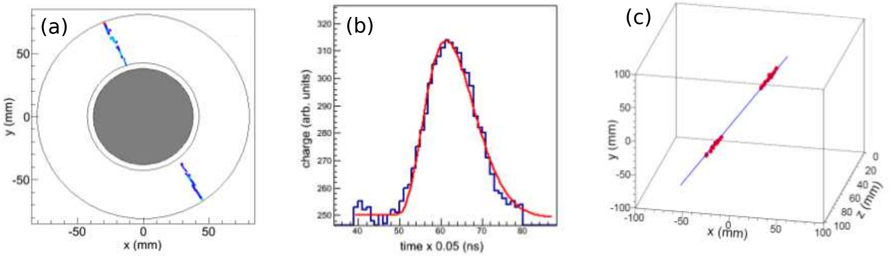

Figure 4.9.: Illustration of the MINOS vertex reconstruction. The data corresponds to a cosmic-rays test run. Figure (a) shows a plot of the (x, y) positions of the Micromegas pads which registered a signal. A signal of a single Micromegas pad fitted with the function of equation 4.12 is depicted in (b). A reconstructed track combining z_{pad} and (x, y) from figure (a) is shown in (c). The figure is taken from [92] and slightly modified.

with the trigger time t_{pad}, the amplitude A, the shaping time τ and the signal base line q_b. The base line q_b is a constant depending on the electronics. A comparison of the analytical description and the measured Micromegas pad signal is shown in figure 4.9b. Fitting the obtained time signal produced in the TPC with the analytical function $q(t)$ yields the trigger time t_{pad}. Considering that the extracted time is relative to the acquisition trigger time t_0 the z position z_{pad} results to [92]

$$z_{pad} = v_{drift} \cdot \left(t_{pad} - t_0\right), \tag{4.13}$$

where v_{drift} is the drift velocity of the electrons in the TPC gas. While the offset t_0 stays constant over the experiment, the drift velocity v_{drift} has to be monitored during the experiment (see section 5.2). Since the TPC is not fully air tight, changes of the gas impurities can occur. Using the obtained z position together with the (x, y) positions obtained from the positions of the Micromegas pads, it is possible to reconstruct the position of the electron creation and therefore the tracks of the charged particles through the TPC (see figure 4.9c). The tracking algorithm used to reconstruct the tracks was developed within the PhD thesis of C. Santamaria [92] and is briefly described in the following. The information of the (x, y) positions obtained by the positions of the Micromegas pads (compare figure 4.9a) are treated as one event which is analyzed by a 2D Hough transform [99]. The Hough transform identifies straight lines inside the multiple points of a track in the (x, y) plane. Events that do not consist of at least ten pad signals or not more than one pad signal of the four inner rings are discarded and evaluated as background events. In the following step, the z coordinate calculated by the trigger time t_{pad} and the drift velocity v_{drift} is used to perform a 3D Hough transform in order to filter the tracks and extract the three dimensional image of the proton track. For a $(p,2p)$ reaction, creating two outgoing protons, the mid-point of the minimal distance between the two tracks serves as reaction vertex since it is unlikely that the tracks have a common crossing point. If only one proton was detected, the algorithm connects the ion track obtained by the double PPACs at the focal point F8 with one proton path in order to reconstruct the reaction vertex. For a more detailed description of the algorithm, the author refers to [92].

4.4 DALI2

The detector array for low intensity radiation (DALI2) consists of 186 NaI(Tl) scintillators and is used for in-beam γ-ray spectroscopy at RIBF. DALI2 consists of three different types of NaI(Tl) scintillators:

- 32 crystals were manufactured for the predessesor DALI by BICRON and cover a volume of $60 \times 60 \times 120$ mm^3.
- 66 crystals cover a volume of $45 \times 80 \times 160$ mm^3 and are fabricated by SAINT-GOBAIN.
- 88 crystals were produced by SCIONIX covering a volume of $40 \times 80 \times 160$ mm^3.

Each detector has an 1 mm thick aluminum housing and is connected to a photomultiplier tube (PMT) from Hamamatsu. The detectors are arranged in eleven layers, ten layers perpendicular to the beam line, and one parallel to the beam axis (compare figure 4.10). The first six layers, counted in beam direction, are equipped by detectors from SAINT-GOBAIN. In the following four layers, crystals produced by SCIONIX are in use. The final layer, covering the smallest detection angles in forward direction, consists of 64 crystals (32 crystals by BICRON and SCIONIX each) oriented parallel to the beam axis. The full DALI2 array covers polar angels from 10° to 128° with respect to the central beam axis and the center of MINOS. As implied by the figures 4.10, MINOS is not placed in the center of DALI2, but shifted 16.5 cm upstream. DALI2 can detect several γ-rays at the same time. The amount of simultaneous γ rays is counted by the quantity of the multiplicity. In addition, addback of close γ-ray hits can be performed. Therefore, a distance of 15 cm is defined, within which simultaneous energy depositions are summed up.

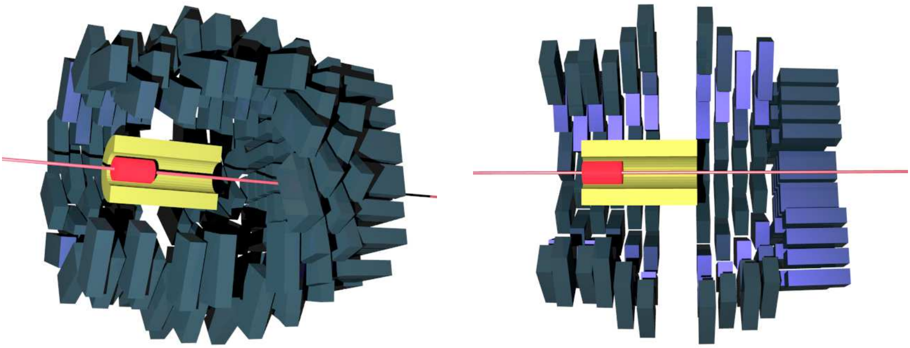

(a) Some of the DALI2 crystals perpendicular to the beam line are not shown, since they would obstruct the view on the inside.

(b) Half of the DALI2 sphere is removed; observer watches from the side.

Figure 4.10.: Schematic picture of DALI2 with MINOS inside. The beam comes from the left and impinges on the LH2 target in red. The MINOS TPC in yellow surrounds the target. The DALI2 crystals are shown in blue.

This distance is called addback distance and was used for the whole analysis.
By a simulation with the GEANT4 framework [100], full-energy peak detection efficiencies of 35% (23%) were obtained for a 500-keV (1-MeV) γ ray (with addback), emitted from a nucleus at the target center moving with a kinetic energy of 250 MeV/u. Five transitions ranging from 662 keV to 1.836 MeV from ^{137}Cs, ^{88}Y, and ^{60}Co sources were used for an energy calibration (for more details see section 5.3). A calibration error of 1.5 keV and an energy resolution of 9% (6%) FWHM at 662 keV (1.332 MeV) were obtained, in agreement with the characteristics of DALI2 [93].

4.5 Data acquisition and trigger

For data acquisition and the trigger logic, five subsystems and their detectors have to be considered:

TEGICs

The SEASTAR 2015 setup uses two TEGIC detectors, one at F7 and a second at F11. The six signals of the six anodes from each TEGIC are processed by a shaping amplifier and forwarded to a charge to digital converter (QDC).

PPACs

In total twelve PPACs are installed, while a pair of PPACs (double PPACs) are operated at F3, F5, F7, F8, F9, and F11. Each PPAC provides five signals which are further amplified. The timing information of the signals is obtained by a constant fraction discriminator (CFD) and digitized by a time-to-digital converter (TDC).

Plastic scintillators

Plastic scintillators are used at F3, F7, F8, and F11 in BigRIPS and ZeroDegree. They are read out by two photomultiplier tubes on two opposite sides of the plastic scintillator. The obtained signals of the two photomultipliers are divided into two. One is forwarded to a QDC to obtain an energy information, whereas the second signal is sent to a leading edge discriminator (LED) and is digitized by TDC afterwards. The fast LED outputs of opposite PMTs were used to create the trigger of each plastic scintillator. During the SEASTAR campaign, only the triggers of the plastic scintillators at F7 and F11 were used.

DALI2

The signals of the 186 DALI2 crystals were amplified and the normal amplifier output was digitized by an analog to digital converter (ADC). The fast output of the amplifier was digitized by a multi-hit TDC. To generate a γ trigger an OR signal of all crystals was applied.

MINOS

Customer specific chips read out the data of the 4068 Micromegas pads.

From the subsystems described previously, the following triggers have been formed:

- **F7(DS):** Incoming rate in BigRIPS using a downscale factor (DS) to account for the high rates. The signal is generated by a rate divider. By setting a specific proportion (such as 1/50), the module only provides this fraction of events (every 50th). This trigger serves as hardware trigger during the experiment.
- **F7×F11:** Incoming rate in BigRIPS transmitted to ZeroDegree.
- **F7×F11×γ:** Incoming rate in BigRIPS transmitted to ZeroDegree together with a registered γ ray in DALI2. This trigger was used as hardware trigger during the experiment.

Finally, the system's dead time has to be considered. Therefore, the SEASTAR 2015 setup was operated as common-dead-time system. The five subsystems created an end-of-busy signal which was combined with an AND. This signal was sent to the system and has been a requirement in oder to process the next event. Beside this, a coincidence register was used to catalog the different coincidence measured by the two hardware triggers. The coincidence register used the F7(DS), F7×F11, and F7×F11 $\times\gamma$ signals as input. The output of this module is called *fbit* and was stored on disk just as the rest of the data. The coincidence module assigns a certain *fbit* value to each of the three triggers. F7(DS) has the value *fbit* $==1$, F7×F11 is assigned to *fbit* $==2$, and F7×F11 $\times\gamma$ is referred to as *fbit* $==4$. For combinations of different trigger conditions these values are summed up, leading to *fbit* $==3$ for the trigger conditions (F7(DS))&&(F7×F11). A complete list of the used *fbit*'s and the corresponding trigger condition is given in table 4.1.

Table 4.1.: Correspondence of *fbit* to the trigger conditions.

fbit	**Trigger condition**
1	F7(DS)
2	F7×F11
3	(F7(DS))&&(F7×F11)
4	F7×F11 $\times\gamma$
5	(F7(DS))&&(F7×F11 $\times\gamma$)
6	(F7×F11)&&(F7×F11 $\times\gamma$)
7	(F7(DS))&&(F7×F11)&&(F7×F11 $\times\gamma$)

5 Data analysis

In the preceding chapter the experimental setup used for the SEASTAR campaign 2015 with its detector systems was presented. The following chapter, gives an examination of the detector systems' correct functionality and a description of the different stages of the data analysis.
The data analyzed in this work has been collected in three different BigRIPS and ZeroDegree settings shown in Table 5.1. Each of the settings is portioned in runs of $\sim$ 1h duration.

Table 5.1.: Characteristics of the three settings applied to collect the data.

Parameter	**Setting** 1	**Setting** 2	**Setting** 3
Isotope centered in BigRIPS	^{85}Ga	^{89}As	^{95}Br
Isotope centered in ZeroDegree	^{84}Zn	^{88}Ge	^{94}Se
^{238}U beam current at the ^{9}Be target (pnA)	~ 35	~ 30	~ 30
Rate at F3 (s^{-1})	~ 6500	~ 6000	~ 6500
Rate at F7 (s^{-1})	~ 5500	~ 5000	~ 6000
Rate at F11 (s^{-1})	~ 700	~ 800	~ 2500
Energy in front of the reaction target (MeV/u)	~ 280	~ 260	~ 270
Measurement period (h)	~ 21	~ 10.5	~ 35

5.1 BigRIPS and ZeroDegree

In order to perform the particle identification in BigRIPS and ZeroDegree as described in section 4.2, the correct operability of the used detector systems was verified first. The necessary checks of the TOF measurement using the plastic scintillators are presented in section 5.1.1. Subsequently, section 5.1.2 treats the tests required for a proper position reconstruction by the PPAC system and section 5.1.3 deals with the determination of the ions' atomic number with the TEGICs. Afterwards, the obtained quantities are used to construct a particle identification in BigRIPS and ZeroDegree. Applied optimizations of the particle identification are described in section 5.1.4. The analysis chapter of BigRIPS and ZeroDegree closes with the description of the $B\rho$ consistency before and after the degrader at F5, which is used to suppress unwanted background.

5.1.1 Plastic scintillators - Time of flight measurement

A distinct selection of the particles in BigRIPS and ZeroDegree is ensured by a measurement of the ions' mass over charge ratio (A/Q) and a measurement of their energy loss (dE/dx), as discussed in section 4.2.1. The A/Q described by equation 4.1, depends on two observables, the magnetic rigidity ($B\rho$), and the velocity (v) of the ions, which have to be measured. The ions' velocity v is obtained by a time of flight (TOF) measurement. Therefore, plastic scintillators are placed at the beginning and at the end of BigRIPS and ZeroDegree, as explained in section 4.2. Two photomultipliers (PMTs), one placed on each side of the scintillation counter, collect the scintillation light. The PMT signals are used to obtain the timing information of the pulse as well as the total charge collected. The proper operation of the plastic scintillators can be ensured by the position information x obtained from the timing information (t_1 and t_2) and the total charge collected (q_1 and q_2) from both PMTs of each scintillator [87]:

$$x = -\frac{V}{2}\left(t_2 - t_1\right), \tag{5.1}$$

$$x = -\frac{\lambda}{2}\ln\left(\frac{q_1}{q_2}\right), \tag{5.2}$$

where λ denotes the attenuation length and V the propagation speed of light in the scintillating material. The correlation of the positions obtained by the timing information and the total charge collected are shown in figure 5.1 for the scintillators placed at F3, F7, F8, and F11. For each of the four scintillators, a clear correlation

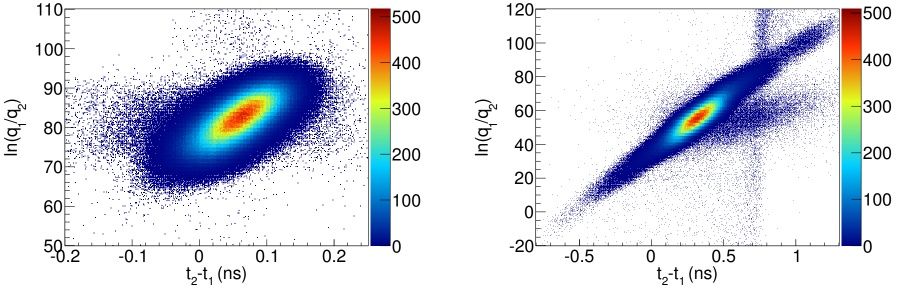

(a) Plastic scintillator at F3.

(b) Plastic scintillator at F7.

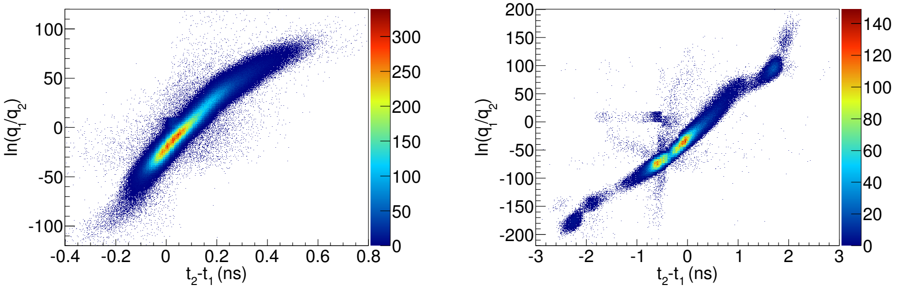

(c) Plastic scintillator at F8.

(d) Plastic scintillator at F11.

Figure 5.1.: Correlations of the time differences $t_2 - t_1$ and the logarithmic charge ratios $\ln(q_1/q_2)$ of both PMTs reading out the plastic scintillators at F3, F7, F8, and F11.

indicating their proper operation arises. In order to obtain the presented correlations a part of the data from setting 1 was used.

A time $T(\mathrm{F})$ independent of the position where the ions cross the plastic scintillator, describing the time at which the ions pass the scintillator, is calculated by the average of the times obtained from the left and right PMT.

$$T(\mathrm{F}) = \frac{1}{2}\left(t_1(\mathrm{F}) + t_2(\mathrm{F})\right). \tag{5.3}$$

Here, F indicates the position of the scintillation counter. Using the time the ions pass the scintillation counter $T(\mathrm{F})$, the TOF for BigRIPS (F3 - F7) and ZeroDegree (F8 - F11) is determined by:

$$TOF_{37} = T(\mathrm{F7}) - T(\mathrm{F3}) + T_{offset,37}, \tag{5.4}$$

$$TOF_{811} = T(\mathrm{F8}) - T(\mathrm{F11}) + T_{offset,811}, \tag{5.5}$$

where $T_{offset,37}$ and $T_{offset,811}$ are offsets due to delays of the used electronics. The two offsets obtained for the different settings are given in table 5.2. The offsets from setting 3 are taken from [101]. How these offsets are determined is described in section 5.1.4. The time of flight obtained in this way is used for the particle identification (section 5.1.4).

Table 5.2.: Obtained TOF offsets.

Setting 1		**Setting 2**		**Setting 3**	
$T_{offset,37}$	$T_{offset,811}$	$T_{offset,37}$	$T_{offset,811}$	$T_{offset,37}$	$T_{offset,811}$
304.4 ns	−162.84 ns	304.15 ns	−162.6 ns	304.2 ns	−162.15 ns

5.1.2 PPACs - Position reconstruction

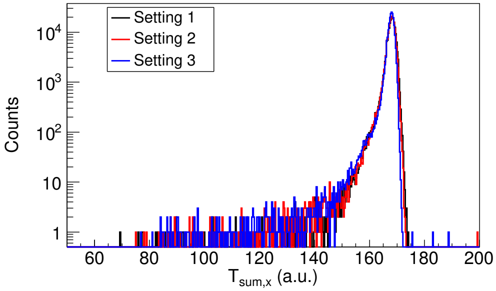

Figure 5.2.: $T_{sum,X}$ for PPAC F71A.

Section 4.2.2 describes the reconstruction of the ion trajectories using the PPACs in BigRIPS and ZeroDegree. The reconstruction is the basis to extract the magnetic rigidity ($B\rho$) of the concerned ions in BigRIPS and ZeroDegree. In order to ensure the correct operation of the PPACs, the consistency of the obtained events is examined in terms of the sum of the delay times $T_{sum,X}$ and $T_{sum,Y}$, as explained in section 4.2.2. As an example, figure 5.2 shows $T_{sum,X}$ of PPAC F71A (first PPAC of the doublet A at focal point F7) for the three different settings. A pronounced peak is observed for all settings indicating a consistent T_{sum}, i.e. the proper functioning of the shown PPAC. The verification of a reasonable $T_{sum,X}$ was performed for all PPACs used. Beside the consistency of the PPAC events, the PPAC efficiency is an important measure of the quality of the particle reconstruction in BigRIPS and ZeroDegree. The PPAC efficiency is obtained by the ratio of events counted in the plastic scintillator at F7 relative to the events counted in each PPAC. For this purpose, ^{87}As was required in BigRIPS and ZeroDegree. Table 5.3 presents the derived results. All the efficiencies are $\sim$ 90% or even higher. In this context, it is essential to know that the position reconstruction for every ion is performed at each focal plane, using the position information of the four PPACs installed there. To obtain a distinct position reconstruction for every ion, the information of two PPACs at each focal plane is sufficient. Therefore, the PPAC efficiencies presented in table 5.3 are smaller than the effective efficiency for the position reconstruction of the passing ions. This consistency check shows a proper functioning of the PPACs.

Table 5.3.: PPAC efficiencies, obtained by the registered counts in each PPAC relative to the counts registered in the plastic scintillator at F7. The efficiencies are calculated using the data from setting 1, requiring a particle identification of ^{87}As in BigRIPS and ZeroDegree.

	PPAC	Efficiency (%)	PPAC	Efficiency (%)
BigRIPS	F31A	91.7	F31B	90.3
	F32A	89.3	F32B	87.2
	F51A	90.4	F51B	98.0
	F52A	94.6	F52B	96.8
	F71A	97.2	F71B	97.5
	F72A	96.0	F72B	98.5
ZeroDegree	F81A	99.5	F81B	98.6
	F82A	99.2	F82B	97.4
	F91A	94.6	F91B	96.6
	F92A	98.5	F92B	94.4
	F111A	99.7	F111B	94.4
	F112A	91.3	F112B	99.0

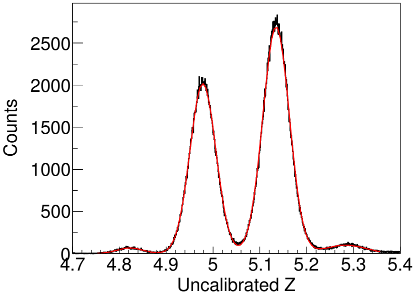

Figure 5.3.: Energy loss spectrum of the TEGIC at F7 during a data run from setting 1, fitted by Gaussian functions in red.

As explained in section 4.2.3, TEGICs placed at F7 and F11 in BigRIPS and ZeroDegree are used to measure the energy loss of the passing ions and therefore their atomic number. The energy loss of each ion inside a TEGIC is calculated by the geometric average of the anode signals. Figure 5.3 shows an example of an energy loss spectrum for the TEGIC placed at F7 in BigRIPS during a data run from setting 1. In order to obtain the centroid peak positions, the energy loss spectrum is fitted by Gaussian functions shown in red. In a next step, the obtained centroid peak

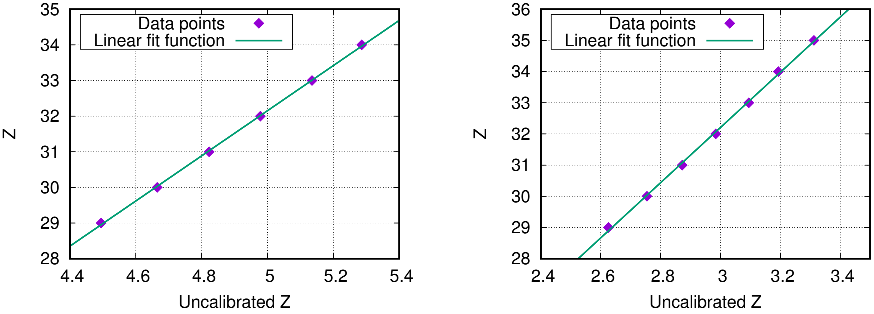

(a) TEGIC at F7.

(b) TEGIC at F11.

Figure 5.4.: Calibration of the TEGICs. The calibration is shown for data from setting 1.

positions are assigned to their corresponding atomic number Z by a linear fit. The assignment of Z is established by the isomer tagging method [87, 102], which is done by the BigRIPS team during the experiments. Their assignments are accessible for the experimentalists and are used within this work. The corresponding fit of the centroid peak positions, obtained from the energy loss spectrum, to the known Z is shown in figure 5.4a for the TEGIC at F7 in BigRIPS and in figure 5.4b for the TEGIC at F11 in ZeroDegree. The illustrated calibration is used in the analysis of setting 1 and has been performed for the additional settings in the same way. Regarding setting 3, the calibration was taken from [101].

5.1.4 Particle identification

A distinct identification of the ions passing the BigRIPS fragment separator and the ZeroDegree spectrometer is enabled by the knowledge of the ions' Z and their mass over charge ratios (A/Q). Thus, the information obtained in sections 5.1.1 to 5.1.3 is applied. While Z is received straight from the TEGICs, the A/Q is calculated from the magnetic rigidity ($B\rho$), extracted from the PPAC position reconstruction, and the time of flight measurement (TOF), performed with the plastic scintillators.
The A/Q is given by equations 4.1 - 4.6 in section 4.2.1. For the BigRIPS fragment separator the $B\rho$s of the two magnetic stages F3 to F5, and F5 to F7, together with the TOF_{37} are used to calculate the A/Q, since a degrader is placed at F5. Since no degrader or wedge is used in ZeroDegree, the $B\rho$s in stages F8 to F9, and F9 to F11 are the same. Because of this reason, a separate consideration of these stages is not needed for the A/Q calculation. For the further analysis, the $B\rho$ of stage F9 to F11 combined with the TOF_{811} is used to calculate the A/Q in the ZeroDegree spectrometer. The TOF offsets, $TOF_{offset,37}$ and $TOF_{offset,811}$, listed in table 5.2, are chosen in such a way that the resulting A/Q of the ions of interest match the assignments from the isomer tagging performed by the BigRIPS team, as described in section 5.1.3.
In the following, the A/Q is optimized according to [87], causing a better A/Q resolution, and therefore, a better separation of the ions passing the BigRIPS fragment separator and the ZeroDegree spectrometer and therefore a better selection of the reaction channels. This optimization method is based on the fact that the deduced A/Q for any isotope should be independent of the position and angle measured by the PPAC system at the focal points along the beam line of BigRIPS and ZeroDegree. Figure 5.5a and 5.5c show the correlation of A/Q and the measured position and angle at focal point F9 in ZeroDegree for data from setting 1. In order to avoid a cluttering of the shown plot, arsenic isotopes are selected in BigRIPS and ZeroDegree. The dependence on both quantities (position and angle) is clearly visible.

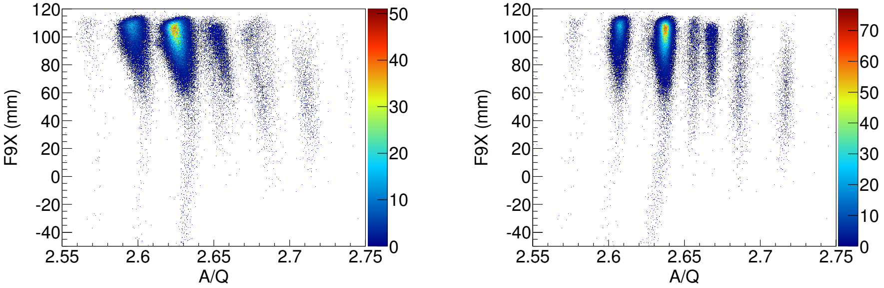

(a) Without A/Q corrections.

(b) A/Q corrections implemented.

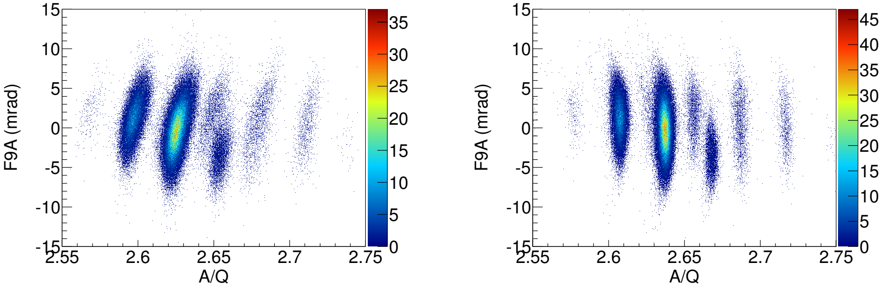

(c) Without A/Q corrections.

(d) A/Q corrections implemented.

Figure 5.5.: Impact of the A/Q corrections demonstrated at the focal point F9 of ZeroDegree. In panel a) and b) A/Q is plotted against the position at F9, while A/Q is plotted against the measured F9 angle in panel c) and d). Uncorrected correlations are shown in panel a) and c), the effect of the A/Q correction is displayed in panel b) and d). These plots use a cut on arsenic in order to avoid a cluttering of the figures.

Correcting these dependencies, a polynomial function is fitted to the two dimensional plots 5.5a and 5.5c. The obtained polynomial coefficients $c_{F9,x}$ and $c_{F9,\alpha}$ are subtracted from the A/Q value in the next step. The impact of this correction is depicted in figure 5.5b and 5.5d. The correlation of A/Q and the measured x-positions and angles vanishes. Performing such a fit at every focal point, the optimized mass over charge ratio A/Q_{opt} for the ZeroDegree spectrometer can be calculated to

$$\begin{aligned} A/Q_{opt} = A/Q &+ c_{F9,x} \times x_{F9} + c_{F9,x^2} \times x_{F9}^2 \\ &+ c_{F9,\alpha} \times \alpha_{F9} + c_{F9,\alpha^2} \times \alpha_{F9}^2 \\ &+ c_{F11,x} \times x_{F11} + c_{F11,x^2} \times x_{F11}^2 \\ &+ c_{F11,\alpha} \times \alpha_{F11} + c_{F11,\alpha^2} \times \alpha_{F11}^2, \end{aligned} \tag{5.6}$$

where x_{Fx} and α_{Fx} are the positions and angles measured by the PPAC system at the focal point Fx. The correlations of A/Q and A/Q_{opt} with the measured positions and angles for all the focal points are shown in appendix A.1.

Figure 5.6 shows the impact of the A/Q optimization for BigRIPS (figure 5.6a) and ZeroDegree (figure 5.6b). The initial distribution of A/Q is shown in red while the optimized A/Q_{opt} is depicted in black. Comparing the results from BigRIPS and ZeroDegree it can be seen that the optimization effect is stronger in ZeroDegree. A distinct separation of the peaks in the A/Q distribution was already given in BigRIPS before the optimization. In this case, the major influence is due to the reduction of the peak width. Nonetheless, the optimization procedure helps strongly to separate the peak structures in ZeroDegree. The newly obtained A/Q_{opt} simplifies the selection of a nucleus with its certain value of A/Q. The optimization of A/Q has been performed for setting 2 in the same way while the optimization coefficients for setting 3 are taken from [101].

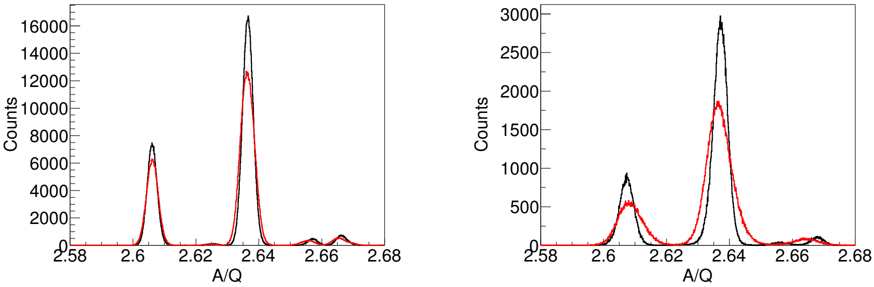

(a) Comparison for BigRIPS.

(b) Comparison for ZeroDegree.

Figure 5.6.: Comparison of the A/Q distribution before (red) and after (black) the A/Q optimization procedure described in the text. The plots use a cut on arsenic isotopes to avoid overlapping peak structures.

5.1.5 Charge state removal

Comparing $B\rho$ before and after the degrader at F5, charge states and reacted particles can be excluded. The goal of the degrader is to decelerate the passing ions depending on their proton number Z. In this case, $B\rho$ of a certain isotope changes slightly but the ratio stays constant. Ions that undergo a reaction, loose or receive electrons while passing the degrader and their $B\rho$ changes significantly. Although the ratio stays constant for these ions, it is distinct from those decelerated ions which do not change their electron configuration. This fact is illustrated in figure 5.7 by plotting the magnetic rigidity before the degrader $B\rho_b$ versus the ratio of the magnetic rigidities before and after the degrader $B\rho_b/B\rho_a$. The shown figure presents data from setting 1 gated on ^{87}Ge in BigRIPS. Ions simply decelerating inside the target possess a ratio $B\rho_b/B\rho_a \approx 1$, while reacting ions and those changing their charge state end up with a ratio different from 1. For the following analysis, the ions with a ratio $B\rho_b/B\rho_a$ around 1 are selected. The same $B\rho$ consistency check is performed for all considered knock-out reactions.

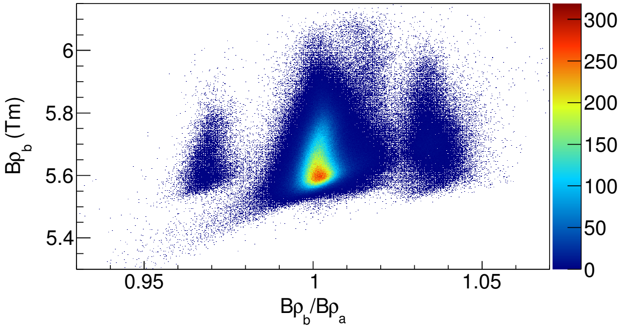

Figure 5.7.: Illustration of the $B\rho$ consistency check for the reaction channel ^{87}As$(p,2p)^{86}$Ge of setting 1. The magnetic rigidity before the degrader $B\rho_b$ is plotted versus the ratio of the magnetic rigidities before and after the degrader $B\rho_b/B\rho_a$. Different constant ratios arise from unreacted and reacted ions changing their charge state.

5.2 MINOS calibration

MINOS, the liquid hydrogen target surrounded by a TPC, is used to reconstruct each reaction position inside the target and therefore to improve the Doppler-correction, as described in section 4.3. To ensure a proper reconstruction of the position along the beam axis z, the drift velocity v_{drift} is vital (compare equation 4.13). Due to varying gas impurities and therefore a changing v_{drift}, it is necessary to determine v_{drift} run by run (one run is $\sim$ 1h). Figure 5.8 shows the distribution of all trigger times t_{pad} obtained by equation 4.12 for a certain run of the experiment. The smallest times t_{min} correspond to electrons ionized in the periphery of the Micromegas, requiring the shortest time, i.e. no drifting towards the Micromegas pads. The electrons created at the cathode, on the other side of the TPC chamber, need to cross the entire gas volume of 300 mm length. Therefore, they take the longest time t_{max}. For this reason, the length of the TPC chamber is reflected by the two times t_{min} and t_{max}. It is important to notice that the minimum trigger time t_{min} does not depend on the drift velocity, but on the DAQ trigger and the MINOS electronics. Since these components did not change during the experiment, a common trigger time t_{min} is obtained for the whole SEASTAR campaign. Figure 5.8 shows a small increase of counts at small trigger times, t_{min} is taken at the top of this slope. In contrast to this, a sharp edge is visible for high trigger times, reflecting the drift velocity dependent nature of t_{max}. The maximum trigger time t_{max} is set to be at

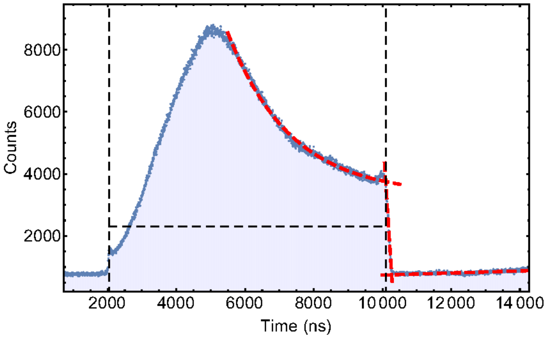

Figure 5.8.: Distribution of all trigger times for one run shown in blue. The vertical, black, dashed lines mark the trigger times t_{min} and t_{max}, while the horizontal, black, dashed line illustrates the target length reflected by those two times. The red functions are used to obtain t_{max}. See text for details.

the middle of the falling edge. Thus, t_{max} is derived by a fit of two polynomial functions and a combination of a polynomial and exponential function, as shown in figure 5.8.

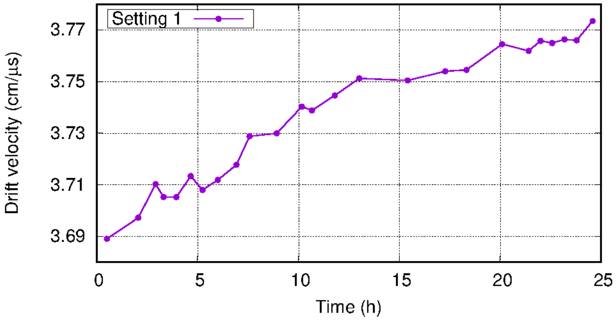

Figure 5.9.: Behavior of the obtained drift velocities v_{drift} for setting 1. The presented time corresponds to the elapsed time after the start of the experiment. For each run the drift velocity is shown at the temporal middle of the run.

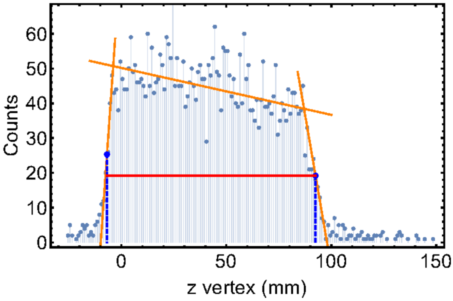

Figure 5.10.: Reconstructed vertex positions, reflecting the length of the MINOS target. The target length indicated by the red line is obtained by a fit of three linear functions (orange).

Since t_{max} depends on the drift velocity, it has to be monitored run by run. By knowing t_{max} and t_{min} and using equation 4.13, the drift velocity can be calculated to [92]

$$v_{drift} = \frac{L_{TPC}}{t_{max} - t_{min}}, \tag{5.7}$$

with $L_{TPC} = z_{cathode} - z_{Micromegas} = 300$ mm being the length of the TPC. The behavior of the drift velocity for setting 1 is shown in figure 5.9 and for setting 2 in appendix A.2, while t_{max} for setting 3 is taken from [101]. The obtained drift velocities serve as calibration of the TPC and are used within the tracking algorithm described in section 4.3.2. Cross checking the obtained results, the reconstructed vertex positions of each run are analyzed, as shown in figure 5.10. In case of a proper operation of the algorithm and a correct calibration of the TPC, the distribution of the reconstructed vertex position should reflect the length of the liquid hydrogen target. Therefore, the width of the obtained vertex distribution is determined by a fit of three polynomial functions to the distribution, as shown in figure 5.10. The beginning and the end of the target are committed to be at the middle of the falling edge on each side of the distribution. The resulting target length obtained run by run for setting 1 is shown in figure 5.11 and is in good agreement with the target length of 100 mm (compare section 4.3.1).

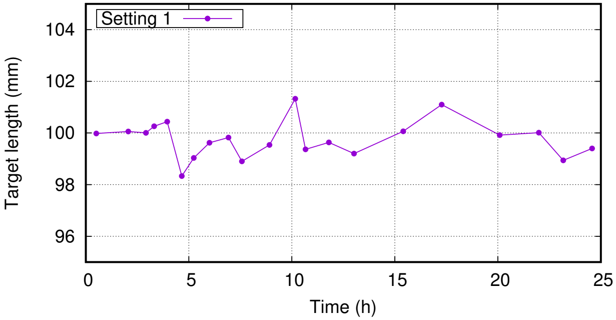

Figure 5.11.: Robustness of the MINOS data demonstrated by the reconstructed target length for setting 1. The presented time corresponds to the elapsed time after the start of the experiment. For each run the target length is shown at the temporal middle of the run.

5.3 DALI2 calibration

5.3.1 Energy calibration

The three sources ^{137}Cs, ^{88}Y, and ^{60}Co serve for the energy calibration of DALI2. One γ ray at 661.66 keV [103] is emitted after the decay of ^{137}Cs. The decay of a

^{60}Co source is followed by two characteristic γ-ray transitions at 1173.23 keV and 1332.49 keV [104] while γ rays at 898.04 keV and 1836.06 keV [105] are emitted after the decay of ^{88}Y. A calibration run was done for each source independently and took $\sim$ 0.5 h for which the sources were put at the end of the beam pipe housing MINOS. The calibration data for setting 1 and 2 were taken before the experimental runs. In case of setting 3, the calibration was taken from [101]. The observed photopeaks in each source run are fitted with a Gaussian function combined with a polynomial function. An example of such a fit for detector 72, located at the first ring after the gap in beam direction (compare figure 4.10), during the calibration run with the ^{60}Co source before the data run of setting 1 is shown in figure 5.12a. At this point, the central peak position of each of the five transitions in units of ADC channels is localized for all the 186 DALI2 detectors. Afterwards, the obtained ADC channels for each DALI2 detector are assigned to the corresponding transition energies by a fit of a second order polynomial function. This is exemplarily shown in figure 5.12b for detector 72. The validity of the DALI2 calibration is checked by an analysis of the calibration data using the energy calibration obtained before. Doing so, the residuum defined as the measured energy subtracted by the tabulated energy of the transition can be obtained. Figure 5.13 shows the resulting residues of the 186 DALI2 detectors of the ^{137}Cs calibration runs from setting 1 and 2. The residues for the γ-ray transitions of the ^{88}Y and ^{60}Co sources are shown in appendix A.3. The plots agree with an uncertainty of 1.5 keV for most of the DALI2 detectors. From the fits performed for the energy calibration the detector

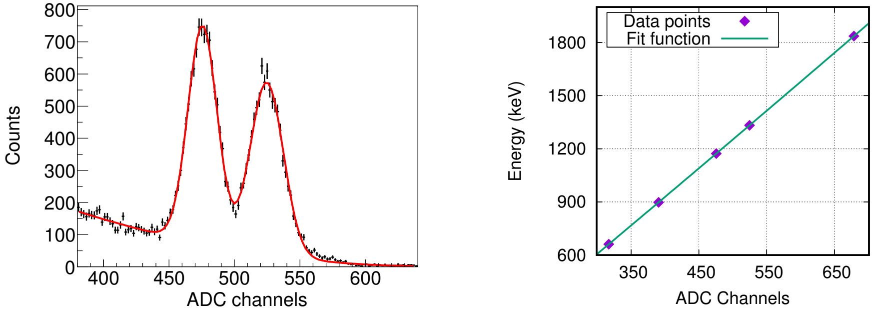

(a) Fit of the photopeaks from the ^{60}Co source to obtain their centroid positions.

(b) Quadratic fit of the centroids from the five transitions.

Figure 5.12.: Energy calibration performed for the DALI2 array. Examples are given for detector 72 and the calibration run before setting 1.

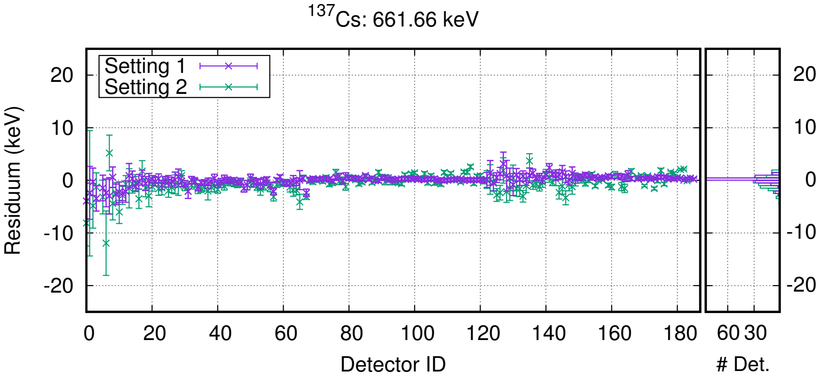

Figure 5.13.: Residues of the 661.66 keV transition after the ^{137}Cs decay, defined as energy difference of the measured and tabulated energy for each detector (left). Projection of the residues for all detectors (right).

resolution (σ) is obtained in addition. The results for the five transitions of the three sources used in the first setting are shown in figure 5.14. The same analysis

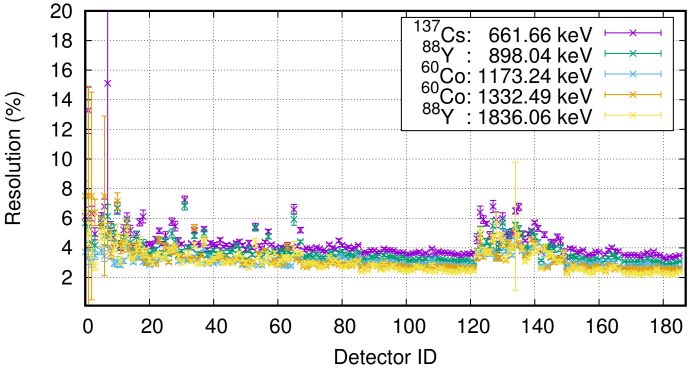

Figure 5.14.: σ resolution of DALI2 in percent for different transition energies.

was performed for setting 2 which is shown in appendix A.3. Both figures illustrate that the resolution is below 5% for most of the detectors. Only for IDs $\lesssim 30$ and IDs from ∼(120-145) the resolution is worse. This can be explained by the fact that the worst detectors are used in the first layers (backward angles) of DALI2 and that the crystals with IDs ∼(120-145) are shielded by other detectors causing smaller chances of a full-energy deposition. The width of the photopeak is proportional to the square root of the transition energy for a scintillation counter [106]. Therefore, the relation

$$\sigma = c \times \sqrt{E/\mathrm{keV}} \quad (\mathrm{keV}), \tag{5.8}$$

serves to describe the energy dependent behavior of the energy resolution. Figure 5.15 shows a fit of the square root behavior to the obtained resolutions from detector 175. This procedure is performed for all the detectors individually. The extracted fit functions for each DALI2 crystal are used as input for the simulation described in section 5.5. The fit functions describing the individual detector resolution for setting 3 were taken from [101].

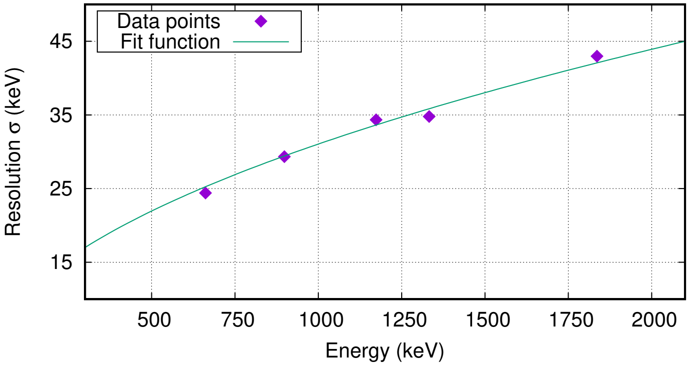

Figure 5.15.: Square root behavior $\sigma = 0.98(1)\mathrm{keV}\sqrt{E/\mathrm{keV}}$ of the DALI2 detector with ID 175.

5.3.2 Time calibration

The time calibration was performed by aligning the time distribution of all DALI2 detectors to each other. A typical raw time spectrum of a DALI2 detector is shown in figure 5.16a for the detector with ID 62, exemplarily. The time spectra of all the detectors are aligned in such a way that the maximum of the prompt response is shifted to the time 0 ns for all detectors. The time alignment for all the detectors is shown in figure 5.16b. It can be seen that the maximum of the prompt peak is located at 0 ns for all the detectors. The shown data correspond to setting 1.

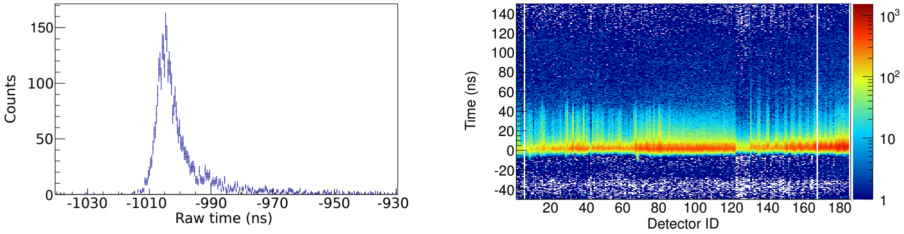

(a) Raw DALI2 time spectrum for the detector with ID 62.

(b) Aligned DALI2 times vs detector ID.

Figure 5.16.: Time spectrum before the calibration, shown for one detector (a), and for all detectors after the calibration (b).

Setting 2 has been calibrated in the same way while for setting 3 the calibration was taken from [101].

5.4 Doppler-correction

After the fragmentation process and the steering through the BigRIPS fragment separator, the nuclei of interest impinge onto the liquid hydrogen target with a kinetic energy higher than 250 MeV/u corresponding to a velocity above $\beta = 0.62c$. While passing through the target, their energy is reduced by $\sim$ 70 MeV/u corresponding to a reduction of their velocity of $\beta = 0.06c$. The energy E_γ of the γ radiation emitted from nuclei in motion, which are excited by reactions with the hydrogen target, is shifted according to the Doppler formula and has to be corrected by

$$E_0 = E_\gamma \frac{1 - \beta \cos \vartheta}{\sqrt{1 - \beta^2}}, \tag{5.9}$$

where E_γ is the detected energy of the γ ray which is transformed to its energy at rest E_0. The velocity at which the γ ray was emitted is β and ϑ describes the emission angle of the γ radiation with respect to the direction of motion of the emitting nucleus.

As discussed in section 4.3, MINOS can be used to improve the quality of the Doppler-correction. As further described, MINOS can reconstruct the reaction vertex by the detection of the emitted protons originating from reactions inside the target. Even if the reaction vertex and the position at which the γ radiation is emitted are not the same (except the half-life of the excited state would be zero) the vertex tracking of MINOS restricts the information significantly. A nucleus moving with a velocity of $0.6c \approx 0.18$ mm/ps reaches 18 mm in 100 ps, which is a short distance compared to the target length of 100 mm. While the time 100 ps is long compared to the half-life considered at such setups. Furthermore, the usage of MINOS depends on the reaction characteristics. Considering a (e.g.) (p,p') reaction the nucleus transfers too little energy to the proton, therefore, it cannot leave the target and reach the MINOS TPC in order to be detected. For this reason, the Doppler-correction is performed in various ways for different reactions. This is illustrated in figure 5.17. In the cases where the protons receive enough energy

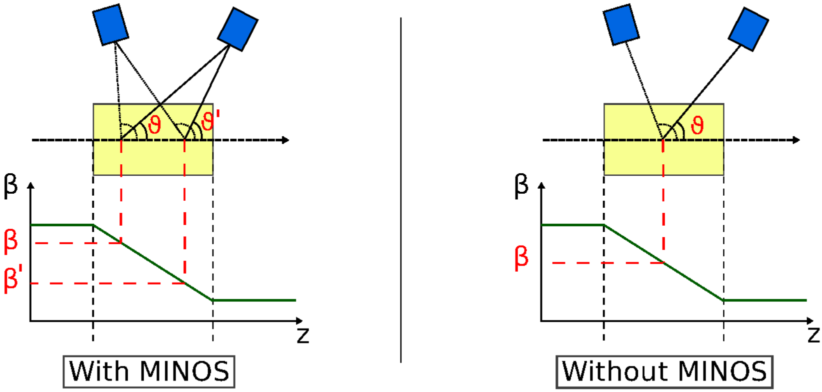

Figure 5.17.: Illustration of the information used for the Doppler-correction with and without MINOS. The usage of MINOS allows a more precise reconstruction of the γ-rays emission angle ϑ and improves the information on the ions velocity β.

to leave the liquid hydrogen target, like $(p,2p)$, (p,pn), $(p,2pn)$, or $(p,2p2n)$ reactions, MINOS can be used. The angle ϑ, describing the direction of the γ-ray emission, depends on two quantities, the position of the γ emission and the detection position in DALI2. The effective first interaction point obtained by a Monte Carlo simulation was used as interaction point inside DALI2, what takes the overlapping of the DALI2 crystals and the occurring Compton effects inside the detector material into account. The usage of MINOS plays a key role for the precision of the reconstructed position of the γ-ray emission. The Doppler-correction performed with MINOS is illustrated on the left-hand side of figure 5.17. The emission of two γ rays at two different positions and their detection in two different detectors are shown. It can be seen that the knowledge of the reaction vertex causes two things: A different emission angle ϑ, even if the same DALI2 detector is hit by the γ ray, and furthermore, different velocities β during the emission can be obtained for different positions inside the target. The picture on the right-hand side shows the Doppler-correction performed in case of a (p, p') reaction where MINOS cannot be used. Since the reaction vertex is unknown, it is assumed that the de-excitation occurs in the center of the target. Therefore, the velocity which is used for the Doppler-correction, corresponds to the ions' velocity in the center of the target. Furthermore, the emission angles ϑ depend only on the effective interaction points inside the DALI2 crystals. This causes a worse energy resolution for the (p, p') analysis.

In order to perform the Doppler-correction described before, the ions' velocities at the target position have to be obtained. As described in section 4.2.1, the distribution of ion velocities β_{57} is obtained in BigRIPS. These velocities correspond to the ion velocities directly after the degrader at F5 [87]. Since there is a certain amount of material between the degrader at F5 and the MINOS target causing energy loss, a LISE++ [107] calculation was performed. The LISE++ calculation uses the mean value of the distribution β_{57} as input and calculates the ion velocities at the target position. In addition, the velocities at the target position are calculated using the mean value of the velocity distribution β_{89} measured in ZeroDegree. The velocity β_{89} corresponds to the ion velocities before the first PPAC at F9. The mean value of both velocity interpolations determine the final ion velocity at the target position. A complete list of the material placed in this stage of BigRIPS and ZeroDegree is given in appendix A.4. The obtained ion velocities at the target position β_{before}, β_{middle}, and β_{after} are listed in table 5.4. The difference between the velocities at the target position extracted from β_{57} and β_{89} is $< 0.3\%$. With the obtained velocities β_{before}, β_{middle}, and β_{after} the Doppler-correction using MINOS is implemented by

$$\beta_{vertex} = \beta_{before} - \frac{z_{vertex}}{L_{target}} \left(\beta_{before} - \beta_{after} \right), \tag{5.10}$$

where z_{vertex} is the reconstructed vertex position ranging from 0 to the target length L_{target}. β_{before} is the beam velocity before the target and β_{after} is the beam velocity after the target. It is important to mention that β_{before} corresponds to the BigRIPS velocity distribution β_{57} shifted to the velocity before the target by the LISE++ calculation previously described. Similarly, β_{after} corresponds to the measured velocity distribution β_{89} in ZeroDegree shifted to the velocity after the target by LISE++. In the case that the MINOS reconstruction cannot be used the velocity β_{middle} is used for the Doppler-correction. Hereby, the velocity distribution β_{57} obtained in BigRIPS is shifted to the velocity in the middle of the target, which is determined by the LISE++ calculation.

Table 5.4.: Velocities of the nuclei of interest at the target position calculated with LISE++.

Reaction	β_{before}	β_{middle}	β_{after}
^{87}As $(p, 2p2n)$ ^{84}Ge	0.6399	0.6122	0.5747
^{86}As $(p, 2pn)$ ^{84}Ge	0.6409	0.6120	0.5753
^{85}Ge (p, pn) ^{84}Ge	0.6402	0.6127	0.5783
^{84}Ge (p, p') ^{84}Ge	0.6411	0.6135	0.5789
^{87}As $(p, 2p)$ ^{86}Ge	0.6362	0.6066	0.5687
^{86}Ge (p, p') ^{86}Ge	0.6354	0.6072	0.5717
^{89}As $(p, 2p)$ ^{88}Ge	0.6272	0.5961	0.5558
^{94}Kr (p, p') ^{94}Kr	0.6318[1]	0.5905[1]	0.5492[1]
^{96}Kr (p, p') ^{96}Kr	0.6250[1]	0.5821[1]	0.5391[1]

[1] Taken from [101]

Furthermore, the relative position of DALI2 and the MINOS target to each other is crucial for the Doppler-correction. Since this quantity could not be measured with sufficient precision at the setup, two offsets are introduced during the analysis to correct for the actual position. These offsets have been determined by Sidong Chen (RIKEN) for the SEASTAR campaign 2015. A DALI2 offset of 41.5 mm and a MINOS offset of 8 mm have been extracted.

As an illustration, a Doppler-corrected γ-ray spectrum for the reaction ^{85}Ge$(p, pn)^{84}$Ge using the MINOS device is shown in figure 5.18a. A Doppler-corrected γ-ray spec-

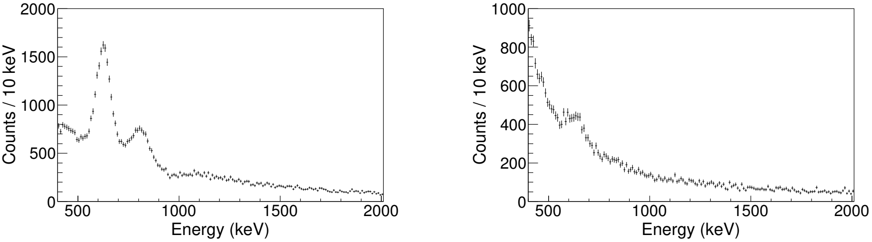

(a) ^{85}Ge$(p, pn)^{84}$Ge.

(b) ^{84}Ge$(p, p')^{84}$Ge.

Figure 5.18.: Doppler-corrected DALI2 spectrum for a knock-out and a (p, p') reaction.

trum for the reaction ^{84}Ge$(p,p')^{84}$Ge where the MINOS reconstruction cannot be used is depicted in figure 5.18b. Two things become evident. First, in the case of a (p,p') reaction the signal-to-background ratio is much smaller compared to the knock-out reaction. Second, the width of the observed peaks is larger in the case of a (p,p') reaction. This fact is notable for the transition at lowest energy in both spectra, i.e. the $2^+_1 \rightarrow 0^+_1$ transition.

5.5 Simulation of the lineshape

Since the geometry of DALI2 is complex, its detection-response function for γ radiation emitted in flight is simulated via GEANT4 [100]. The simulation, written by P. Doornenbal, which is used for the whole SEASTAR campaign, is divided into three steps: an `EventGenerator`, an `EventBuilder`, and a `Reconstructor`. A detailed manual is provided by [108].

`EventGenerator`

One million particles are simulated to impinge on the liquid hydrogen target of MINOS. The energy of the incoming particles is chosen such that it matches the velocities in front of the target which are listed in table 5.4, obtained by the LISE++ calculation. Additional beam characteristics, like the width and the position of the beam, are adjusted to match the measured beam quantities of BigRIPS. The MINOS target is implemented by a cylinder with the dimensions discussed in section 4.3.1 and a density of 73.22(8) kg/m^3. This information is used to simulate the slowing down of the irradiating ions inside the target. Furthermore, the half-life of the excited state and the energy of the simulated γ-ray is provided. Together with the velocity distribution, a half-life dependent emission of γ-radiation in random directions is simulated. The resulting information of the γ rays' Doppler-shifted energy and its emission direction, together with the positions where the nuclei are excited and de-excite, are forwarded to the next simulation step, the `EventBuilder`.

`EventBuilder`

The `EventBuilder` uses the output from the `EventGenerator` to simulate the interaction of the γ radiation with the DALI2 array. The geometry of DALI2, presented in section 4.4, is implemented into the simulation. In addition, an offset of 16.5 mm from the MINOS target to the nominal center of DALI2 and a position resolution of 5 mm (FWHM) [82] for MINOS were introduced adopting the experimental conditions. The interaction positions and the deposited energies at these positions are obtained for each γ ray by means of the simulation. It should be noted that due to (e.g.) the Compton-effect a γ ray can have more than one interaction point.

Therefore, the total γ-ray energy is not necessarily deposited at the first interaction point. In the final step, the individual detector resolution obtained for the corresponding setting (see section 5.3.1) is used to smear out the energies received by the simulation. The newly obtained simulation results and the information from the `EventBuilder` are forwarded to the `Reconstructor`.

`Reconstructor`

The `Reconstructor` uses the output of the `EventBuilder` as input. This simulation output matches the experimental observables from MINOS and DALI2. Therefore, the analysis of the `EventBuilder` output is performed in the same way as it is realized for the measured data. The most important operation step of the `Reconstructor` is the Doppler-correction, which has to be done precisely like the experimental analysis described in section 5.4. Therefore, the γ-ray emission angle ϑ has to be based on the same information obtained during the measurement. If the MINOS reconstruction is in use, the excitation position of the impinging nuclei serves to reconstruct ϑ and β while in case of a (p,p') reaction both values at the center of MINOS are used. Additionally, both cases use the effective first interaction points inside DALI2. The effective first interaction points are the ones used for the experimental analysis as described in section 5.4.
An example of the simulated lineshapes concerning three different energies is shown in figure 5.19. It can be seen that each simulated transition consists of a

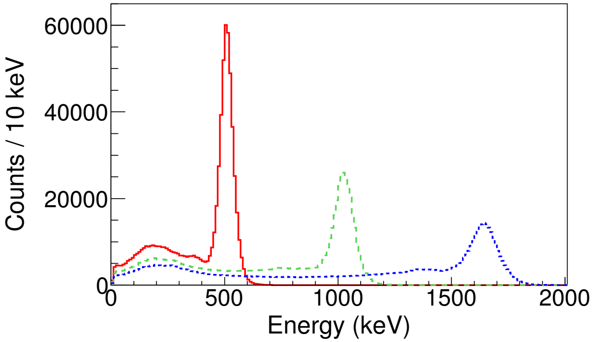

Figure 5.19.: Simulated lineshapes for three different transition energies. A transition energy of 507 (1030) [1650] keV was used to simulate the red, solid (green, dashed) [blue, dotted] lineshape. No transition half-life was set.

full-energy peak, in case the total γ-ray energy was deposited in the detector and a Compton-continuum, in case where only a part of the energy was deposited. In addition, the DALI2 energy-dependent efficiency is reflected by the decreasing area of the simulated lineshapes for increasing energies. These simulated lineshapes are used to describe the experimental spectra. The fitting procedure is described in the following section 5.6.

5.6 Fitting of the experimental spectra

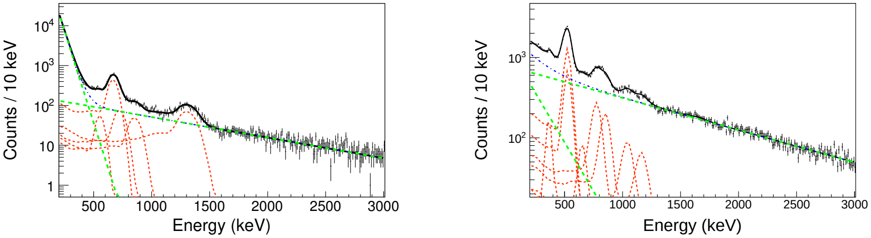

(a) ^{94}Kr$(p,p')^{94}$Kr.

(b) ^{87}As$(p,2p)^{86}$Ge.

Figure 5.20.: Doppler-corrected DALI2 spectrum for a knock-out and a (p,p') reaction. The fit of the double-exponential functions describing the background is illustrated in green.

This section outlines the applied fitting procedure describing the experimental spectra by the simulated lineshape. The simulated lineshape of each observed transition is fitted together with a double-exponential function describing the background to the experimental spectrum. Each lineshape has two fitting parameters: the transition energy and an amplitude scaling the height of the distribution. Section 5.4 discusses the distinct background in the treated reaction types. Therefore, different kind of fitting procedures are performed for the knock-out reactions and the (p,p') reactions. An example for both reaction types is depicted in figure 5.20. In case of a (p,p') reaction shown in figure 5.20a, the background at low energies is particularly high. This background is described by two exponential functions shown in green. One of them is fixed to high energies (2000-3000 keV in the shown case) and the other is fixed to low energies (200-300 keV). The remaining part of the spectrum is described by the simulated lineshapes, which are adjusted in amplitude and energy. For the knock-out reactions the background at low energies is much lower, as shown in figure 5.20b. By a fit of one exponential function to high energies of the spectrum, most of the background is already considered. It can be seen that the region from 200 to 400 keV is dominated by Compton scattered events from the observed transitions. However, not all the observed γ rays at low energies stem from Compton scattered events of observed transitions. This background at low energies is taken into account by a second exponential function whose parameters are free during the fit. It is important to note that the second exponential function cannot be fixed to the low-energy part of the spectrum, as in the case of a (p,p') reaction since there is a crucial amount of γ rays stemming from Compton scattered events which cannot be neglected. The specifics of each fitted spectrum by the simulated lineshapes and the double-exponential function are discussed in section 6.

5.7 Characteristics of $\gamma\gamma$-coincidences with DALI2

To identify cascades of γ-ray transitions, $\gamma\gamma$-coincidences are used. Therefore, multiple γ rays which are detected at the same time by DALI2 are sorted into a 2D-matrix in such a way that each permutation of simultaneously detected energies has one entry. Figure 5.21 shows such a 2D matrix for ^{84}Ge. For the matrix depicted, it is requested that not more than 6 γ rays are detected at the same time. Points with higher statistics in this matrix indicate that γ rays with the corresponding energies on x- and y-axis are measured at the same time. By projecting the energy range 570-670 keV on the y-axis, the spectrum in figure 5.22a is obtained (Note that a smaller y-energy range than in the matrix is chosen). The black data points in the energy region 570-670 keV indicate a coincidence to this region. In the following the origin of this coincidences is explained. The number of coincident

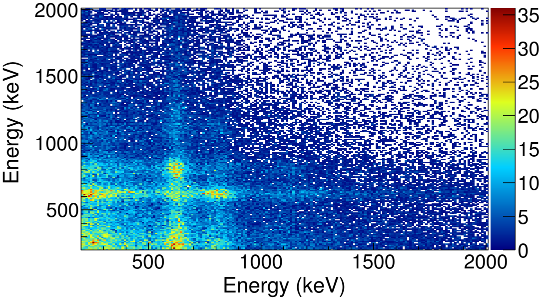

Figure 5.21.: 2D $\gamma\gamma$-coincidence matrix for ^{84}Ge. Multiplicity ≤ 6 is shown.

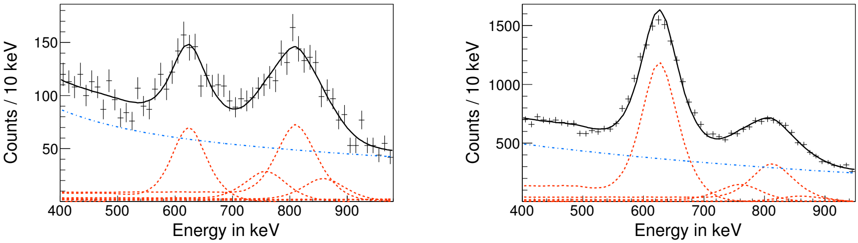

(a) Energy projection of the x-range 570-670 keV in figure 5.21 on the y-axis. Multiplicity ≤ 6 is shown.

(b) Doppler-corrected DALI2 spectrum with multiplicity ≤ 6

Figure 5.22.: Doppler-corrected DALI2 spectrum and gate on a $\gamma\gamma$-coincidence spectrum for the reaction ^{85}Ge$(p,pn)^{84}$Ge.

γ rays is determined by a fit of the red, dashed simulated lineshape to 1063(32) counts. Figure 5.22b shows a DALI2 spectrum where the number of γ rays observed by DALI2 is limited to 6 in agreement with the restriction for the $\gamma\gamma$-coincidences matrix. The experimental spectrum is again fitted by simulated lineshapes (Parts of the fits for the higher-energy transitions cannot be seen in this figure. If the reader is interested in the fit, the author refers to figure 6.1a showing the fit of the whole spectrum). The Compton continua of the transitions at higher energies underneath the gated energy range of 570-670 keV are visible. Summing up these γ rays yield 1020(32) counts. This means that the observed coincidence is a characteristic of the DALI2 array which can be explained by the particular lineshape of the observed transitions and a gate on Compton events from high-lying transitions.

5.8 Half-life dependent uncertainty

As described in section 5.4, the reconstructed reaction position is used for the Doppler-correction. However, the de-excitation of the excited nucleus occurs further downstream depending on its half-life. This causes a different velocity and emission angle for the emitted γ radiation, compared to those used for the Doppler-correction. Therefore, the observed transition energy is shifted and the peak shape is broadened. By the broadening of the lineshape, it is possible to deduce the half-life of the de-excited state. The following examines how the half-lifes of the de-excited states were determined and how an uncertainty is derived from it.

In a first step, the experimental spectrum is fitted by the simulated DALI2 response for each observed transition, together with a double exponential function describing the background, as explained in section 5.6. The the position and its amplitude are the fitting parameters for a simulated lineshape. Regarding the first fit no half-life is considered for all simulated lineshapes. In a second step, all parameters from the exponential function, as well as the position and the amplitude of the simulated lineshapes, are fixed to the values obtained by the first fit, except for one transition. For this transition the two parameters are free and a fit is performed with simulated lineshapes for different level half-lifes. Each fit gives a χ^2 which is a measure for the quality of the fit. Figure 5.23 depicts the behavior of the χ^2 for different half-lifes by the red diamonds for the transition at 510 keV corresponding to the $(2_2^+) \rightarrow (2_1^+)$ decay in ^{86}Ge. A clear minimum for a certain $T_{1/2}$ is observed from a fit of a second order polynomial function. Since, this half-life describes the data the best it is used for the analysis. The uncertainty of this χ^2 analysis is given by the 1σ level which corresponds to a change of $\chi^2 = 1$ from the minimum, thus the half-life is defined. This range of $T_{1/2}$ is used to calculate the corresponding energy shift, and therefore, to define the half-life dependent uncertainty of the obtained transition energies. The χ^2 fits of the other transitions treated in this work are given in appendix A.5. In some cases the best χ^2 was obtained for $T_{1/2} = 0$. In these cases an upper limit was found by the method described before.

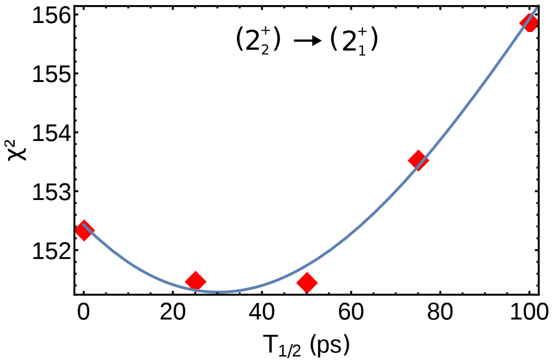

Figure 5.23.: Evolution of χ^2 for different level half-lifes $T_{1/2}$ used for the simulation of a de-exciation transition energy of 510 keV corresponding to the $(2_2^+) \rightarrow (2_1^+)$ decay in ^{86}Ge. The data points are fitted by a second order polynomial function.

5.9 Treatment of the reaction channels

Within this work, ^{84,86,88}Ge and ^{94,96}Kr populated by different reactions are analyzed. Figure 5.24a shows the ZeroDegree particle identification (PID) plot for setting 1. It displays all the nuclei registered in ZeroDegree. Serving as example, ^{84}Ge and ^{86}Ge are selected by a condition on A/Q and Z, as indicated by the red cycles. These conditions can be used to identify the corresponding nuclei in BigRIPS. The PID plot for BigRIPS, requiring ^{84}Ge in ZeroDegree, is depicted in figure 5.24b. It becomes evident that ^{84}Ge in ZeroDegree is populated by four reactions: ^{87}As$(p,2p2n)$, ^{86}As$(p,2pn)$, ^{85}Ge(p,pn) and ^{84}Ge(p,p').

The BigRIPS PID, requiring ^{86}Ge in ZeroDegree, is presented in figure 5.24c. Two isotopes in BigRIPS fulfill this condition. Therefore, the reaction channels are: ^{87}As$(p,2p)$ and ^{86}Ge(p,p').

A condition demanding ^{88}Ge in ZeroDegree is leading to the BigRIPS PID depicted in figure 5.24d. Thus, the reactions populating ^{88}Ge are ^{90}Se$(p,3p)$, ^{88}As$(p,2p)$ and ^{88}Ge(p,p'). It is important to notice that the reaction channels ^{90}Se$(p,3p)^{88}$Ge and ^{88}Ge$(p,p')^{88}$Ge have very low cross sections. Because of this reason, they are not considered for the further analysis.

Finally, figures 5.24e and 5.24f depict the reactions populating ^{94}Kr and ^{96}Kr. Only the (p,p') reaction channels are analyzed within this work while the other reactions are analyzed by Kevin Moschner (University of Cologne).

Since the analysis of knock-out reactions and (p,p') reactions face different difficulties and require various analysis steps they are discussed in different sections. The implemented analysis steps, concerning the knock-out reactions are presented in section 5.9.1, while the (p,p') reaction analysis is discussed in section 5.9.2.

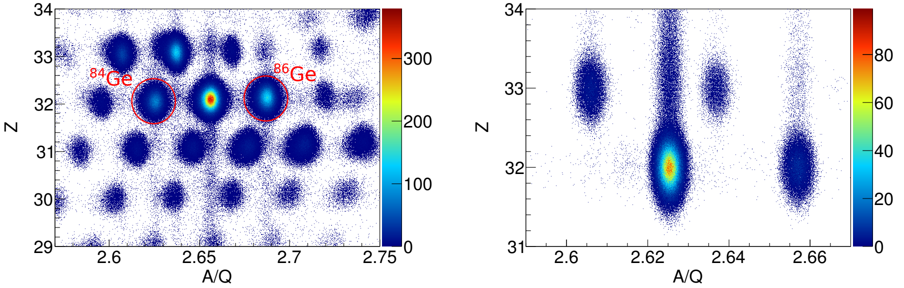

(a) ZeroDegree PID of setting 1. ^{84}Ge and ^{86}Ge are highlighted.

(b) BigRIPS PID gated on ^{84}Ge in ZeroDegree.

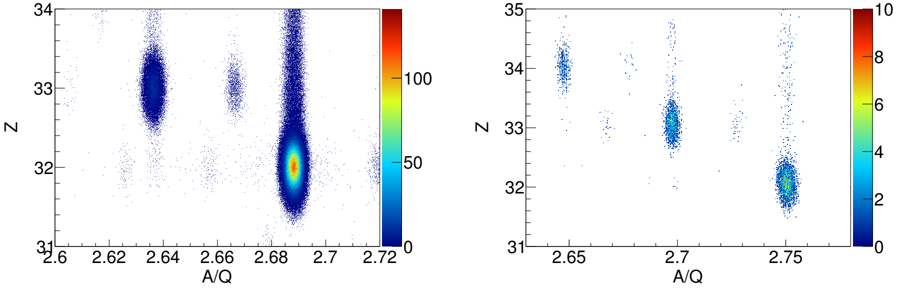

(c) BigRIPS PID gated on ^{86}Ge in ZeroDegree.

(d) BigRIPS PID gated on ^{88}Ge in ZeroDegree.

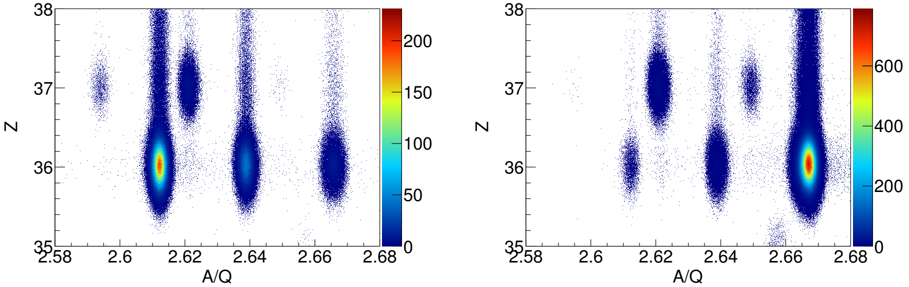

(e) BigRIPS PID gated on ^{94}Kr in ZeroDegree.

(f) BigRIPS PID gated on ^{96}Kr in ZeroDegree.

Figure 5.24.: PIDs in ZeroDegree and BigRIPS. Gates on certain nuclei in ZeroDegree are used for the BigRIPS PIDs shown.

5.9.1 Knock-out reactions

This section discusses the particular analysis of the knock-out reactions. The PIDs shown in figure 5.24 can be used to select distinct reaction channels, and therefore, to extract the reaction cross section, as described in the first paragraph of this section. Knowing the reaction channels, it is of interest to consider the emitted γ radiation caused by these reactions and detect them with DALI2. Using the detected γ radiation the cross section calculation for a particular state can be obtained, as described afterwards. Finally, a method to judge on the significance of γ-ray transitions observed by DALI2 is presented.

Reaction cross sections

The reaction cross section is an area quantifying the probability that an impinging ion is interacting with the target material. Considering N_{inc} incident ions impinging on a target with a number of scattering centers per area n, the amount of outgoing particles N_{out} is given by

$$N_{out} = \sigma_{reaction} \cdot n \cdot N_{inc}, \tag{5.11}$$

with the cross section $\sigma_{reaction}$ describing the probability that the reaction occurs. For the SEASTAR campaign the number of scattering centers n is characterized by

$$n = \rho_{LH_2} \cdot L_{LH_2} \cdot \frac{N_A}{M_H}, \tag{5.12}$$

where ρ_{LH_2} and L_{LH_2} are the density and the length of the MINOS target. N_A is the Avogadro constant, M_H is the molar mass of hydrogen, resulting in $n = 4.329(44) \cdot 10^{23}$. To perform a measurement of the reaction cross section, the reaction partners are selected in BigRIPS and ZeroDegree. But not all ions produced at the beginning of the BigRIPS fragment separator reach the ZeroDegree spectrometer, which is caused by scattering of material along the beam line and the efficiencies of the used detectors. Therefore, the reaction cross section needs to consider the transmission T, compensating that not all the ions are detected in the ZeroDegree spectrometer. The reaction cross section including the transmission T is given by

$$\sigma_{reaction} = \frac{N'_{out}}{N_{inc}} \cdot \frac{1}{nT}, \tag{5.13}$$

with $N'_{out} = T \cdot N_{out}$ being the amount of particles detected in ZeroDegree considering the losses due to the transmission, which is composed of three efficiencies:

$$T = \epsilon_{beam\ line} \cdot \epsilon_{target} \cdot \epsilon_{ZeroDegree}. \tag{5.14}$$

$\epsilon_{beam\ line}$ is considering the losses along the beam line, while ϵ_{target} takes into account the particle losses due to scattering in the hydrogen reaction target of MINOS. Finally, $\epsilon_{ZeroDegree}$ describes the undetected particles based on the acceptance of the ZeroDegree spectrometer. The following describes the method used to obtain these efficiencies.

$\epsilon_{beam\ line}$:

Before every setting, an empty MINOS target measurement was performed. During this measurement a nucleus centered in BigRIPS and ZeroDegree is selected. The centered nuclei during this measurement were ^{85}Ga for setting 1, ^{90}Se for setting 2, and ^{95}Br for setting 3. The beam line efficiency $\epsilon_{beam\ line}$ is calculated by

$$\epsilon_{beam\ line} = \frac{N_{ZeroDegree}}{N_{BigRIPS}}, \tag{5.15}$$

where $N_{BigRIPS}$ is the number of ions detected in BigRIPS and $N_{ZeroDegree}$ the number of ions detected in ZeroDegree. This efficiency is independent on the considered reaction channel and it is assumed to be constant for the considered setting. The obtained efficiencies $\epsilon_{beam\ line}$ for the three settings are listed in table 5.5.

Table 5.5.: Efficiency $\epsilon_{beam\ line}$ obtained for the three settings.

	Setting 1	**Setting** 2	**Setting** 3
$\epsilon_{beam\ line}$	0.905(32)	0.871(3)	0.924(2)

ϵ_{target}:

Typically, the product of $\epsilon_{beam\ line}$ and ϵ_{target} is obtained by a setting with the same nuclei centered in BigRIPS and ZeroDegree together with the filled MINOS target. Such measurements were only performed before setting 2 and 3. In these cases,

$$\epsilon_{beam\ line} \cdot \epsilon_{target} = \frac{N_{ZeroDegree}}{N_{BigRIPS}}. \tag{5.16}$$

Note that $N_{ZeroDegree}$ will be smaller than for the measurement with the empty MINOS target. Concerning setting 1, the product $\epsilon_{beam\ line} \times \epsilon_{target}$ was extracted from the experimental runs, since a setting with filled MINOS target and the same nucleus centered in BigRIPS and ZeroDegree was not performed. Therefore, the ratio $N_{ZeroDegree}/N_{BigRIPS}$ cannot be applied since different ions are centered in BigRIPS and ZeroDegree. To solve this issue, the x-position distribution at F5 is considered, as shown in figure 5.25. The blue histogram depicts the position distribution for all ^{86}Ge ions observed in BigRIPS while the black histogram shows the ^{86}Ge ions detected in BigRIPS and ZeroDegree. The blue histogram is scaled by a factor of 0.612(2) to the black one. This factor is obtained by a fit of the function shown in red. It becomes evident that both histograms have the same shape from 10 to 90 mm, but differ significantly for x-positions smaller than 10 mm. This due to the acceptance of the ZeroDegree spectrometer cutting out the part of the distribution with x-positions smaller than 10 mm. Since the acceptance of ZeroDegree does not effect the shape of the x-positions distributions from 10 to 90 mm, the obtained scaling factor from the fit reflects the ion losses due to the beam line and the scattering inside the target, and therefore, the product $\epsilon_{beam\ line} \times \epsilon_{target}$ from equation 5.16. This method was conducted for ^{87}As and ^{84}Ge as well, where scaling factors of 0.611(3) and 0.618(3) were gained. For the further analysis, the average 0.614(2) of the three values is used. The product of $\epsilon_{beam\ line} \times \epsilon_{target}$ stays constant for each setting and the derived values are presented in table 5.6.

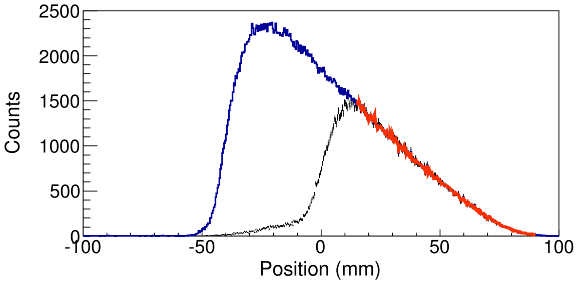

Figure 5.25.: x distributions at F5 for ions detected in BigRIPS shown by the blue histogram and ions detected in BigRIPS and ZeroDegree shown by the black data points. A function describing the course of the blue histogram is shown in red. This function determines a scaling factor which is applied to scale down the blue histogram, so that both histograms overlay in the region from 10 to 90 mm.

Table 5.6.: Product of the efficiencies $\epsilon_{beam\ line}$ and ϵ_{target} obtained for the three settings.

	Setting 1	**Setting** 2	**Setting** 3
$\epsilon_{beam\ line} \cdot \epsilon_{target}$	0.614(2)	0.573(2)	0.581(2)

$\epsilon_{ZeroDegree}$:

The efficiency $\epsilon_{ZeroDegree}$ is reflecting the undetected reaction products in ZeroDegree because of its limited acceptance. In order to extract this efficiency, the x-position distributions at F5 from ions detected in BigRIPS and ions registered in BigRIPS and ZeroDegree need to be compared for the considered reaction channel. Figure 5.26 shows the distribution of the ions detected in BigRIPS in blue and the distribution of the ions observed in both, BigRIPS and ZeroDegree, in black. The evolution of both shapes agree in the region from -20 mm to 20 mm, thus this region can be assumed to be independent of the ZeroDegree acceptance and $\epsilon_{ZeroDegree} = 1$ in this region. Because of this, a function is fitted to the position distribution of the ions detected in BigRIPS and ZeroDegree. It describes the position distribution of the ions detected in BigRIPS for the mentioned region. The resulting fit is shown in red and the obtained scaling factor is used to scale the distribution

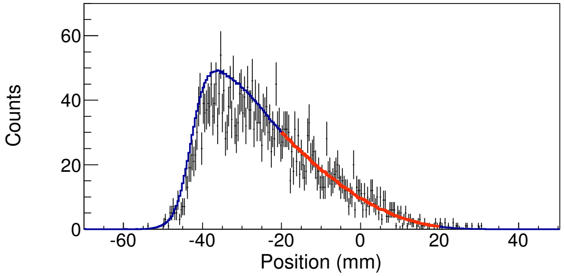

Figure 5.26.: x distributions at F5 for ions detected in BigRIPS shown by the blue histogram and ions detected in BigRIPS and ZeroDegree shown by the black data points. A function describing the course of the blue histogram is shown in red. This function is fitted to the black data points to obtain a scaling factor, which is used to align both distribution in region from -20 to 20 mm. See text for more details.

of the ions observed in BigRIPS to the distribution of the nuclei registered in both. Knowing the scaling factor a_{scale}, the efficiency $\epsilon_{ZeroDegree}$ can be obtained by

$$\epsilon_{ZeroDegree} = \frac{N_{ZeroDegree}}{N_{BigRIPS} \cdot a_{scale}}. \tag{5.17}$$

The resulting efficiencies $\epsilon_{ZeroDegree}$ for the considered reaction channels are given in table 5.7, just like the obtained transmission from BigRIPS to ZeroDegree.

Table 5.7.: Product of the efficiencies $\epsilon_{beam\ line}$ and ϵ_{target} obtained for the three settings.

Reaction	$\epsilon_{ZeroDegree}$	**T**
^{87}As $(p,2p2n)$ ^{84}Ge	0.089(6)	0.055(4)
^{86}As $(p,2pn)$ ^{84}Ge	0.602(25)	0.370(16)
^{85}Ge (p,pn) ^{84}Ge	0.240(7)	0.148(4)
^{87}As $(p,2p)$ ^{86}Ge	0.895(30)	0.550(18)
^{89}As $(p,2p)$ ^{88}Ge	0.576(27)	0.329(17)

Excitation cross sections of particular states

In order to calculate the cross section for the excitation of a particular state, one has to measure how often a state has been populated and how many ions undergo an interaction with the target. The amount of ions impinging on the target can be counted in BigRIPS. Since the reaction channel has to be selected, the transmission T to ZeroDegree has to be considered. Besides this, not every ion emitting a γ ray is observed by MINOS. Therefore, the efficiency of MINOS ϵ_{MINOS} has to be incorporated. It is defined by the ratio of reconstructed vertices and the total amount of reactions occurring. Because of problems concerning the DALI2 trigger during the SEASTAR 2015 campaign, an additional correction factor has to be considered. In some cases the DALI2 trigger was not sent to the DAQ, although γ rays were detected by DALI2. Every event is stored in the data together with its induced triggers. Thus, the DALI2 events which did not send a trigger to the DAQ are labeled by the coincidence register model with $fbit == 3$. DALI2 events which sent a trigger to the DAQ are labeled by $fbit == 7$ or $fbit == 6$. Since $fbit == 3$ is combined with the F7(DS) trigger it can only be compared to $fbit == 7$ which contains the F7(DS) trigger as well (compare table 4.1). The amount of missing events can be obtained, by introducing a DALI2 trigger efficiency $\epsilon_{DALI2,trigger}$:

$$\epsilon_{DALI2,trigger} = \frac{N_{fbit==3}}{N_{fbit==3||fbit==7}}. \tag{5.18}$$

$N_{fbit==3}$ and $N_{fbit==3||fbit==7}$ denote DALI2 events with the triggers as indicated by the indices (compare table 4.1). The obtained efficiencies ϵ_{MINOS} and $\epsilon_{DALI2,trigger}$ for each reaction channel are listed in table 5.8.

Table 5.8.: Efficiencies ϵ_{MINOS} and $\epsilon_{DALI2,trigger}$ for each reaction channel.

Reaction	ϵ_{MINOS}	$\epsilon_{DALI2,trigger}$
^{87}As $(p,2p2n)$ ^{84}Ge	0.764(11)	0.496(39)
^{86}As $(p,2pn)$ ^{84}Ge	0.880(7)	0.522(24)
^{85}Ge (p,pn) ^{84}Ge	0.543(5)	0.520(20)
^{87}As $(p,2p)$ ^{86}Ge	0.898(5)	0.546(18)
^{89}As $(p,2p)$ ^{88}Ge	0.891(31)	0.482(81)

Using the transmission given in table 5.7, the MINOS efficiency ϵ_{MINOS} and the DALI2 trigger efficiency $\epsilon_{DALI2,trigger}$, the cross section for the excitation of a particular state is described by

$$\sigma_{state} = \frac{A \cdot N_{simulated}}{N_{BigRIPS}} \cdot \frac{1}{\epsilon_{DALI2,trigger} \cdot \epsilon_{MINOS}} \cdot \frac{1}{nT}, \tag{5.19}$$

with the number of simulated ions $N_{simulated}$, the amplitude A obtained from the fit of the simulation to the data, discussed in section 5.6, and n the number of scattering centers per area. It is important to note that by fitting the simulated lineshape to the energy spectrum the efficiency of the DALI2 array is already considered.

Significance test

As described in section 5.6, the experimental DALI2 spectra are fitted using two exponential functions describing the background and by simulated lineshapes of the transitions observed. These simulated lineshapes consist of a photopeak and the Compton-continuum since these two effects are the underlying physical mechanisms causing the specific shape. Therefore, it can be assumed that the distributions of simulated lineshapes for different energies are equal. By fitting the simulated lineshapes to the experimental spectrum of DALI2, different measurements of the same quantity are performed, namely a measurement of the covered area of a transition lineshape. The uncertainty of this measurement is obtained by the uncertainty of the fit. In [109], it is described that the revised measurement of the same quantity and its uncertainty are governed by a functional interrelation. The measured lineshape areas versus their corresponding uncertainties are shown in figure 5.27. The lineshape areas together with their uncertainties are obtained from fits of the experimental DALI2 spectra of setting 1. Two different data points are shown in figure 5.27. The purple data points correspond to measured transition areas from a standard DALI2 spectrum, while the green data points represent measured lineshape areas from a coincidence spectrum of a certain transition. Regarding the distribution of the points, no systematics can be observed between both cases. A second order polynomial function (blue) is used to describe the data points. It is important to notice that the functional interrelation is not determined. Thus, the choice of a second order polynomial function is conservative compared to a linear fit function. On the basis of the shown fit function, the interrelation between the measured areas and their corresponding uncertainties can be interpolated to an area of 0. Thus, the measurement of an area with zero counts has an uncertainty of 64(8) Counts. That means it is not possible to distinguish a minimum of 72 counts from background within the presented measurements since 72 counts are inside the 1σ interval of a DALI2 response with zero counts. Areas above this limit can be considered as significant and the significance can be given in units of σ.

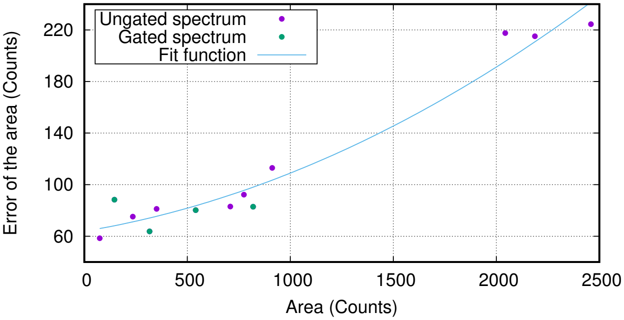

Figure 5.27.: Measured peak area versus its uncertainty. The correlation is fitted by a second order polynomial function.

5.9.2 (p,p') reactions

Figure 5.18b indicates that the optimization of the measured energy spectra, especially the reduction of the background, is essential for the analysis of the (p,p') reaction channels. The first paragraph of this section describes the reduction of the background. Afterwards, it is described how the cross section for the excitation of a particular state is calculated.

Background reduction

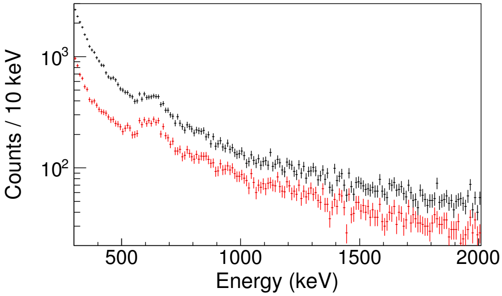

Figure 5.28.: Comparison of a DALI2 energy spectrum from all detectors (black) and a DALI2 energy spectrum using only detectors with ID 53-186 (red).

The obtained energy spectra of DALI2 after a (p,p') reaction suffer from high background. A spectrum of the reaction ^{84}Ge$(p,p')^{84}$Ge is depicted by the black data points in figure 5.28. The two characteristics of the spectrum are on one hand the significant background and on the other hand a bad energy resolution. In order to improve the energy resolution, detectors around $\vartheta \approx 90^\circ$ (ID 0-53) are not considered since those are affected by Doppler-broadening the most. In addition, figure 5.14 shows that the resolution of these detectors belongs to the poorest of the setup. The resulting spectrum is presented by the red data points in figure 5.28. Compared to the black DALI2 spectrum without any conditions, the peak around 600 keV becomes more pronounced in the DALI2 spectrum using the constraints for the detectors. For further background reduction it is necessary to consider the detected γ-ray energy versus the time when the γ ray was detected. This relation is shown in figure 5.29. It can be seen that the first γ rays reach DALI2 at the time ~ -5 ns, while the largest proportion of γ radiation hits DALI2 at the time ~ 0 ns.

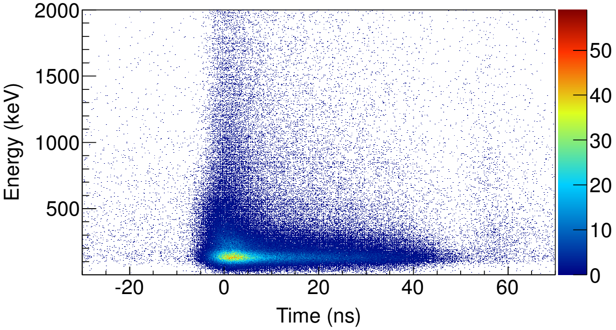

Figure 5.29.: Detected DALI2 energy versus DALI2 time.

For longer times (> 10 ns), especially for small energies, a long tail arises which contributes significantly to the background. During a period of 10 ns a particle moving with ∼ 0.5 c would travel a distance of ∼ 1.5 m. Even if the beam pulse has a certain spatial distribution, it can be excluded that detected γ radiation stem from de-excitations of excited beamlike ions after 10 ns. The resulting spectrum, introducing a time cut of ±10 ns together with an ID-53-186 condition compared to the DALI2 spectrum using only the detector ID cut, is shown in figure 5.30a.

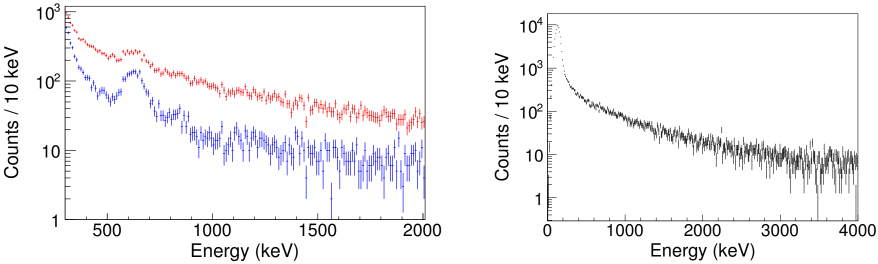

(a) Comparison of a DALI2 spectrum using detectors with ID-53-186 only (red) and a DALI2 spectrum with a DALI2-time condition of ±10 ns and the same ID cut applied (blue).

(b) Difference of both spectra shown in 5.30a.

Figure 5.30.: Doppler-corrected DALI2 spectrum with different conditions for the reaction ^{84}Ge$(p, p')^{84}$Ge and their difference.

This condition allows to receive a much clearer energy spectrum. Nevertheless, it is necessary to ensure that no γ rays from de-exciting beamlike ions are discarded. This is illustrated by figure 5.30b showing the difference of the energy spectrum with applied ID condition and the energy spectrum using the ID and the time condition. In this spectrum no transitions are visible. The same check was performed for the other (p, p') reactions considered.

The resulting spectra showing the removed part of the energy spectrum are presented in appendix A.6.

Excitation cross section of a particular state

The cross sections for the excitation of a particular state after a (p, p') reaction are calculated similar to those of the knock-out reactions described by equation 5.19. Only the applied efficiencies have to be adjusted. Since the MINOS tracking is not used in case of a (p, p') reaction, the efficiency ϵ_{MINOS} should not be considered. Furthermore, the transmission $T_{(p,p')}$ is independent of the ZeroDegree acceptance for a particular reaction $\epsilon_{ZeroDegree}$. The transmission $T_{(p,p')}$ is therefore defined as

$$T_{(p,p')} = \epsilon_{beam\ line} \cdot \epsilon_{target}, \tag{5.20}$$

and is listed in table 5.6. The cross section for the excitation of a particular state after a (p, p') reaction calculates to

$$\sigma_{state,(p,p')} = \frac{A \cdot N_{simulated}}{N_{BigRIPS}} \cdot \frac{1}{\epsilon_{DALI2,trigger}} \cdot \frac{1}{nT_{(p,p')}}, \tag{5.21}$$

with the number of simulated ions $N_{simulated}$ and the amplitude A obtained from the fit of the simulation to the data, as described in section 5.6.

6 Results

6.1 Reaction cross sections

This section presents the resulting reaction cross sections of the knock-out channels populating ^{84,86,88}Ge obtained using the method described in section 5.9.1. The reaction cross section is calculated by equation 5.13. For each reaction, different transmissions T are obtained and listed in table 5.7. The number of incoming ions N_{inc} corresponds to the ions detected in BigRIPS, which requires the condition $fbit == 1$ && $fbit == 3$ && $fbit == 7$ (compare table 4.1). The number of outgoing particles N'_{out} request the same condition, whereas the ions have to be detected in BigRIPS and ZeroDegree. These conditions yields the reaction cross sections given in table 6.1. It becomes evident that reactions removing neutrons are more likely. Comparing the two reaction paths ^{87}As $(p,2p2n)$ and ^{87}As $(p,2p)$, the cross section increases by more than a factor of two, if two additional neutrons are removed. This fact illustrates the abundance of neutrons for the neutron rich, exotic nuclei considered in this work. The difference of the removal of one or two additional neutrons is not significant within the uncertainties, as indicated by the cross sections for the reactions ^{87}As $(p,2p2n)$ ^{84}Ge and ^{86}As $(p,2pn)$ ^{84}Ge. The proton knock-out seems to be the limiting factor in both cases. It is confirmed by the increasing cross section of the ^{85}Ge (p,pn) ^{84}Ge reaction where no additional proton is removed. Protons have to additionally overcome the Coulomb-wall compared to the neutrons.

Table 6.1.: Cross section $\sigma_{reaction}$ for the reactions populating ^{84,86,88}Ge.

Reaction	$\sigma_{reaction}$ (mb)
^{87}As $(p,2p2n)$ ^{84}Ge	11.02(81)
^{86}As $(p,2pn)$ ^{84}Ge	10.21(49)
^{85}Ge (p,pn) ^{84}Ge	47.11(160)
^{87}As $(p,2p)$ ^{86}Ge	4.24(17)
^{89}As $(p,2p)$ ^{88}Ge	6.07(58)

Section 6.2.3 discusses the cross section of a particular state σ_{state} after these reactions. The reaction cross sections obtained in this section, listed in table 6.1, will give an upper limit for the sum of the cross sections of i excited states $\Sigma_i \sigma_{state,i}$.

6.2 Knock-out reactions

The spectroscopic results from the analysis of the knock-out reactions are presented in this section. New transitions of ^{84,86,88}Ge are observed and the results are shown in section 6.2.1. Afterwards, the new observations are used to extend the known systematics of the Germanium isotopes. Their systematic behavior is compared to trends of neighboring even-even isotopic chains in section 6.2.2. The excitation cross section for particular states are presented in section 6.2.3.

6.2.1 New transition energies

^{84}Ge

^{84}Ge is populated by the three different reactions as illustrated in figure 5.24b. Beside the (p,p') reaction, the majority of ^{84}Ge in ZeroDegree is produced by the ^{85}Ge (p,pn) reaction channel. Therefore, the cross section for this reaction is the highest, as shown in table 6.1.

Since most of the transitions of ^{84}Ge are already known from β-delayed spectroscopy [110, 111, 112], ^{84}Ge serves as test case for the analysis of transition energies. As discussed before, ^{85}Ge (p,pn) ^{84}Ge is the strongest reaction channel. Therefore, the transition energies are obtained by the measured DALI2 spectrum of this reaction channel. Afterwards, the results from the ^{85}Ge (p,pn) ^{84}Ge reaction channel are cross checked with the spectra after the ^{87}As $(p,2p2n)$ ^{84}Ge and ^{86}As $(p,2pn)$ ^{84}Ge reactions.

Figure 6.1a shows the Doppler-corrected DALI2 spectrum with multiplicity ≤ 6 after the reaction ^{85}Ge (p,pn) ^{84}Ge, while a $\gamma\gamma$-coincidence spectrum gating on the energy region of the strongest transition is shown in figure 6.1b. Spectra with different multiplicity conditions are shown in appendix B.1.1. For the Doppler-correction MINOS is used as explained in section 5.4. The spectrum is fitted by simulated DALI2 response functions of the observed transitions together with a double-exponential function to consider the background as described in section 5.6. The energy ratio of the transition energies forming the triplet at 800 keV was taken from [110, 111, 112] to reduce the fitting parameters. Six transitions are

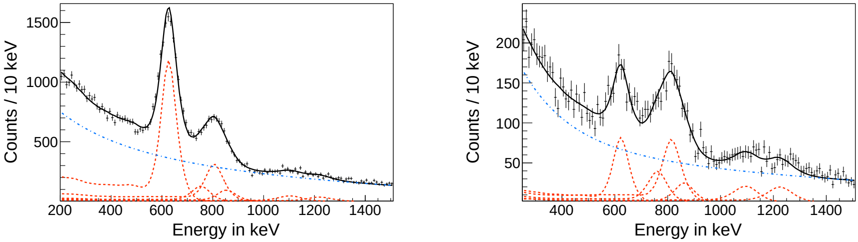

(a) Doppler-corrected DALI2 spectrum.

(b) $\gamma\gamma$-coincidence spectrum gated on the region of the 2^+_1.

Figure 6.1.: Doppler-corrected DALI2 spectrum and $\gamma\gamma$-coincidence spectrum gated on the region of the $2^+_1 \rightarrow 0^+_1$ transition after the reaction ^{85}Ge$(p,pn)^{84}$Ge. The shown spectra require multiplicity ≤ 6.

observed in the spectrum, listed in table 6.2, such as the literature values and the used level half-lifes $T_{1/2}$ with uncertainties obtained as described in section 5.8. The uncertainties of the transition energies consist of three contributions: an uncertainty from the DALI2 calibration obtained in section 5.3, an uncertainty that depends on the half-life of the state, as explained in section 5.8, and a statistical uncertainty stemming from the fitting procedure, discussed in section 5.6. In some cases the uncertainties are asymmetric caused by the half-life dependent uncertainties. Table 6.2 shows, that the obtained results within their uncertainties are in

Table 6.2.: Obtained transition energies after the reaction ^{85}Ge (p,pn) ^{84}Ge, together with the literature values from [110, 111, 112] and the half-lifes used for the simulation. The corresponding cross sections are given in table 6.5.

Transition energy (keV)	Literature value (keV)	$T_{1/2}$ (ps)
629 ± 7	623.9[1]	15 ± 10
762^{+10}_{-13}	764.3[1]	70^{+30}_{-40}
803 ± 8	805.4[1]	0^{+10}_{-0}
856 ± 10	858.0[1]	15^{+25}_{-15}
1121 ± 21	–	40^{+60}_{-40}
1229^{+16}_{-13}	1224.0[1]	25^{+40}_{-25}

[1] Taken from [110, 111, 112]

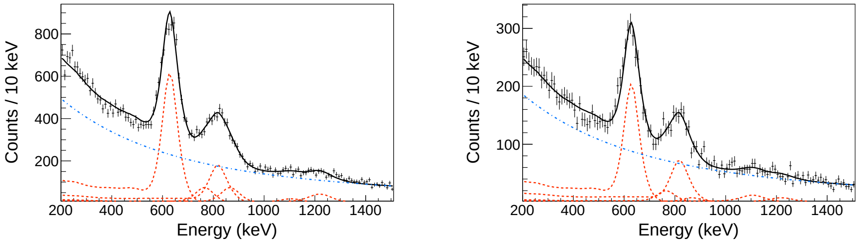

(a) After the reaction ^{86}As $(p, 2pn)$ ^{84}Ge. **(b)** After the reaction ^{87}As $(p, 2p2n)$ ^{84}Ge.

Figure 6.2.: Doppler-corrected DALI2 spectra requiring multiplicity ≤ 6.

good agreement with the known values from [110, 111, 112]. In addition a new transition is observed at 1128(24) keV.

Figures 6.2 show the DALI2 spectra after the reactions ^{87}As $(p, 2p2n)$ ^{84}Ge and ^{86}As $(p, 2pn)$ ^{84}Ge. Additional spectra of the two reaction channels for different multiplicities are shown in appendix B.1.2 and B.1.3. The fit of the spectra is performed using the transition energies listed in table 6.2. Both spectra are well described with the transition energies obtained from the ^{85}Ge (p, pn) ^{84}Ge reaction channel. These fits are performed to proof the consistency of the gained result and to verify if the $(p, 2pn)$ and $(p, 2p2n)$ reactions cause excitations of different states. After these reactions no additional transition can be identified in the Doppler-corrected DALI2 spectra, but the validity of the analysis for the DALI2 spectrum after the ^{85}Ge (p, pn) ^{84}Ge reaction is confirmed.

The present experiment is not sensitive to the spins of the involved states. Therefore, the level scheme, presented in figure 6.3, is based on systematics of neighboring Germanium isotopes and assumptions from knock-out reactions in general. From [113, 114, 115, 116] it can be seen that the strongest transition after a knock-out reaction corresponds to the $2^+_1 \rightarrow 0^+_1$ transition while the second strongest transition corresponds to the $4^+_1 \rightarrow 2^+_1$ transition. Therefore, the 629-keV and the 803-keV γ rays are assigned to be the $(2^+_1) \rightarrow (0^+_1)$ and the $(4^+_1) \rightarrow (2^+_1)$ transitions. By comparison to the mirror nucleus ^{80}Ge with respect to the shell closure at $N = 50$, the 762-keV γ rays is assigned to the $(2^+_2) \rightarrow (2^+_1)$ transition. The newly observed transition at 1121-keV is assigned to the $(6^+_1) \rightarrow (4^+_1)$ decay by the same reason. These assignments are in good agreement with the observations from [110, 111, 112]. For the 856-keV and the 1229-keV γ-ray transitions, the assignments are taken from [110]. Figure 6.2b shows a $\gamma\gamma$-coincidence on the region of the $2^+_1 \rightarrow 0^+_1$ transition energy. Note that the self-coincidence of this region stems from Compton events of higher-energy transitions, as explained in section 5.7. The fact that all transitions are observed in the $\gamma\gamma$-coincidence spectrum is in agreement with the assignments. The proposed level scheme is shown in figure 6.3. Dashed arrows denote transitions known from [110, 111, 112] and solid lines mark transitions only observed within this work.

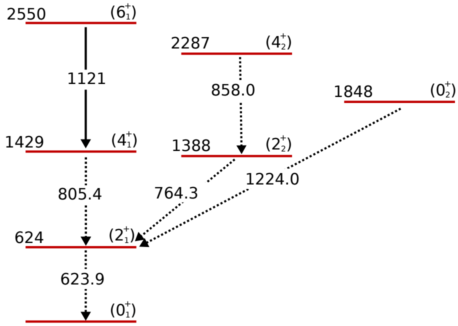

Figure 6.3.: Measured transition energies and proposed level scheme of ^{84}Ge. Dashed arrows denote transition energies taken from literature [110, 111, 112].

^{86}Ge

^{86}Ge is populated by one knock-out reaction channel, as illustrated in figure 5.24c. The Doppler-corrected DALI2 spectrum after the ^{87}As $(p, 2p)$ reaction and a $\gamma\gamma$-coincidence gate on the region of the strongest transition are depicted in figure 6.4. Doppler-corrected DALI2 spectra after this reaction are shown in appendix B.1.4 for different multiplicities. The number of γ rays detected at the same time is limited to two for figure 6.4a and to three for figure 6.4b. The fit of the DALI2 spectrum, as described in section 5.6, yields seven transitions. The observed transitions are presented in table 6.3, such as the level half-lifes used for the simulation. Only one transition at 527 keV is known from β-delayed spectroscopy [117], which is in good agreement with the observed 534-keV transition. Regarding a typical γ-ray spectrum after a knock-out reaction [113, 114, 115, 116], the strongest transition at 534 keV is assigned to be the $(2_1^+) \rightarrow (0_1^+)$ transition and the second strongest transition at 794 keV is allocated to the $(4_1^+) \rightarrow (2_1^+)$ decay. Two important observations can be made in the $\gamma\gamma$-coincidence gate on the energy region of the strongest transition shown in figure 6.4b. In comparison to the $\gamma\gamma$-coincidence

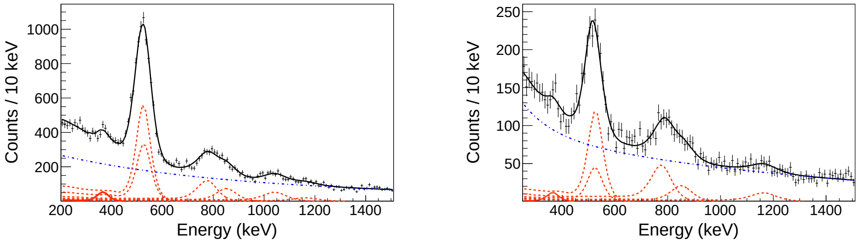

(a) Doppler-corrected DALI2 spectrum for multiplicity ≤ 2.

(b) $\gamma\gamma$-coincidence spectrum gated on the region of the doublet for multiplicity ≤ 3.

Figure 6.4.: Doppler-corrected DALI2 spectrum and $\gamma\gamma$-coincidence spectrum gated on the region of the $2_1^+ \rightarrow 0_1^+$ after the reaction ^{87}As$(p,2p)^{86}$Ge. Different multiplicities are shown.

Table 6.3.: Obtained transition energies after the reaction ^{87}As $(p,2p)$ ^{86}Ge, together with the half-lifes used for the simulation. The corresponding cross sections are given in table 6.8.

Transition energy (keV)	$T_{1/2}$ **(ps)**
371^{+16}_{-8}	0^{+100}_{-0}
510 ± 19	30 ± 30
534 ± 8	30^{+20}_{-25}
794^{+13}_{-15}	80 ± 50
861^{+17}_{-19}	50 ± 50
1064^{+10}_{-14}	80^{+30}_{-40}
1182^{+19}_{-25}	55 ± 55

gate on the region of the $2_2^+ \rightarrow 0_1^+$ transition of ^{84}Ge, shown in figure 6.1a, the observed self-coincidence of this region is much stronger. Since, the strength of the transition cannot be explained by the characteristics of $\gamma\gamma$-coincidence spectra using DALI2 (see section 5.7) it is a hint for a doublet at this energy. Furthermore, a transition at 1064 keV is observed in the DALI2 spectrum in figure 6.4a which is absent in the $\gamma\gamma$-coincidence spectrum presented in figure 6.4b. Within the uncertainties, the sum of γ rays at 510 keV and 534 keV, forming the doublet, agrees with the 1064-keV transition energy. Therefore, the 1064-keV γ ray is assigned

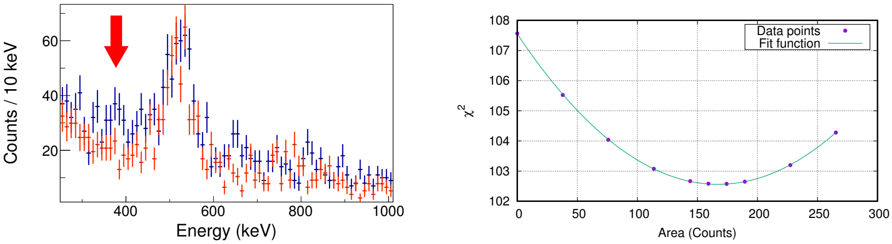

(a) Gate on the energy region of the $2_2^+ \rightarrow 0_1^+$ transition (blue) compared to a gate at ~ 1360 keV, where no transition is observed (red).

(b) Resulting χ^2, using different areas of the 371-keV transition for the fit.

Figure 6.5.: $\gamma\gamma$-coincidence spectrum gated on the region of the $2_2^+ \rightarrow 0_1^+$ compared to a background gate for multiplicity ≤ 3 and a χ^2 analysis for the observed area of the 371-keV transition.

to the $(2_2^+) \rightarrow (0_1^+)$ transition and the γ-rays forming the doublet are assigned to the competitive $(2_2^+) \rightarrow (2_1^+) \rightarrow (0_1^+)$ decay path. According to the systematics of ^{84}Ge, the 1182-keV and 861-keV γ-rays are assigned to the $(6_1^+) \rightarrow (4_1^+)$ and $(4_2^+) \rightarrow (2_2^+)$ decays. The transition at 371 keV appears in the $\gamma\gamma$-coincidence gate of the $(2_1^+)/(2_2^+)$ doublet and it is visible in a gate on the $(2_2^+) \rightarrow (0_1^+)$ transition shown in figure 6.5a. The transition does not appear with a gate on the neighboring region (~ 1360 keV). Possible spin assignments for the level of this transition are 0^+ and 3^+. By the 1229-keV transition of ^{84}Ge it can be seen that a 0^+ state would dominantly decay to the 2_1^+. In contrast to this, the main branch of a 3^+ state would be the decay to the 2_2^+. Therefore, the 371-keV transition is tentatively assigned to the $(3_1^+) \rightarrow (2_2^+)$ decay. This assignment is in good agreement with predictions from state-of-the-art theories discussed in section 7.1.1. Since the (3_1^+) state is central for the following discussion, a significance test has been performed, as described in section 5.9.1. This test yields a significance of $\sim 4\sigma$ for figure 6.4a and $> 2\sigma$ for figure 6.4b. In addition, a χ^2 analysis has been performed for the measured area from the lineshape of the 371-keV transition shown in figure 6.5b. Therefore, the area of the lineshape is varied and the change of χ^2 is recorded. The χ^2 analysis has been performed for the DALI2 spectrum shown in figure 6.4a and shows a pronounced minimum for an area different than zero. This minimum additionally confirms the existence of a transition at this energy. The proposed level scheme for ^{86}Ge is shown in figure 6.6.

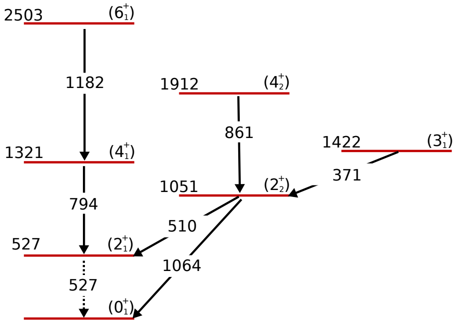

Figure 6.6.: Measured transition energies and proposed level scheme of ^{86}Ge. The dashed arrow denotes a transition energy taken from literature [117].

^{88}Ge

The Doppler-corrected γ-ray spectrum of ^{88}Ge after a ^{89}As$(p,2p)$ reaction is shown in figure 6.7a while a $\gamma\gamma$-coincidence spectrum gated on the region of the $2_1^+ \rightarrow 0_1^+$ transition is shown in figure 6.7b. The same spectra for different multiplicities are shown in appendix B.1.5. It is the first γ-ray spectroscopy of ^{88}Ge, thus all transitions are observed for the first time. The detected transition energies are listed in table 6.4, such as the half-lifes used for the simulation. The suggested

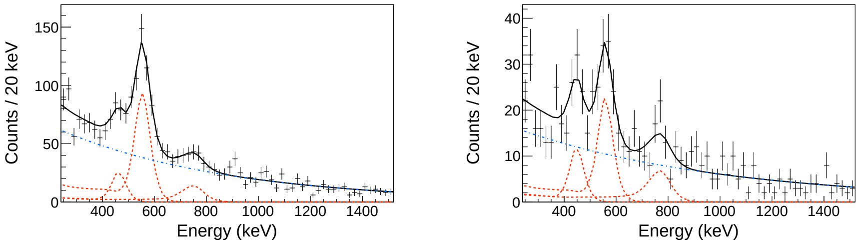

(a) Doppler-corrected DALI2 spectrum for multiplicity ≤ 6.

(b) $\gamma\gamma$-coincidence spectrum gated on the region of the $2_1^+ \rightarrow 0_1^+$ transition for multiplicity ≤ 5.

Figure 6.7.: Doppler-corrected DALI2 spectrum and $\gamma\gamma$-coincidence spectrum gated on the region of the $2_1^+ \rightarrow 0_1^+$ transition after the reaction ^{89}As$(p,2p)^{88}$Ge. Different multiplicities are shown.

Table 6.4.: Obtained transition energies after the reaction ^{89}As $(p,2p)$ ^{88}Ge, together with the half-lifes used for the simulation. The corresponding cross sections are given in table 6.9.

Transition energy (keV)	$T_{1/2}$ (ps)
462^{+20}_{-12}	0^{+100}_{-0}
551^{+12}_{-4}	0^{+50}_{-0}
760^{+33}_{-21}	60^{+210}_{-60}

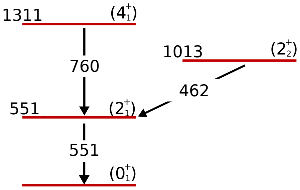

Figure 6.8.: Measured transition energies and proposed level scheme of ^{88}Ge.

level scheme of ^{88}Ge is shown in figure 6.8. According to the assignments from ^{84,86}Ge, the strongest transition at 551 keV is assigned to the $(2_1^+) \rightarrow (0_1^+)$ decay. A $\gamma\gamma$-coincidence gate yields the 462-keV and the 760-keV transition. Through the comparison to ^{86}Ge, the 462-keV and the 760-keV transitions are assigned to the $(4_1^+) \rightarrow (2_1^+)$ and the $(2_2^+) \rightarrow (2_1^+)$ decays, respectively.

6.2.2 Systematics

This section presents the behavior of 2_1^+, 4_1^+, and 2_2^+ level energies of the germanium isotopic chain from the shell closure $N = 50$ to the sub-shell closure $N = 56$ and compares this trends to even-even isotopic chains in this region. The positions of these states give a first insight on the nuclear structure. Within this work, the information is completed up to $N = 56$.

The trends of the 2_1^+ level energies for nuclei from Zr ($Z = 40$) to Ge ($Z = 32$) are depicted in figure 6.9a. The zirconium level energies peak at the sub-shell closure $N = 56$. At $N = 58$ it maintains a rather high value until it drops significantly for $N = 60$, at the onset of collectivity. For Sr, Kr, and Se, the peak at $N = 56$ vanishes and a flat behavior of the 2_1^+ level energies up to $N = 60$ is observed. Nevertheless, a slight increasing of the 2_1^+ level energies at the sub-shell closure is observed for the Kr and Ge isotopic chains.

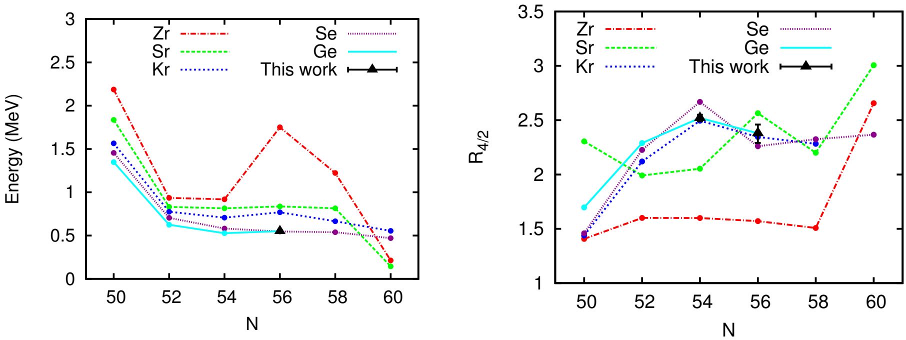

(a) Behavior of the 2_1^+ level energies. **(b)** Behavior of the $R_{4/2}$ ratio.

Figure 6.9.: Behavior of the 2_1^+ level energies and $R_{4/2}$ ratio for the isotopic chains of Zr ($Z = 40$) [24, 25, 26, 27, 28, 29], Sr ($Z = 38$) [24, 25, 26, 27, 28, 30], Kr ($Z = 36$) [24, 25, 26, 27, 30, 31, 32], Se ($Z = 34$) [31, 33, 118] and Ge ($Z = 32$) [31, 34, 110, 111, 112, 117].

The corresponding $R_{4/2}$ ratios are shown in figure 6.9b. The observed systematic trend in the Ge isotopic chain is similar to those in the Kr and Se isotopic chains, but significantly different from the observed trends in the Zr and Sr isotopic chains. An increase of $R_{4/2}$ from $N = 50$ to $N = 54$ followed by a drop towards $N = 56$ is observed for germanium. A rise of collectivity is typically reflected by a decreasing 2_1^+ level energy and an increasing $R_{4/2}$ ratio towards the rotational limits. The flat behavior of the 2_1^+ level energies of the Kr and Ge with the small kink at $N = 56$, together with the dropping $R_{4/2}$ ratio from $N = 54$ towards $N = 56$, may therefore indicate a reminder of the sub-shell closure. Thus, ^{88}Ge may be gently stabilized by the sub-shell closure $N = 56$ and the nucleus is driven back to sphericity.

Figure 6.10 shows the behavior of the 2_1^+, 4_1^+, and 2_2^+ level energies for the Ge isotopes from $N = 50$ to $N = 56$. The black triangles highlight the newly obtained results from this work. At the shell closure $N = 50$, the 4_1^+ and 2_2^+ levels are near-degenerate and their level energy is a little less than double the 2_1^+ level energy. Such a low-spin spectrum is typical for a spherical, vibrational nucleus. Moving away from the shell closure towards $N = 52$, all level energies decrease equally. The 4_1^+ and 2_2^+ levels are still degenerate. Caused by the decrease in equal measure of all three states, the degenerated 4_1^+ and 2_2^+ level energies are ~ 2.5 times the 2_1^+ level energy. Regarding $N = 54$ and $N = 56$, a slightly lower 2_1^+ and 4_1^+ level energy is observed, but the 4_1^+ level energy is still ~ 2.5 times the 2_1^+ level energy. However, the 2_2^+ level drops distinctly below the 4_1^+ level and they are not degen-

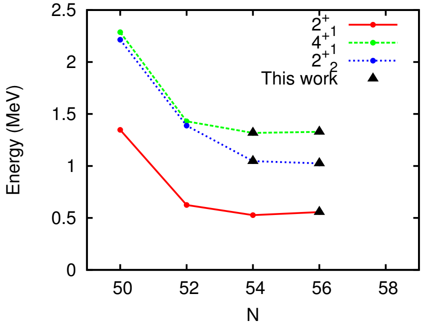

Figure 6.10.: Behavior of the 2_1^+, 4_1^+, and 2_2^+ level energies from $N = 50$ to $N = 56$. Results obtained within this work are marked by the black triangles.

erated anymore. This behavior is an indication of arising triaxial features for these nuclei. This discussion is taken up again in section 7.1.

6.2.3 Excitation cross section of a particular state

The previous section describes how the level energies for ^{84,86,88}Ge are obtained. These Ge isotopes are populated by different knock-out reactions, with different cross sections as mentioned before. The following sections explains how the excitation cross sections of a particular state is calculated for the considered reaction channels.

^{84}Ge

^{85}Ge (p, pn) ^{84}Ge

In section 5.9.1 it is described, how the cross section of particular states is calculated. The cross section for a transition with an area $A \cdot N_{BigRIPS}$ observed in the spectrum is described by equation 5.19. The Doppler-corrected DALI2 spectrum after the reaction ^{85}Ge (p, pn) ^{84}Ge is presented in figure 6.11. No constraints are set on the γ-ray multiplicity. The spectrum is fitted with the simulated lineshapes using the obtained transition energies given in table 6.2. However, an additional transition at $\sim$ 1380 keV was included to the fit to obtain a better description of the measured spectrum. A complete description of the measured spectrum is important, since the measured peak areas are used to obtain the final cross section. The DALI2 spectrum for this reaction shows transitions up to an energy of $\lesssim$ 1500 keV.

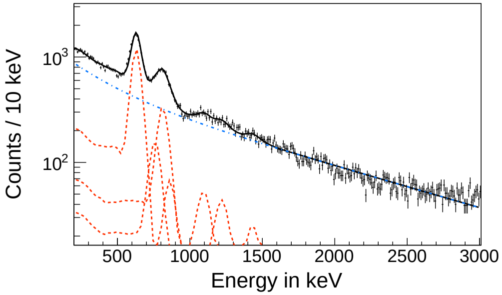

Figure 6.11.: Doppler-corrected DALI2 spectrum without constraints on the multiplicity after the reaction ^{85}Ge (p, pn) ^{84}Ge.

This part of the spectrum is described by the simulated lineshapes together with the double exponential function describing the background (compare section 5.6). At higher energies no transitions are observed and a decent description of the background is ensured by one of the exponential functions, as explained in section 5.6. Applying equation 5.19 leads to the inclusive excitation cross sections $\sigma_{inclusive}$ for the observed transitions. The result is given in table 6.5. Note, that $\sigma_{inclusive}$ does not consider feeding from higher-lying states. Therefore, $\sigma_{inclusive}$ corresponds to the observed amount of de-excitations via a certain transition. The final exclusive cross section of a particular states $\sigma_{exclusive}$ is obtained by the cross sections

Table 6.5.: Resulting inclusive excitation cross sections $\sigma_{inclusive}$, which are not taking feeding into account and the exclusive cross section of a particular state $\sigma_{exclusive}$, considering feeding, after the reaction ^{85}Ge (p, pn) ^{84}Ge.

Transition energy (keV)	Assignment	$\sigma_{inclusive}$ (mb)	State	$\sigma_{exclusive}$ (mb)
629	$2^+_1 \rightarrow 0^+_1$	23.85(97)	2^+_1	8.22(127)
803	$4^+_1 \rightarrow 2^+_1$	9.07(62)	4^+_1	6.85(70)
1121	$6^+_1 \rightarrow 4^+_1$	2.22(32)	6^+_1	2.22(32)
1229	$0^+_2 \rightarrow 2^+_1$	2.12(29)	0^+_2	2.12(29)
762	$2^+_2 \rightarrow 2^+_1$	4.43(47)	2^+_2	4.56(71)
856	$4^+_2 \rightarrow 2^+_2$	1.54(44)	4^+_2	1.54(44)
$\sim$ 1380	$(2^+_2 \rightarrow 0^+_1)$	1.67(31)		

$\sigma_{inclusive}$ of feeding states subtracted from the fed states. In consideration of the proposed level scheme of ^{84}Ge and the assumption that all feeding transitions have been observed $\sigma_{exclusive}$ is given in table 6.5. It is assumed, that the transition at $\sim$ 1380 keV stems from the known 1388-keV [110, 112, 111] γ ray corresponding to the $2^+_2 \rightarrow 0^+_1$ decay.

^{86}As $(p, 2pn)$ ^{84}Ge

The Doppler-corrected DALI2 spectrum after the reaction ^{86}As $(p, 2pn)$ ^{84}Ge without constraints on the γ-ray multiplicity is shown in figure 6.12. The fit of the measured spectrum is performed with the transition energies listed in table 6.2.

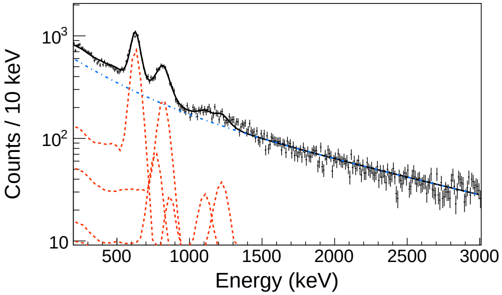

Figure 6.12.: Doppler-corrected DALI2 spectrum without constraints on the multiplicity after the reaction ^{86}As $(p, 2pn)$ ^{84}Ge.

Table 6.6.: Resulting inclusive excitation cross sections $\sigma_{inclusive}$, which are not taking feeding into account and the exclusive cross section of a particular state $\sigma_{exclusive}$, considering feeding, after the reaction ^{86}As $(p, 2pn)$ ^{84}Ge.

Transition energy (keV)	Assignment	$\sigma_{inclusive}$ (mb)	State	$\sigma_{exclusive}$ (mb)
629	$2^+_1 \rightarrow 0^+_1$	3.05(16)	2^+_1	0.89(25)
803	$4^+_1 \rightarrow 2^+_1$	1.38(11)	4^+_1	1.12(12)
1121	$6^+_1 \rightarrow 4^+_1$	0.26(5)	6^+_1	0.26(5)
1229	$0^+_2 \rightarrow 2^+_1$	0.36(5)	0^+_2	0.35(5)
762	$2^+_2 \rightarrow 2^+_1$	0.43(14)	2^+_2	0.31(19)
856	$4^+_2 \rightarrow 2^+_2$	0.11(13)	4^+_2	0.11(13)

Above ∼ 1250 keV no transmissions are observed and the measured data is well described by the fit function. The resulting $\sigma_{inclusive}$, without the consideration of feeding, is shown in table 6.6, together with $\sigma_{exclusive}$, which is regarding feeding of higher-lying states (compare table 6.3).

^{87}As $(p, 2p2n)$ ^{84}Ge

The Doppler-corrected γ-ray spectrum after the reaction ^{87}As $(p, 2p2n)$ ^{84}Ge is depicted in figure 6.13. No constraints on the γ-ray multiplicity are set. The obtained energies listed in table 6.2 are used for the simulation of the lineshapes. The

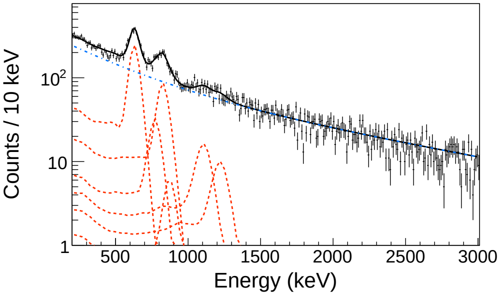

Figure 6.13.: Doppler-corrected DALI2 spectrum without constraints on the multiplicity after the reaction ^{87}As $(p, 2p2n)$ ^{84}Ge.

Table 6.7.: Resulting inclusive excitation cross sections $\sigma_{inclusive}$, which are not taking feeding into account and the exclusive cross section of a particular state $\sigma_{exclusive}$, considering feeding, after the reaction ^{86}As $(p, 2p2n)$ ^{84}Ge.

Transition energy (keV)	Assignment	$\sigma_{inclusive}$ (mb)	State	$\sigma_{exclusive}$ (mb)
629	$2_1^+ \rightarrow 0_1^+$	3.59(30)	2_1^+	0.91(42)
803	$4_1^+ \rightarrow 2_1^+$	1.72(23)	4_1^+	1.20(26)
1121	$6_1^+ \rightarrow 4_1^+$	0.52(12)	6_1^+	0.52(12)
1229	$0_2^+ \rightarrow 2_1^+$	0.34(11)	0_2^+	0.34(11)
762	$2_2^+ \rightarrow 2_1^+$	0.62(15)	2_2^+	0.49(21)
856	$4_2^+ \rightarrow 2_2^+$	0.13(14)	4_2^+	0.13(14)

areas obtained by a fit of the lineshapes to the measured spectrum are inserted into equation 5.19 to obtain $\sigma_{inclusive}$. The resulting $\sigma_{inclusive}$ for the observed γ-ray transitions are listed in table 6.7, while $\sigma_{exclusive}$ results after the consideration of feeding (compare table 6.3).

^{86}Ge

^{86}Ge is produced by a ^{87}As$(p,2p)$ reaction, and the Doppler-corrected γ-ray spectrum without a multiplicity cut is shown in figure 6.14. The fit function uses lineshapes simulated with the transition energies listed in table 6.3. In addition two lineshapes with transition energies of $\sim$ 670 keV and $\sim$ 1650 keV are used to describe the measured DALI2 spectrum. Since, the obtained area of the transitions forming the doublet at $\sim$ 520 keV can not be clearly assigned to the contributing transitions, a summed area and joined $\sigma_{inclusive} = 1.73(10)$ is calculated for the doublet. A branching ratio of $I(2_2^+ \to 2_1^+)/I(2_2^+ \to 0_1^+) = 1.6(4)$ could be obtained by comparison of a $\gamma\gamma$-coincidence spectrum with a gate on the doublet and the singles spectrum. The resulting area of the doublet in the $\gamma\gamma$-coincidence spectrum corresponds solely to the $2_2^+ \to 2_1^+ \to 0_1^+$ decay chain. Considering the efficiency of DALI2 this area can be related to the observed area of the $2_2^+ \to 0_1^+$ transition in the singles spectrum. The resulting $\sigma_{exclusive}$ after the consideration of feeding is presented in table 6.8. The additional transitions at energies of $\sim$ 670 keV and $\sim$ 1650 keV are not placed in the level scheme. This causes eventual feeding of the considered states, leading to a reduction of $\sigma_{exclusive}$ of 0.11(3) mb. This reduction is not considered in table 6.8.

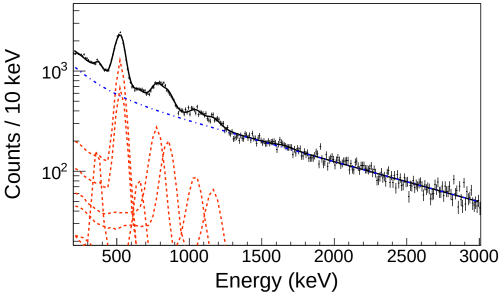

Figure 6.14.: Doppler-corrected DALI2 spectrum without constraints on the multiplicity after the reaction ^{87}As $(p,2p)$ ^{86}Ge.

Table 6.8.: Resulting inclusive excitation cross sections $\sigma_{inclusive}$, which are not taking feeding into account and the exclusive cross section of a particular state $\sigma_{exclusive}$, considering feeding, after the reaction ^{87}As $(p,2p)$ ^{86}Ge.

Transition energy (keV)	Assignment	$\sigma_{inclusive}$ (mb)	State	$\sigma_{exclusive}$ (mb)
371	$3_1^+ \rightarrow 2_2^+$	0.09(2)	2_1^+	0.70(16)
510	$2_2^+ \rightarrow 2_1^+$	0.30(8)	3_1^+	0.09(2)
534	$2_1^+ \rightarrow 0_1^+$	1.43(13)	4_1^+	0.27(3)
794	$4_1^+ \rightarrow 2_1^+$	0.43(3)	6_1^+	0.16(2)
861	$4_2^+ \rightarrow 2_2^+$	0.34(2)	2_2^+	0.06(9)
1064	$2_2^+ \rightarrow 0_1^+$	0.19(2)	4_2^+	0.34(2)
1181	$6_1^+ \rightarrow 4_1^+$	0.16(2)		
~ 670	–	0.08(2)		
~ 1650	–	0.03(2)		

^{88}Ge

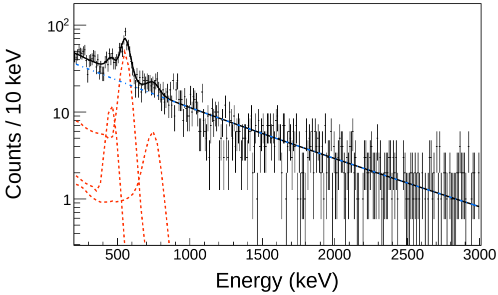

Figure 6.15.: Doppler-corrected DALI2 spectrum without constraints on the multiplicity after the reaction ^{89}As $(p,2p)$ ^{88}Ge.

The Doppler-corrected γ spectrum from the reaction ^{89}As$(p,2p)^{88}$Ge without DALI2-multiplicity constraints is presented in figure 6.15. The measured spectrum is described by three simulated lineshapes with the transition energies listed in table 6.4 and a double exponential function. No additional transitions are observed in the DALI2 spectrum. The obtained $\sigma_{inclusive}$ and $\sigma_{exclusive}$ are shown in table 6.9.

Table 6.9.: Resulting inclusive excitation cross sections $\sigma_{inclusive}$, which are not taking feeding into account and the exclusive cross section of a particular state $\sigma_{exclusive}$, considering feeding, after the reaction ^{89}As $(p,2p)$ ^{88}Ge.

Transition energy (keV)	Assignment	$\sigma_{inclusive}$ (mb)	State	$\sigma_{exclusive}$ (mb)
551	$2^+_1 \rightarrow 0^+_1$	1.44(19)	2^+_1	0.82(23)
760	$4^+_1 \rightarrow 2^+_1$	0.32(11)	4^+_1	0.32(11)
462	$2^+_2 \rightarrow 2^+_1$	0.31(9)	2^+_2	0.31(9)

6.3 p,p' reactions

6.3.1 ^{84}Ge

The Doppler-corrected DALI2 spectrum after a ^{84}Ge (p,p') ^{84}Ge reaction is shown in figure 6.16a. By restricting the detector ID from 53-186 and using a DALI2 time cut of ±10 ns, as described in section 5.9.2, the background is suppressed. The discarded γ-rays by the DALI2 time condition are shown in appendix A.6. Thus, it is evident that no de-exciting γ-rays from the nucleus of interest are discarded. Four transitions are observed in the spectrum, presented in figure 6.16a.The γ-ray transitions at 629 keV, 803 keV, and 762 keV are known from the analysis

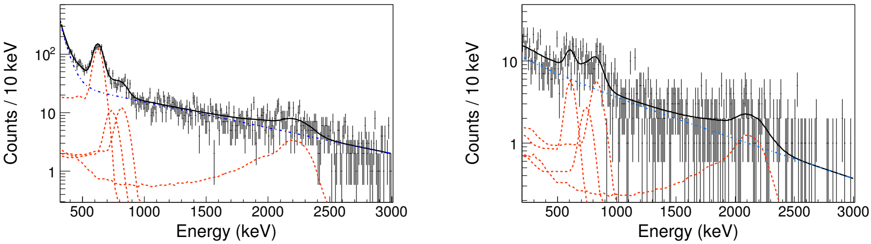

(a) Doppler-corrected DALI2 spectrum without constraints on the multiplicity after the reaction ^{84}Ge (p,p') ^{84}Ge.

(b) $\gamma\gamma$-coincidence spectrum gated on the region of the $2^+_1 \rightarrow 0^+_1$ transition (550-700 keV).

Figure 6.16.: Doppler-corrected DALI2 spectrum and $\gamma\gamma$-coincidence spectrum gated on the region of the $2^+_1 \rightarrow 0^+_1$ transition after the reaction ^{84}Ge$(p,p')^{84}$Ge.

of the knock-out reactions (compare section 6.2.1). Therefore, these transition energies are used for three of the simulated lineshapes. Furthermore, an additional transition at 2270(34) keV has been observed. The $\gamma\gamma$-coincidence spectrum gated on the region of the $2_1^+ \rightarrow 0_1^+$ transition yields the 629 keV, 803 keV, and 762 keV and 2270 keV γ rays. The presence of the 629-keV γ ray in the gate on the region of 490-560 keV is caused by the underlying Compton scattered events underneath the $2_1^+ \rightarrow 0_1^+$ transition as explained in section 5.7. The newly observed 2270-keV γ ray is tentatively assigned to be a $3_1^- \rightarrow 2_1^+$ decay. This assumption is based on the fact, that one-phonon states have significantly high cross sections for (p,p') reactions. With the amplitudes A, obtained from the fit of the measured spectrum, the inclusive excitation cross section $\sigma_{inclusive}$ is calculated by equation 5.21. Note, that $\sigma_{inclusive}$ does not take into account feeding of higher transition. The obtained $\sigma_{inclusive}$ for the ^{84}Ge (p,p') ^{84}Ge reaction are listed in table 6.10. By consideration of the level assignments shown in figure 6.3 and the assumption that the 2270 keV is decaying to the 2_1^+ state the exclusive cross section of a particular state $\sigma_{exclusive}$ is obtained.

Table 6.10.: Resulting inclusive excitation cross sections $\sigma_{inclusive}$, which is not taking into account feeding and the exclusive cross section of a particular state $\sigma_{exclusive}$, considering feeding, after the reaction ^{84}Ge (p,p') ^{84}Ge.

Transition energy (keV)	Assignment	$\sigma_{inclusive}$ (mb)	State	$\sigma_{exclusive}$ (mb)
629	$2_1^+ \rightarrow 0_1^+$	4.08(18)	2_1^+	2.49(26)
803	$4_1^+ \rightarrow 2_1^+$	0.57(11)	4_1^+	0.57(11)
762	$2_2^+ \rightarrow 2_1^+$	0.47(12)	2_2^+	0.47(12)
2270	$3_1^- \rightarrow 2_1^+$	0.55(8)	3_1^-	0.55(8)

6.3.2 ^{86}Ge

^{86}Ge is excited via a (p,p') reaction. The corresponding Doppler-corrected γ-ray spectrum using a DALI2 time cut and an ID restriction, as explained in section 5.9.2, is shown in figure 6.17a. The discarded γ rays are shown in appendix A.6. The plot yields no peaks, and therefore, no γ decays stemming from the considered reaction are discarded. Figure 6.17a depicts seven transitions, while five of them are at energies of 534 keV, 510 keV, 794 keV, 861 keV, and 1064 keV and are known from the knock-out reaction, discussed in section 6.2.1. In addition, two transitions at 677(46) keV and 2154(22) keV are observed in the (p,p') reaction channel. A gate

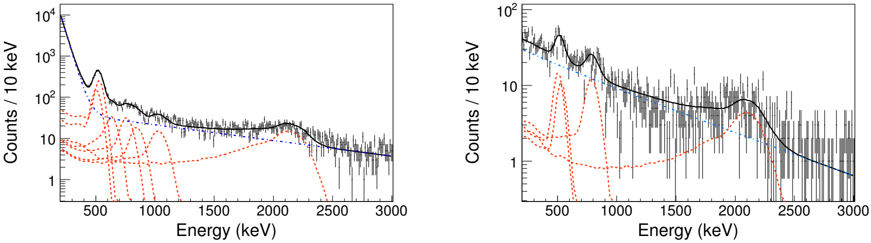

(a) Doppler-corrected DALI2 spectrum without constraints on the multiplicity after the reaction ^{86}Ge (p,p') ^{86}Ge.

(b) $\gamma\gamma$-coincidence spectrum gated on the region of the doublet (440-590 keV).

Figure 6.17.: Doppler-corrected DALI2 spectrum and $\gamma\gamma$-coincidence spectrum gated on the region of the $2_1^+ \rightarrow 0_1^+$ transition after the reaction ^{86}Ge$(p,p')^{86}$Ge.

on the region of the doublet yields the 794-keV and 2154-keV γ rays. The newly observed 2154-keV γ ray is tentatively assigned to be a $3_1^- \rightarrow 2_1^+$ decay. A similar structure with an observed 3^- state at 2692 keV, which is dominantly decaying to the 2^+1 by a 2129-keV γ ray is known in ^{76}Ge [119] (in section 7.1.2 it is highlighted that there are strong similarities between ^{76}Ge and ^{86}Ge). As explained in section 5.9.2, $\sigma_{inclusive}$ is calculated. The result of this calculation is presented in table 6.11. Since, the obtained area of the transitions forming the doublet at

Table 6.11.: Resulting inclusive excitation cross sections $\sigma_{inclusive}$, which is not taking feeding into account and the exclusive cross section of a particular state $\sigma_{exclusive}$, considering feeding, after the reaction ^{86}Ge (p,p') ^{86}Ge.

Transition energy (keV)	Assignment	$\sigma_{inclusive}$ (mb)	State	$\sigma_{exclusive}$ (mb)
510	$2_2^+ \rightarrow 2_1^+$	0.78(22)	2_1^+	1.99(48)
534	$2_1^+ \rightarrow 0_1^+$	4.64(40)	4_1^+	0.67(14)
794	$4_1^+ \rightarrow 2_1^+$	0.67(14)	2_2^+	0.79(27)
861	$4_2^+ \rightarrow 2_2^+$	0.48(14)	4_2^+	0.48(14)
1064	$2_2^+ \rightarrow 0_1^+$	0.49(6)	3_1^-	1.20(7)
2154	$3_1^- \rightarrow 2_1^+$	1.20(7)		
677	–	0.57(9)		

$\sim$ 520 keV can not be clearly assigned to the contributing transitions, a summed area and joint $\sigma_{inclusive} = 5.42(33)$ is calculated for the doublet. The $\sigma_{inclusive}$ for the transitions at 534 keV and 510 keV are calculated using the branching ratio of 1.6(4) obtained in section 6.2.3. Incorporating the level scheme of ^{86}Ge, yields $\sigma_{exclusive}$, which is considering feeding. The transition at 677 keV is not placed in the level scheme and is not considered for the feeding corrections.

6.3.3 ^{94}Kr

Figure 6.18a presents the Doppler-corrected DALI2 spectrum after a $^{94}\mathrm{Kr}\,(p,p')\,^{94}\mathrm{Kr}$ reaction. As explained in section 5.9.2 the background is reduced by a DALI2-time gate and an ID restriction. The discarded γ radiation is shown in appendix A.6.

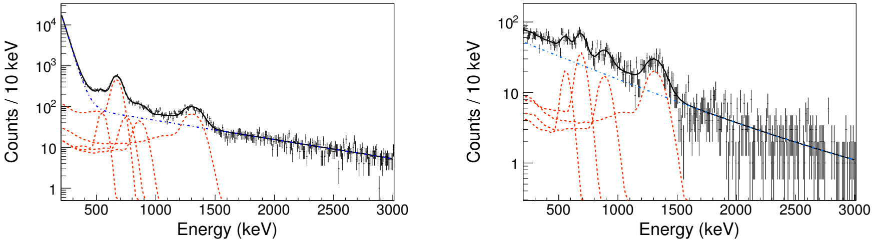

(a) Doppler-corrected DALI2 spectrum after the reaction $^{94}\mathrm{Kr}\,(p,p')\,^{94}\mathrm{Kr}$.

(b) $\gamma\gamma$-coincidence spectrum gated on the region of the $2^+_1 \rightarrow 0^+_1$ transition (590-740 keV).

Figure 6.18.: Doppler-corrected DALI2 spectrum and $\gamma\gamma$-coincidence spectrum gated on the region of the $2^+_1 \rightarrow 0^+_1$ transition after the reaction $^{94}\mathrm{Kr}(p,p')^{94}\mathrm{Kr}$.

Five transitions are observed in figure 6.18a. While the transition energies at 665 keV, and 853 keV are known from [120], the 550-keV γ ray was observed in the knock-out reactions [101]. The two transitions at 734(12) keV and 1286(9) keV are observed in (p,p'), solely. Figure 6.18b presents a gate on the region of the $2^+_1 \rightarrow 0^+_1$ transition and yields the 550-keV, 665 keV, 853-keV and 1286-keV γ rays. The presence of the 665-keV γ ray in the gate on the region of 490-560 keV can be explained by underlying Compton scattered events underneath the $2^+_1 \rightarrow 0^+_1$ transition as described in section 5.7. Since 3^- states are highly likely for (p,p') reactions caused by their one phonon character and the fact that the 734-keV and 1286-keV transitions arise solely in the (p,p') channel, they may stem from a com-

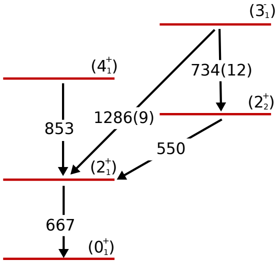

Figure 6.19.: Proposed level scheme of ^{94}Kr.

mon 3^- state. The γ-ray energies of 550 keV and 734 are preliminarily assigned to the cascade $3^-_1 \rightarrow 2^+_2 \rightarrow 2^+_1$. They agree within their uncertainties with the 1286-keV γ ray, which is therefore assigned to the $3^-_1 \rightarrow 2^+_1$. The resulting $\sigma_{inclusive}$, which is not taking into account feeding, and $\sigma_{exclusive}$, using the assignment shown in figure 6.19, are given in table 6.12. Since, the assignments are not ensured, the possible feeding of the 2^+_1 state by the 734-keV γ-ray is considered within the errors of $\sigma_{exclusive}(2^+_1)$ as an additional systematic error.

Table 6.12.: Resulting inclusive excitation cross sections $\sigma_{inclusive}$, which is not taking into account feeding and the exclusive cross section of a particular state $\sigma_{exclusive}$, considering feeding, after the reaction ^{94}Kr (p,p') ^{94}Kr.

Transition energy (keV)	**Assignment**	$\sigma_{inclusive}$ **(mb)**	**State**	$\sigma_{exclusive}$ **(mb)**
665[1]	$2^+_1 \rightarrow 0^+_1$	6.26(15)	2^+_1	$2.35^{+0.20}_{-0.20}{}_{-0.93}$
853[1]	$4^+_1 \rightarrow 2^+_1$	0.87(8)	4^+_1	0.87(7)
550[1]	$2^+_2 \rightarrow 2^+_1$	0.73(8)	2^+_2	0.00(14)
734	$3^-_1 \rightarrow 2^+_2$	0.82(11)	3^-_1	3.13(14)
1286	$3^-_1 \rightarrow 2^+_1$	2.31(10)		

[1] Taken from [120]

6.3.4 ^{96}Kr

The Doppler-corrected DALI2 spectrum after the reaction ^{96}Kr (p,p') ^{96}Kr, without constraints on the γ-ray multiplicity is depicted in figure 6.20a. The shown γ spectrum uses a DALI2-time gate and a restriction on the detector ID, as explained in

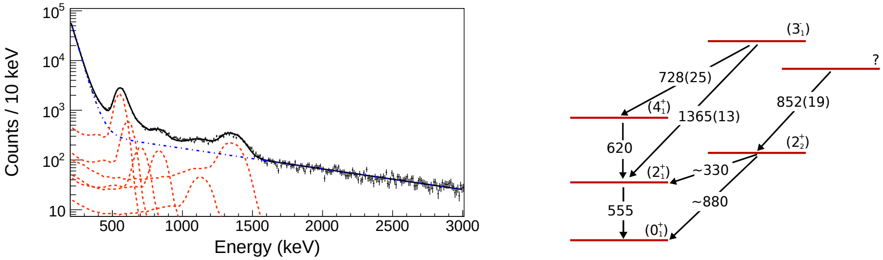

(a) Doppler-corrected DALI2 spectrum after the reaction ^{96}Kr (p,p') ^{96}Kr.

(b) Proposed level scheme of ^{96}Kr.

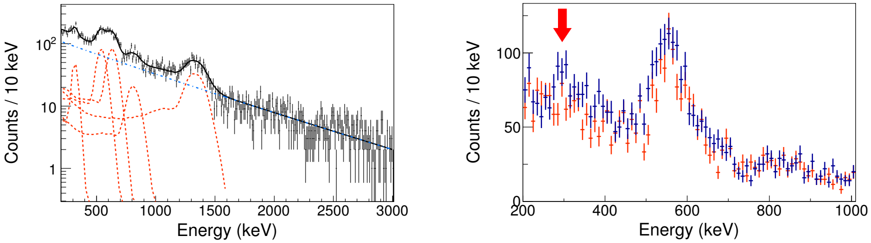

(c) $\gamma\gamma$-coincidence spectrum gated on the left half of the $2^+_1 \rightarrow 0^+_1$ transition (490-560 keV).

(d) $\gamma\gamma$-coincidence spectrum gated on the region of 780-850 keV (blue) and 860-930 keV (red).

Figure 6.20.: Doppler-corrected DALI2 spectrum and $\gamma\gamma$-coincidence spectra gated on different energy regions after the reaction ^{96}Kr (p,p') ^{96}Kr and the proposed level scheme of ^{96}Kr.

section 5.9.2. No γ-rays corresponding to de-excitations of ^{96}Kr are discarded by the DALI2-time gate. The discarded γ rays are depicted in appendix A.6. In figure 6.20a, six γ-ray transitions are observed. The transitions at 555 keV and 620 keV correspond to the $2^+_1 \rightarrow 0^+_1$ and $4^+_1 \rightarrow 2^+_1$ decay chains and are known from [121], while the transitions at 728(25) keV, 852(19) keV, 1170(40) keV, and 1365(13) keV are observed after a (p,p') reaction, solely. The corresponding $\sigma_{inclusive}$, which is not taking into account feeding, is shown in table 6.13. In addition a $\gamma\gamma$-coincidence spectrum gated on the region of the $2^+_1 \rightarrow 0^+_1$ transition is shown in figure 6.20c. The gate on the $2^+_1 \rightarrow 0^+_1$ transition yields the 555-keV, 620-keV, 852-keV and 1365-keV γ rays, furthermore a transition at $\sim$ 330 keV is observed. The presence of the 555-keV γ ray in the gate on the region of 490-560 keV is caused by the underly-

ing Compton scattered events underneath the $2^+_1 \rightarrow 0^+_1$ transition as explained in section 5.7. The transition at $\sim$ 330 keV is also observed in a gate on the energy region of 780-850 keV, while it is absent in a gate on the energy region of 860-930 keV shown in figure 6.20d by the blue and red histogram. The blue histogram shows γ-ray transitions coincident to the energetically lower half of the 852-keV transition, while the red histogram shows coincident γ rays to the energetically higher half of the 852-keV transition. This observation might be a hint for an unobserved doublet at the energy range of the 852-keV transition. The hypothesis is further confirmed by observations from the $^{97}\mathrm{Rb}(p, 2p)^{96}\mathrm{Kr}$ reaction channel analyzed by Kevin Moschner (Cologne). This analysis yields two γ rays at $\sim$ 330 keV and $\sim$ 880 keV tentatively assigned to the $2^+_2 \rightarrow 2^+_1$ and $2^+_2 \rightarrow 0^+_1$, respectively [101]. The efficiency corrected intensity ratio of these transitions is 1.0(2) [101].
In the following, this assignment is checked on compatibility based on the observed intensities. A gate on the $2^+_1 \rightarrow 0^+_1$ transition energy can be used to obtain the number of coincident 853-keV γ rays and calculate the expected γ rays of the 853-keV transition in the singles spectrum. It follows that 72(13)% of the observed intensity of the 853-keV transition in the singles spectrum is expected from the number coincident γ rays. The missing intensity might correspond to the unobserved $\sim$ 880 keV transition, which can be extracted indirectly by an intensity analysis of the $\sim$ 330 keV γ ray transition. The observed intensity of the $\sim$ 330 keV γ ray corresponds to 34(8)% of the observed intensity of the 853-keV transition in

Table 6.13.: Resulting inclusive excitation cross sections $\sigma_{inclusive}$, which is not taking into account feeding and the exclusive cross section of a particular state $\sigma_{exclusive}$, considering feeding, after the reaction ^{96}Kr (p, p') ^{96}Kr.

Transition energy (keV)	**Assignment**	$\sigma_{inclusive}$ **(mb)**	**State**	$\sigma_{exclusive}$ **(mb)**
555[1]	$2^+_1 \rightarrow 0^+_1$	7.92(33)	2^+_1	$3.19^{+0.37}_{-0.37\ -1.82}$
620[1]	$4^+_1 \rightarrow 2^+_1$	1.87(11)	4^+_1	1.30(11)
728(25)	$3^-_1 \rightarrow 4^+_1$	0.57(5)	2^+_2	0.00(10)
1365(13)	$3^-_1 \rightarrow 2^+_1$	2.59(12)	3^-_1	3.16(13)
852(19)	–	0.78(6)		
1170(40)	–	0.46(5)		
$\sim$ 330[2]	$2^+_2 \rightarrow 2^+_1$	0.27(7)		

[1] Taken from [121].

[2] Taken from [101]

the singles spectrum. Using the intensity ratio 1.0(2) [101] of the $\sim$ 330 keV and $\sim$ 880 keV transitions, it follows that the $\sim$ 880 keV transition covers 34(10)% of the 853-keV transition in the singles spectrum. This matches the missing intensity expected from the coincidence analysis and consolidates the presumption of a doublet at 853 keV. Therefore, the $\sim$ 330 keV transition is tentatively assigned to the $2_2^+ \rightarrow 2_1^+$ and its $\sigma_{inclusive}$ obtained from the $\gamma\gamma$-coincidence spectrum is given in table 6.13. The part of the 853-keV transition which is in coincidence to the $\sim$ 330-keV transition is assigned to be a feeder of the 2_2^+ state, but its spin is unassigned. The observed transitions at 728 keV and 1365 keV are tentatively assigned to a common 3^- state. This assignment is based on the following facts. A common 3^- state is highly likely populated by (p, p') reactions caused by its one phonon character. In addition the transition energies 620 keV and 728 keV sum up to 1365 keV transition within their uncertainties. Therefore, they are tentatively assigned to the competing decay branches $3_1^- \rightarrow 4_1^+ \rightarrow 2_1^+$ and $3_1^- \rightarrow 2_1^+$, respectively. A proposed level scheme for the observed transitions is depicted in figure 6.20b. Considering feeding on bases of the assignments shown in 6.20b, yields $\sigma_{exclusive}$. Since, the level assignment are not ensured, the feeding of all observed γ rays is considered in the error of $\sigma_{exclusive}(2_1^+)$.

7 Discussion

7.1 Knock-out reactions

7.1.1 Comparison to theoretical predictions

This sections compares the spectroscopic results presented in section 6.2.1 with predictions of different theories.

Within this work an IBM-2 calculation for ^{86}Ge was performed. This calculation was done with the software NPBOS [122]. The IBM-2 was chosen since it is known to achieve successful descriptions of γ-soft nuclei and it is further known that γ softness plays crucial role for nuclei in this region. Within the IBM-2, γ-soft nuclei are described by the dynamical symmetry $O(6)$, as explained in section 3.4.

In order to reproduce the experimentally obtained spectrum of ^{86}Ge the following IBM-2 parameters are applied: $\epsilon_d = 0.169$, $\kappa = -0.306$, $\kappa_\nu = \kappa_\pi = -0.153$, $\chi_\nu = -\chi_\pi = 1$, $\xi = 0.6$ and $\xi_3 = -0.5$. This set of parameters, especially χ_ν, χ_π, ξ and ξ_3, are needed to reproduce the energy spacing in the γ band. The use of these parameterization leads to the breaking of the $O(6)$ symmetry. Beside this all the states in the γ band turn out to be mixed symmetry states (indicated by $F < F_{max}$). The description of the γ band states by mixed-symmetric states is quite unexpected and is questioning the credibility of the whole calculation. Furthermore, the IBM-2 calculation predicts an exclusive $2^+_2 \rightarrow 2^+_1$ decay path, while the $2^+_2 \rightarrow 0^+_1$ branch is suppressed entirely. This is in contradiction with the experimentally observed intensity ratio $I(2^+_2 \rightarrow 2^+_1)/I(2^+_2 \rightarrow 0^+_1) = 1.6(4)$ (compare section 6.2.3). Due to this contradiction, an essential conclusion can be drawn. The observed experimental spectrum of ^{86}Ge cannot be described in a meaningful manner by a model known to achieve remarkable results for the description of γ-soft nuclei.

In order to gain a deeper insight on the structure of ^{84,86,88}Ge the experimental results are compared to a shell model calculation [123] and to a SCCM calculation [124], in the following. The obtained experimental level schemes of ^{84,86,88}Ge are shown in figure 7.1 by the red levels. The green dotted levels depict the predictions from a shell model calculation by Sieja. The shell model results are achieved in a model space $\pi(1f_{5/2}, 2p_{3/2}, 2p_{1/2}, 1g_{9/2})$ for protons and

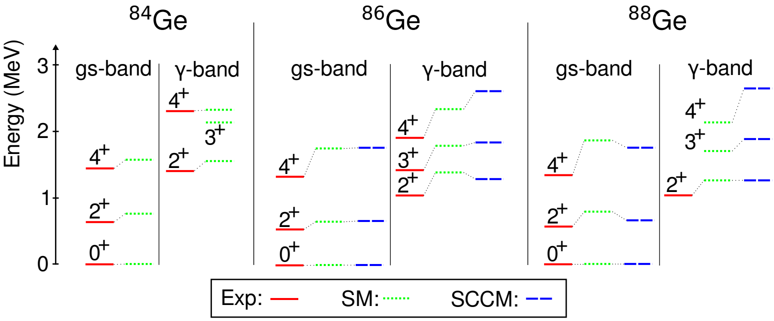

Figure 7.1.: Systematics of the experimental ^{84,86,88}Ge level energies compared to theoretical predictions from shell model (SM) [123] and SCCM [124]. The shell model calculation for ^{84}Ge is taken from [78].

$\nu(2d_{5/2}, 3s_{1/2}, 2d_{3/2}, 1g_{7/2}, 1h_{11/2})$ for neutrons outside an inert ^{78}Ni core. Furthermore, an effective interaction consisting of three parts is used. It contains a fit from [125] in its proton-proton part. It uses the neutron-neutron interaction called GCN5082 [126, 127] and the proton-neutron realistic G-matrix to reproduce the shell evolution between ^{91}Zr and ^{101}Sn. For more information on this calculation the author refers to [78, 128]. The blue dotted lines mark the results from a SCCM calculation by Rodríguez, as described in section 3.3 and in [77, 78, 129].

The predicted sequences of the states from shell model and SCCM are in good agreement with the proposed level schemes. However, both theoretical calculations overestimate the level energies in all cases. For the SCCM calculation it is known, that it predicts wrong moment of inertia and therefore a stretching of the level schemes compared to experimental results. This situation can be corrected by the cranking procedure [130], though cranking is not applied for the SCCM calculation presented in this work. However, structural informations are derived from energy ratios of the observed states and not their absolute values. Both theories predict a $R_{4/2}$ ratio of ~ 2.5 for ^{86,88}Ge, which agrees with the data. The shell model prediction of $R_{4/2} \approx 2$ for ^{84}Ge underestimates the experimental value of ~ 2.3, as shown in table 7.1. Interestingly, the shell model predicts a smaller $R_{4/2}$ for ^{88}Ge than for ^{86}Ge, which may indicate the effect of the sub-shell closure at $N = 56$.

The predicted low-lying γ bands for the three nuclei match the experimental result and reflect a degree of triaxiality. This is shown by the $R_{4/2}$ and $R_{2/2} = E(2^+_2)/E(2^+_1)$ ratios in table 7.1. Furthermore, the shell model and the SCCM calculation predict a 3^+_1 state which is closer to the 2^+_2 state than to the 4^+_2 state in ^{86}Ge. This energy

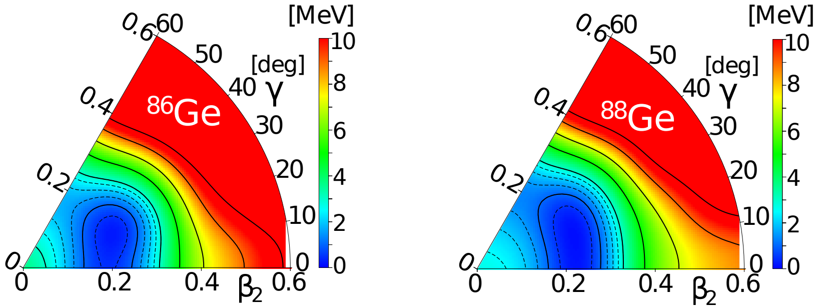

Figure 7.2.: Potential energy surfaces from the SCCM calculation presented in section 3.3 for ^{86}Ge and ^{88}Ge. The spacing between the contour lines corresponds to 2 MeV. The intermediate dashed lines correspond to steps of 0.5 MeV. The pictures are taken from [124].

spacing in the γ band reflects the properties of any good rotor with $E(J) \sim J(J+1)$. However, the predicted low-lying γ-band head is distinct from a symmetric rotor. Deeper insights of the triaxial features can be gained by the position of the odd-spin states relative to even-spin states in the γ band, as pointed out in section 1. This relative energy difference is called staggering and is defined by [131]

$$S(J) = \frac{[E(J) - E(J-1)] - [E(J-1) - E(J-2)]}{E(2_1^+)}. \tag{7.1}$$

For $J = 4$ the staggering parameter ($S(4)$) has a positive value for a rigid triaxial rotor, while it is negative for a γ-soft nucleus. $S(4)$ is positive for a well-deformed rotor with $E(J) \sim J(J+1)$ as well, but the γ-band head is located at much higher

Table 7.1.: Comparison of experimental and theoretical $R_{4/2}$ and $R_{2/2}$. The shell model calculation for ^{84}Ge is taken from [78].

	^{84}Ge		^{86}Ge			^{88}Ge		
	Exp	SM	Exp	SM	SCCM	Exp	SM	SCCM
$R_{4/2}$	2.290(4)	2.08	2.52(3)	2.69	2.66	2.38(8)	2.37	2.66
$R_{2/2}$	2.224(4)	2.05	1.99(3)	2.14	1.95	1.84(6)	1.60	1.92
$S(4)$	–	-0.52	0.23(6)	0.23	0.33	–	-0.01	0.22

energies relative to the yrast states, as mentioned before. Table 7.1 shows that the experimental $S(4)$ is in good agreement with all consulted theories. This value suggests rigid triaxiality for ^{86}Ge. This phenomenon is solely observed in ^{86}Ge. The shell model predicts $S(4) = -0.52$ for ^{84}Ge pointing towards a γ-soft nucleus. In the case of ^{88}Ge the shell model and SCCM calculation disagree. While the shell model predicts an $S(4) = -0.01$ the SCCM predicts $S(4) = 0.22$. However, both theories suggest ^{88}Ge less rigid.
Similar conclusions can be drawn from the potential energy surface from the SCCM calculation in figure 7.2. A pronounced minimum located at $\sim 30°$ is observed for ^{86}Ge. The SCCM calculation predicts the potential energy surface of ^{88}Ge very similar. However, a larger deformation parameter β and a different distribution in γ is found. No pronounced minimum is apparent and the potential has more γ softness. Nevertheless, the potential minimizes at triaxial values of γ.

7.1.2 Experimental hints for rigid triaxiality in ^{86}Ge

In section 1 it has been introduced, that rigid triaxiality is a very rare phenomena. So far, only one nucleus is known in the medium-heavy mass region $A < 100$ with rigid triaxial deformation in the ground state. This nucleus is the stable ^{76}Ge [51]. Its low-spin spectrum is shown in figure 7.3 by the blue, dashed lines. The low-spin spectrum of ^{86}Ge with the assignments of section 6.2.1 is shown by the red, solid line. Both spectra are surprisingly similar. The levels agree within 100 keV and in particular the relative positions of the odd- to even-spin members in the γ band are consistent. A comparison of the staggering parameter for both nuclei yields $S(4) = 0.091(2)$ for ^{76}Ge and $S(4) = 0.23(6)$ for ^{86}Ge. This points to an even larger degree of triaxiality for ^{86}Ge. With the tentative assignment of the 3_1^+ state

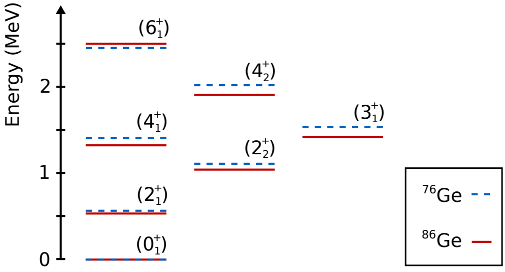

Figure 7.3.: Comparison of the low-spin spectrum of ^{76}Ge (blue, dashed) and ^{86}Ge (red, solid). The level energies of ^{76}Ge are taken from [51].

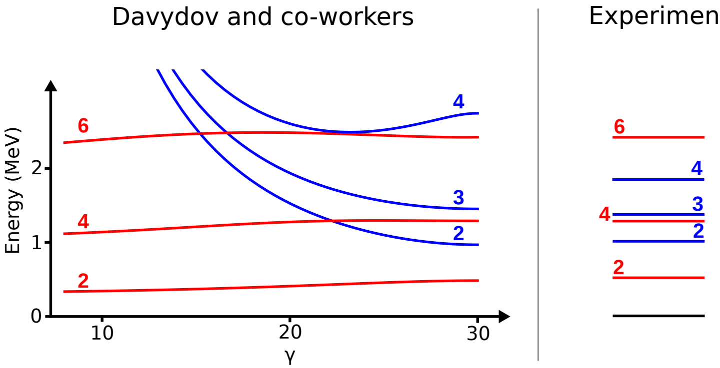

Figure 7.4.: Evolution of the low-spin spectrum for increasing γ within the model by Davydov and co-workers (see section 3.2.2) compared to the experimental spectrum of ^{86}Ge.

in ^{86}Ge this nucleus is the first candidate of a rigid, triaxial, neutron-rich nucleus. The model of Davydov and co-workers, presented in section 3.2.2, was developed to describe the energy spectra for nuclei of rigid triaxial shapes. This model makes an extreme assumption of a fixed value for the deformation parameter γ and does not assume a distribution in γ. Obviously, a nucleus described by a delta function for γ can only be an idealized limit but cannot reflect the actual nuclear shape. However, important conclusions can be drawn from the comparison to this benchmark. Figure 7.4 depicts the level energies for increasing γ within the model of Davydov and co-workers. The level energies of the ground state band (red) stay constant for increasing γ and the predicted level spacing of the ground state band is in good agreement with the experimental result. However, the level energies of the γ band are strongly dependent on the deformation parameter γ. Especially, the position of the γ-band head leads to important findings. At $\gamma \approx 23^\circ$ the 2_2^+ level energy drops below the 4_1^+ level energy. Similarly, a low 2_2^+ level energy below the 4_1^+ level energy is observed experimentally. Using equation 3.23 a deformation parameter $\gamma = 30(1)^\circ$ is obtained within the model by Davydov and co-workers.
The experimental findings of a rigid triaxial shaped nucleus with a deformation parameter $\gamma \approx 30^\circ$ is in good agreement with the prediction from theory presented before. This makes ^{86}Ge the first candidate of a rigid, triaxial, neutron-rich nucleus.

7.2 (p,p') reactions

This section aims to extract structural information out of the exclusive (p,p') cross sections for ^{84,86}Ge and ^{94,96}Kr presented in section 6.3. The exclusive cross sections for the 2_1^+ excitations are summarized in table 7.2. $\sigma_{2_1^+}$ considers feeding, which is based on the level assignments presented in sections 6.2.1 and 6.3. For ^{84}Ge and ^{86}Ge the obtained cross sections agree within the uncertainties, while an increasing cross section is observed from ^{94}Kr towards ^{96}Kr. This might be a hint for increasing collectivity.

Table 7.2.: Summary of the 2_1^+ excitation cross sections for ^{84,86}Ge and ^{94,96}Kr. The cross sections correspond to the results presented in section 6.3 regarding feeding of higher lying transitions, which is based on the presented level schemes. Since the level assignments are not ensured, possible feeding is considered as an additional systematic error.

	^{84}Ge	^{86}Ge	^{94}Kr	^{96}Kr
$\sigma_{2_1^+}$ (mb)	2.49(26)	1.99(48)	$2.35^{+0.20}_{-0.20\ -0.93}$	$3.19^{+0.37}_{-0.37\ -1.82}$

Using the coupled channel calculation code ECIS-97 [58] the cross section is related to the deformation length δ. Through this transformation it is possible to compare the (p,p') cross sections to a Coulomb measurement. This technique is adapted from [94] and is taken up again later in the text. An example of an input file is given in appendix C.1. The optical potential used for the calculation has the form as described in section 2.1.1. Namely, the Koning-Delaroche (KD02) is applied, as in [94]. Figure 7.5 shows exemplarily how the deformation is obtained for ^{84}Ge. ECIS-97 calculates cross sections for different deformation length δ. The result is shown by the red points in figure 7.5, while the red curve reflects the trend of these points. A projection of the cross section and its uncertainties on the red function leads to a value of δ with corresponding uncertainties. This procedure is indicated by the solid and dashed lines, corresponding to the relevant value and its uncertainties. The correlations of δ and the (p,p') cross section for ^{86}Ge and ^{94,96}Ge are shown in appendix C.2. Equation 3.12 relates δ_{em} to the $B(E2, 2_1^+ \rightarrow 0_1^+)$ within the model of Bohr and Mottelson. However, only Coulomb excitation data from ^{94}Kr and ^{96}Kr are available, where the $B(E2, 2_1^+ \rightarrow 0_1^+)$ was measured to $19.5^{+2.2}_{-2.1}$ W.u. and $33.4^{+7.4}_{-6.7}$ W.u. [32], respectively. Figure 7.6 depicts the resulting δ's from Coulomb excitation and (p,p') scattering, while table 7.3 summarizes the result in addition. The $\delta_{p,p'}$ values of all considered nuclei are in the order of 0.8-0.9 fm, while the δ_{em} extracted from Coulomb excitation are

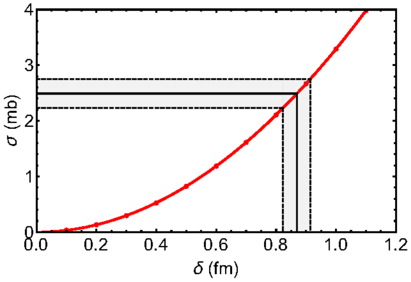

Figure 7.5.: Correlation of the deformation length and the (p,p') cross section of the 2_1^+ state. The red function shows the cross section for different δ obtained by an ECIS-97 calculation. The horizontal lines define the measured cross section with its uncertainties. Using the red function obtained from the ECIS-97 calculation the cross section can be projected to a corresponding range of δ.

above 1 fm. Furthermore, it becomes apparent that a similar trend is observed for $\delta_{p,p'}$ and δ_{em} from ^{94}Kr towards ^{96}Kr.

As mentioned in section 2.3, Coulomb excitation is probing the protons exclusively, while (p,p') scattering probes both, neutrons and protons. Since $\delta \sim Q_0$, the quadrupole moment formed by the protons is much bigger than the quadrupole moment of neutron and protons together. Furthermore, this leads to a significant difference of the neutron and proton contributions to the excitation. As described in section 2.3 the different contributions of neutrons and protons to the excitation is reflected by the M_n/M_p ratio. From a collective model $M_n/M_p = N/Z$ is expected since the proton and neutron "liquids" move in the same direction. Deviations from this simplified picture are expected from single closed shell nuclei, where nucleons occupying the closed shell do not contribute to the excitation. In the scenario depicted in figure 7.6 the proton contribution is 1.3 (1.6) times bigger

Table 7.3.: Deformation length δ calculated from (p,p') scattering and Coulomb excitation.

	^{84}**Ge**	^{86}**Ge**	^{94}**Kr**	^{96}**Kr**
$\delta_{p,p'}$ (fm)	$0.87^{+0.04}_{-0.05}$	$0.77^{+0.09}_{-0.10}$	$0.80^{\quad +0.03}_{-0.04\ -0.19}$	$0.90^{\quad +0.05}_{-0.05\ -0.34}$
δ_{em} (fm)	–	–	1.06(6)[1]	1.40(15)[1]

[1] Calculated using the $B(E2)$'s taken from [32]

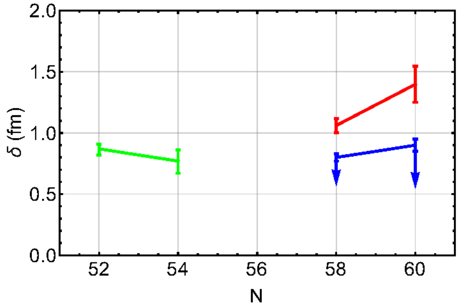

Figure 7.6.: Trends of $\delta_{p,p'}$ for Ge in green and Kr in blue. δ_{em} for Kr is shown in red. The errors illustrate the systematic errors due to the level assignment which is not ensured.

than the neutron contribution for ^{94}Kr (^{96}Kr). Such a deviation would imply significant shell effects for the neutrons. However, the shell closure is at $N = 50$ and in section 1 it is mentioned that even the sub-shell closure at $N = 56$ observed for the Zr isotopes vanishes for the Kr isotopes.

In order to explain the observed differences of $\delta_{p,p'}$ and δ_{em} the used optical potential can be considered. As described in section 2.1.1, the KD02 is valid for $24 \leq A \leq 209$ and energies between 1 keV and 200 MeV. Furthermore, the potential was not systematically tested for nuclei that far from stability. The valid energy range of the potential is well below the energies of the ions considered in this work. An extrapolation from this energy range of the model to higher energies may cause a systematic offset for the extracted cross section. Regarding figure 7.6 such an offset could cause systematic deviations of the value of $\delta_{p,p'}$. Since the considered nuclei are located in a small area of the nuclear chart the deviations of $\delta_{p,p'}$ can be assumed to be similar. Assuming that the proton and neutron contribution to the excitation is equal, which means that the deformation length of protons and neutrons is the same, $\delta_{p,p'}$ can be scaled to δ_{em}. Scaling the obtained $\delta_{p,p'}$ for ^{84,86}Ge and ^{94,96}Kr to δ_{em} for ^{94}Kr leads to figure 7.7. It should be noted that a different scaling factor could be chosen. Anyhow, it becomes clear that the trend of the Coulomb excitation measurement is observed in (p, p') as well. The increasing deformation length is equivalent to an increasing $B(E2)$, pointing towards a rise of collectivity from ^{94}Kr to ^{96}Kr.

Under the assumption that the systematic offset for the Ge isotopes is the same as the one for the Kr isotopes and considering the points made above, the $B(E2)$'s for the Ge isotopes can be predicted. As mentioned before, equation 3.12 relates

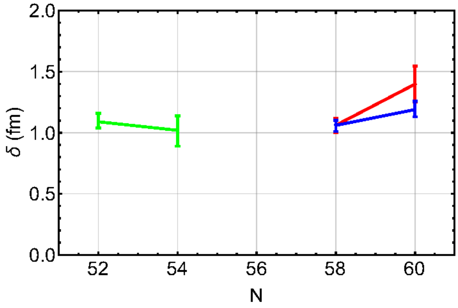

Figure 7.7.: Trends of $\delta_{p,p'}$ for Ge in green and Kr in blue. All values of $\delta_{p,p'}$ are scaled to δ_{em} of ^{94}Kr. δ_{em} for Kr is shown in red.

δ to the $B(E2, 2_1^+ \rightarrow 0_1^+)$ within the model of Bohr and Mottelson. The resulting $B(E2, 2_1^+ \rightarrow 0_1^+)$ for ^{84,86}Ge using the scaled $\delta_{p,p'}$'s are given in table 7.4. Finally, figure 7.8 shows a comparison of the obtained $B(E2, 2_1^+ \rightarrow 0_1^+)$ and the known values from literature [132]. Decreasing $B(E2, 2_1^+ \rightarrow 0_1^+)$ values are observed approaching the shell closure at $N = 50$. For $N > 50$ no literature values are available. The obtained $B(E2, 2_1^+ \rightarrow 0_1^+)$ using the scaled $\delta_{p,p'}$ suggest increasing $B(E2, 2_1^+ \rightarrow 0_1^+)$ strength after the shell closure, which indicates increasing collectivity. However, a constant $B(E2, 2_1^+ \rightarrow 0_1^+)$ strength within the uncertainties is obtained for ^{84}Ge and ^{86}Ge. This values can only be a first hint of the expected $B(E2, 2_1^+ \rightarrow 0_1^+)$ strength,

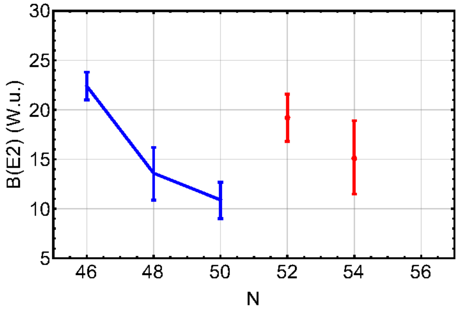

Figure 7.8.: Trend of the $B(E2, 2_1^+ \rightarrow 0_1^+)$ from literature [132] (blue) compared to the obtained $B(E2, 2_1^+ \rightarrow 0_1^+)$ values using the scaled $\delta_{p,p'}$ (red) for the germanium isotopic chain.

caused by the random choice of the scaling parameter. Nevertheless, consistent results with respect to literature are obtained for the Kr and Ge isotopes.

Table 7.4.: $B(E2, 2_1^+ \rightarrow 0_1^+)$ for ^{84}Ge and ^{86}Ge calculated using the scaled $\delta_{p,p'}$.

	^{84}Ge	**^{86}Ge**
$B(E2, 2_1^+ \rightarrow 0_1^+)$ (W.u.)	$19.2^{+2.4}_{-1.8}$	$15.1^{+3.8}_{-3.6}$

8 Summary and outlook

This work describes the spectroscopic analysis of ^{84,86,88}Ge and ^{94,96}Kr populated by different reactions within the SEASTAR campaign 2015. The analysis includes the calibration of the detector systems along the BigRIPS fragment separator and ZeroDegree spectrometer as well as the calibration of the NaI(Tl) array (DALI2) and the LH_2 target combined with a TPC (MINOS).

Different knock-out channels were used to populate neutron-rich ^{84,86,88}Ge. Occurring γ radiation emitted in flight was detected using DALI2. The γ-ray spectra after Doppler-correction were analyzed with simulated lineshapes of the observed transitions. γ-spectroscopy of neutron-rich ^{88}Ge has been performed for the first time. In total 16 transitions in ^{84,86,88}Ge have been observed ten of which so far unknown. On the basis of the observed intensities and systematics in neighboring Ge isotopes new level schemes for ^{86,88}Ge are proposed for the first time.

The tentative assignment of a 3_1^+ state in ^{86}Ge would be compatible to new shell model and SCCM predictions. Furthermore it is in good agreement with predicted level orderings from the collective model by Davydov and co-workers. This points to a degree of rigid triaxiality in this nucleus, which has previously been predicted within this broader mass region. New calculations, presented in this work, predict a maximum of triaxiality in ^{86}Ge. This work shows the first indication of rigid ground state triaxiality for this very neutron-rich region of the nuclear chart. ^{86}Ge may constitute the first example of an unstable nucleus with this feature in this newly-accessible region which is extensively discussed in view of triaxial features. More detailed future studies of this rare phenomenon are desirable, especially a firm spin assignment. An investigation of the underlying mechanisms may provide valuable conclusions on nuclear structure. The occurrence of rigid triaxiality may stem from bunching of single-particle orbitals [133]. A study of Effective Single Particle Energies (ESPEs) like in ^{110}Zr [133] could provide certainty.

In addition, a detailed analysis of reaction cross sections, as well as cross sections for the excitation of a particular state was performed. These results can serve as a first benchmark to test nuclear models for very neutron-rich nuclei. Since the RIBF belongs to the first new generation RIB facility, this data set of cross sections represents one of the first results in this exotic region of the nuclear chart.

Furthermore, ^{84,86}Ge and ^{94,96}Kr were investigated via (p, p') reactions. Different transitions in comparison to knock-out reactions arise due to the changed excitation mechanism. These transitions with considerable high cross sections for (p,p') reactions are candidates for octupole 3^- states, which are observed to decay strongly to the 2_1^+ state. The tentatively assigned 3^- states are the first benchmark for the octupole degree of freedom in this newly accessible neutron-rich region.

In addition, a comparison of the obtained (p,p') cross section and the transition strengths of the 2_1^+ state was performed on basis of the deformation length for ^{94,96}Kr. The optical potential, which best suites the experimental conditions has been used to extract the deformation length from the (p,p') cross section. Nevertheless, the comparison yields discrepancies, which may originate from the used optical potential. The applied optical potential is not systematically tested for the energies considered in this work as well as exotic nuclei far from the valley of stability. With regards to future RIB projects (e.g. NUSTAR @ FAIR) it is desirable to extend existing optical model to higher energies and more exotic regions. Data sets like the one of this work can be used to test this models.

A Supplementary data for the analysis

A.1 Particle identification - A/Q correction

As described in section 5.1.4, correlations of A/Q and the measured positions (X) and angels (A) at different focal points of BigRIPS and ZeroDegree are used to optimize the A/Q. Such correlations at the focal points F3, F5 and F11 are shown.

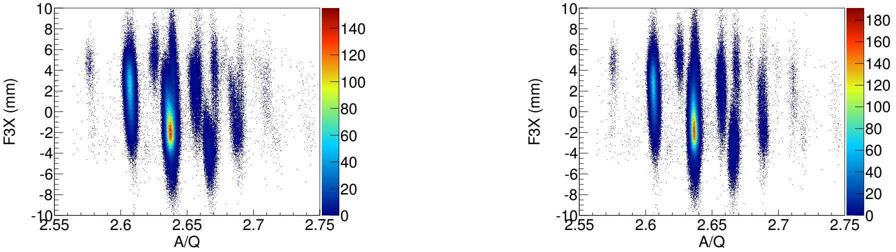

(a) Without A/Q corrections. **(b)** A/Q corrections implemented.

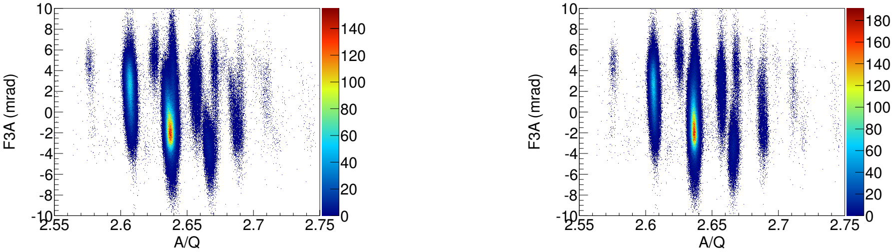

(c) Without A/Q corrections. **(d)** A/Q corrections implemented.

Figure A.1.: Impact of the A/Q corrections demonstrated by correlations of A/Q and the reconstructed positions (X) and angles (A) at the focal point F3 of BigRIPS. Panel a) and c) show uncorrected data while b) and d) depict the impact of the correction. See section 5.1.4 for more details.

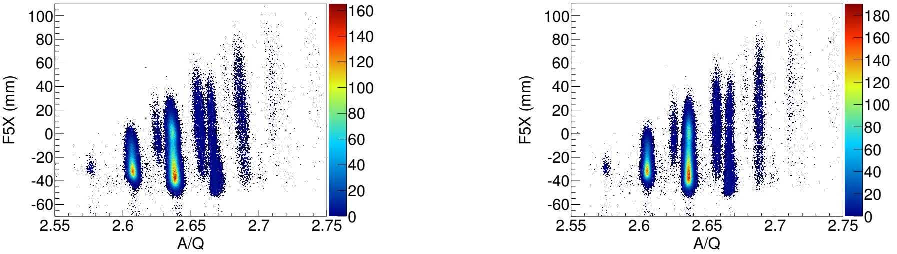

(a) Without A/Q corrections.

(b) A/Q corrections implemented.

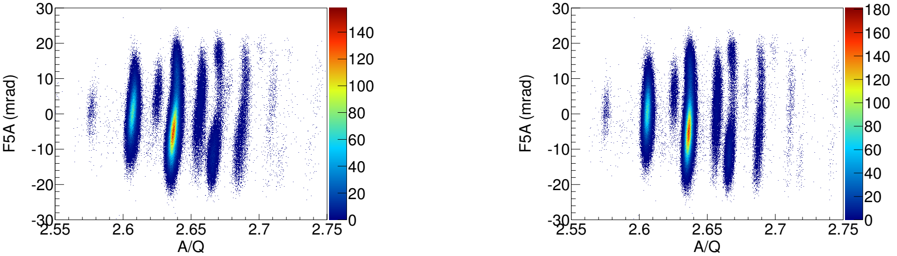

(c) Without A/Q corrections.

(d) A/Q corrections implemented.

Figure A.2.: Impact of the A/Q corrections demonstrated by correlations of A/Q and the reconstructed positions (X) and angles (A) at the focal point F5 of BigRIPS. Panel a) and c) show uncorrected data while b) and d) depict the impact of the correction. See section 5.1.4 for more details.

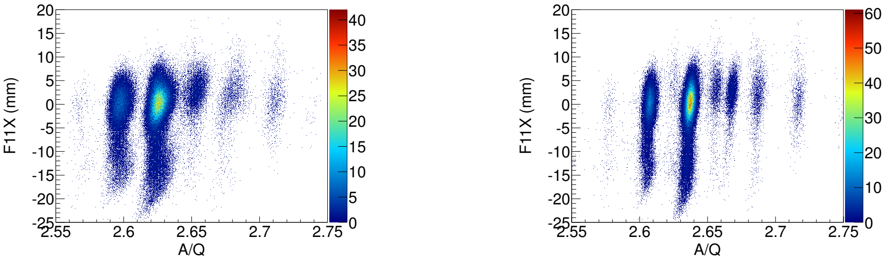

(a) Without A/Q corrections.

(b) A/Q corrections implemented.

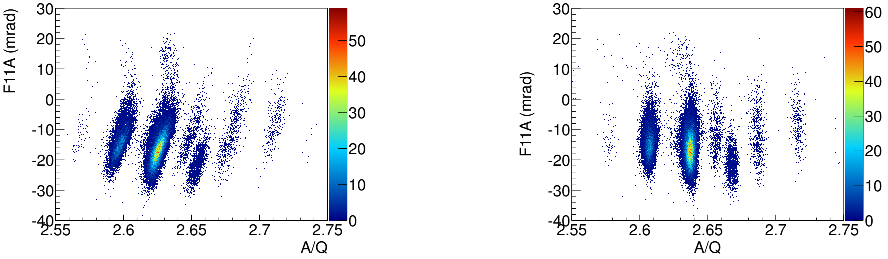

(c) Without A/Q corrections.

(d) A/Q corrections implemented.

Figure A.3.: Impact of the A/Q corrections demonstrated by correlations of A/Q and the reconstructed positions (X) and angles (A) at the focal point F11 of ZeroDegree. Panel a) and c) show uncorrected data while b) and d) depict the impact of the correction. See section 5.1.4 for more details.

A.2 MINOS calibration

For a proper functionality of the MINOS system the drift velocity v_{drift} has to be monitored run by run, as described in section 5.2. The obtained v_{drift} for setting 2 is shown in figure A.4.

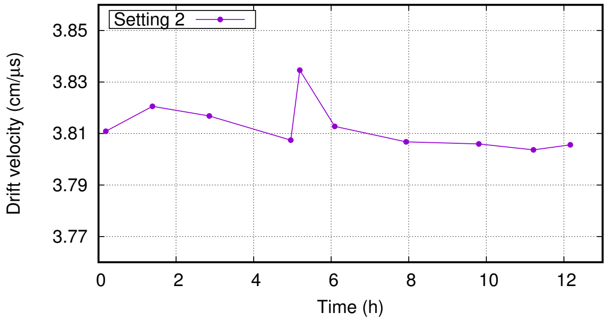

Figure A.4.: Behavior of the obtained drift velocities v_{drift} for setting 2. The presented time corresponds to the elapsed time after the start of the experiment. For each run the drift velocity is shown at the temporal middle of the run. See section 5.2 for more details.

A.3 DALI2 calibration

To evaluate the quality of the DALI2 calibration, the residues of the measured and tabulated energy of a transition is introduced in section 5.3. These residues are shown for the γ-ray transitions of 1173.23 keV and 1332.49 keV after the ^{60}Co decay in figures A.5 and A.6. Figures A.7 and A.8 show the residues for the γ-ray transitions at 898.04 keV and 1836.06 keV after the ^{88}Y decay.

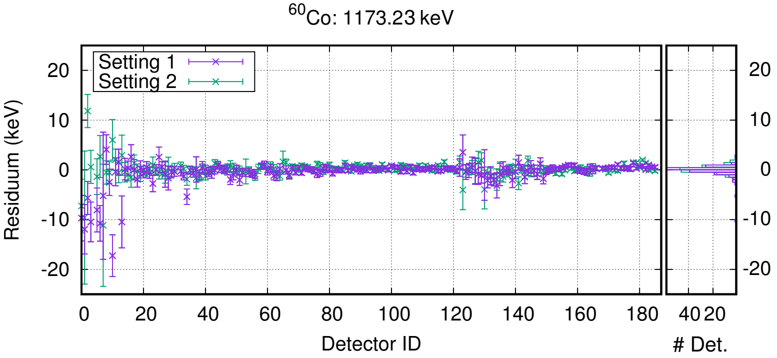

Figure A.5.: Residues of the 1173.23 keV transition after the ^{60}Co decay, defined as energy difference of the measured and tabulated energy for each detector (left) and the projected residues for all detectors (right). The calibration before setting 1 (2) is shown in purple (green).

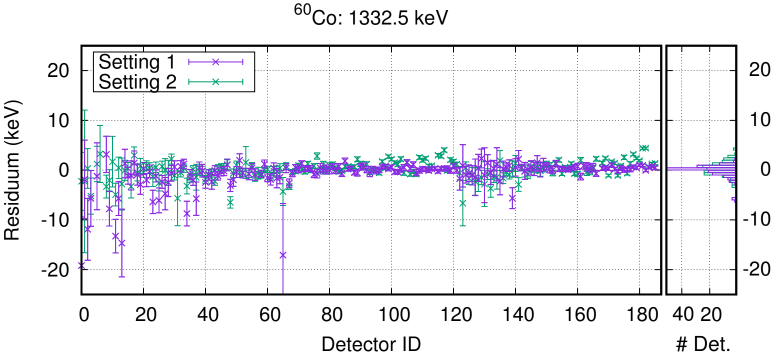

Figure A.6.: Residues of the 1332.49 keV transition after the ^{60}Co decay. Further information is given in the caption of figure A.5.

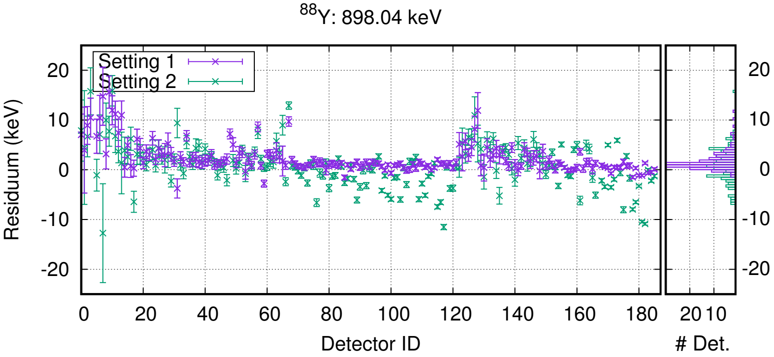

Figure A.7.: Residues of the 898.04 keV transition after the ^{88}Y decay. Further information is given in the caption of figure A.5.

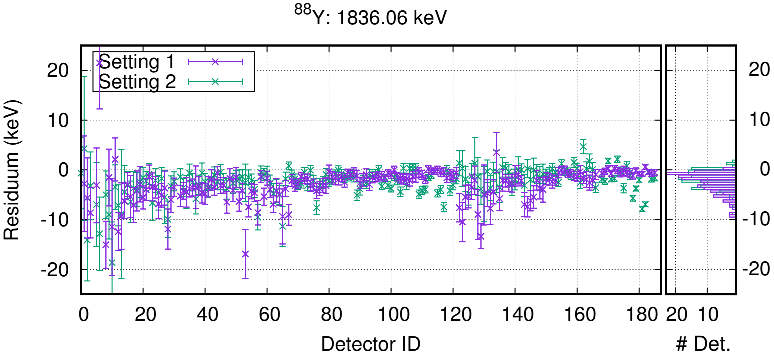

Figure A.8.: Residues of the 1836.06 keV transition after the ^{88}Y decay. Further information is given in the caption of figure A.5.

The resolution (σ) of all DALI2 detectors obtained from an analysis of the calibration run before setting 2 is shown in figure A.9. See section 5.3 for more information.

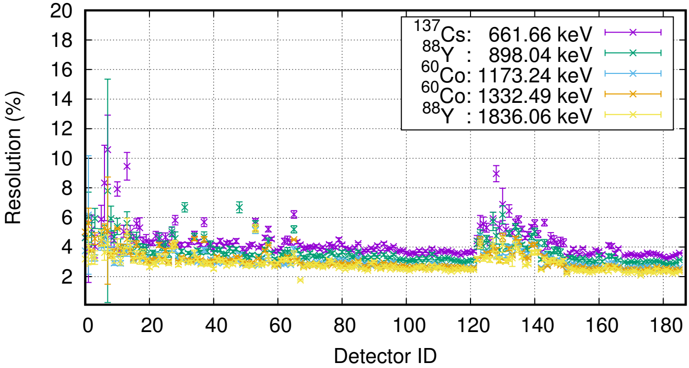

Figure A.9.: σ resolution of DALI2 in percent for different transition energies. The picture shows data from the calibration before setting 2.

A.4 Doppler-correction - Material along the beam line

Table A.1.: Material placed along the beam line, which is used for a LISE++ calculation. The measured velocity β_{57} in BigRIPS corresponds to the velocity measured after the F5 degrader, while β_{89}, measured in ZeroDegree, corresponds to the velocity before the F9PPAC1 [87]. Compare section 5.4 for further information.

Description	Material	Thickness
F5 degrader	Al	2 mm
F5PPAC2	$H_8C_{10}O_4$	45 μm
F7PPAC1	$H_8C_{10}O_4$	45 μm
F7IC[1] Window	$C_{22}H_{10}N_2O_4$	125 μm
F7IC[1] Gas	$H_8C_2Ar_{90}$	586 mm
F7IC[1] Electrodes	$H_8C_{10}O_4$	100 μm
F7IC[1] Window	$C_{22}H_{10}N_2O_4$	125 μm
F7PPAC2	$H_8C_{10}O_4$	45 μm
F7 Scintillator	$H_{10}C_9$	200 μm
F8PPAC1	$H_8C_{10}O_4$	45 μm
F8 Scintillator	$H_{10}C_9$	100 μm
F8PPAC2	$H_8C_{10}O_4$	45 μm
Kapton Window	$C_{22}H_{10}N_2O_4$	125 μm
Al foil	Al	12 μm
Air	$O_{23}N_{76}Ar$	300 mm
Entrance window	$C_{22}H_{10}N_2O_4$	260 μm
MINOS target	H	99 mm
Exit window	$C_{22}H_{10}N_2O_4$	300 μm
Air	$O_{23}N_{76}Ar$	800 mm
Al foil	Al	12 μm
F9PPAC1	$H_8C_{10}O_4$	45 μm

[1] Ionization chamber

A.5 Half-life dependent uncertainty - χ^2 distributions

A.5.1 ^{85}Ge (p, pn) ^{84}Ge

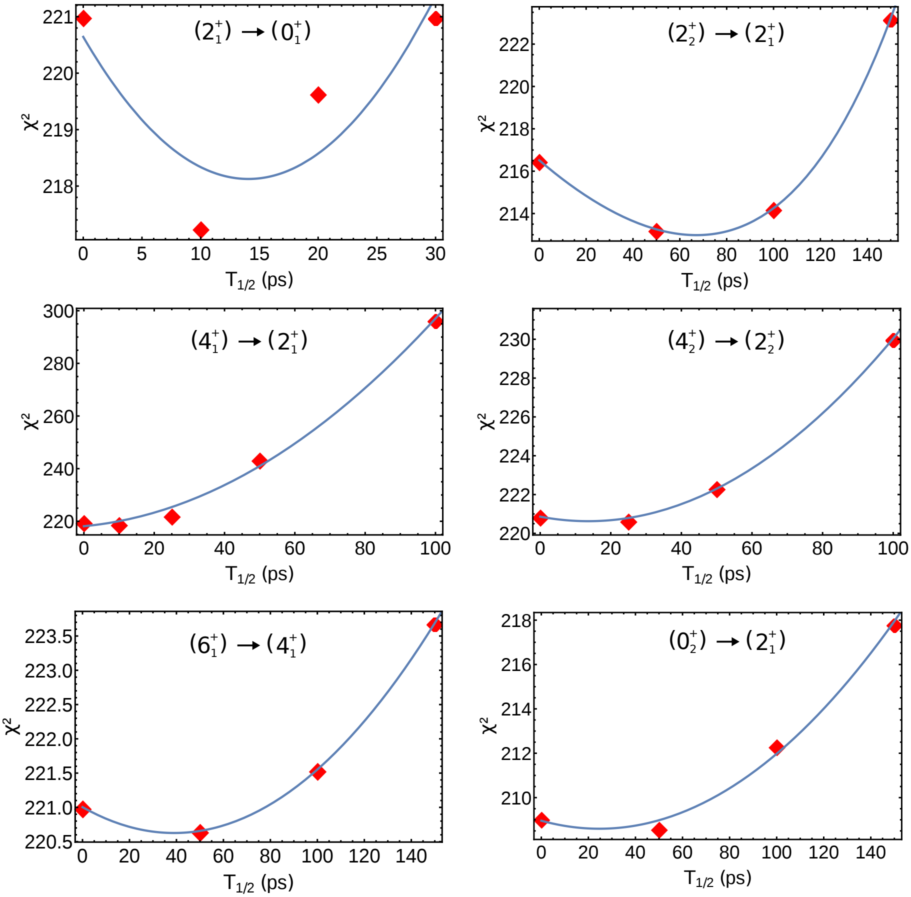

Figure A.10.: Evolution of χ^2 for different simulated level half-lifes $T_{1/2}$. The transition energy corresponds to the labeled decays of ^{84}Ge. The data points are fitted by a second order polynomial function. See section 5.8 for more information.

A.5.2 ^{87}As $(p,2p)$ ^{86}Ge

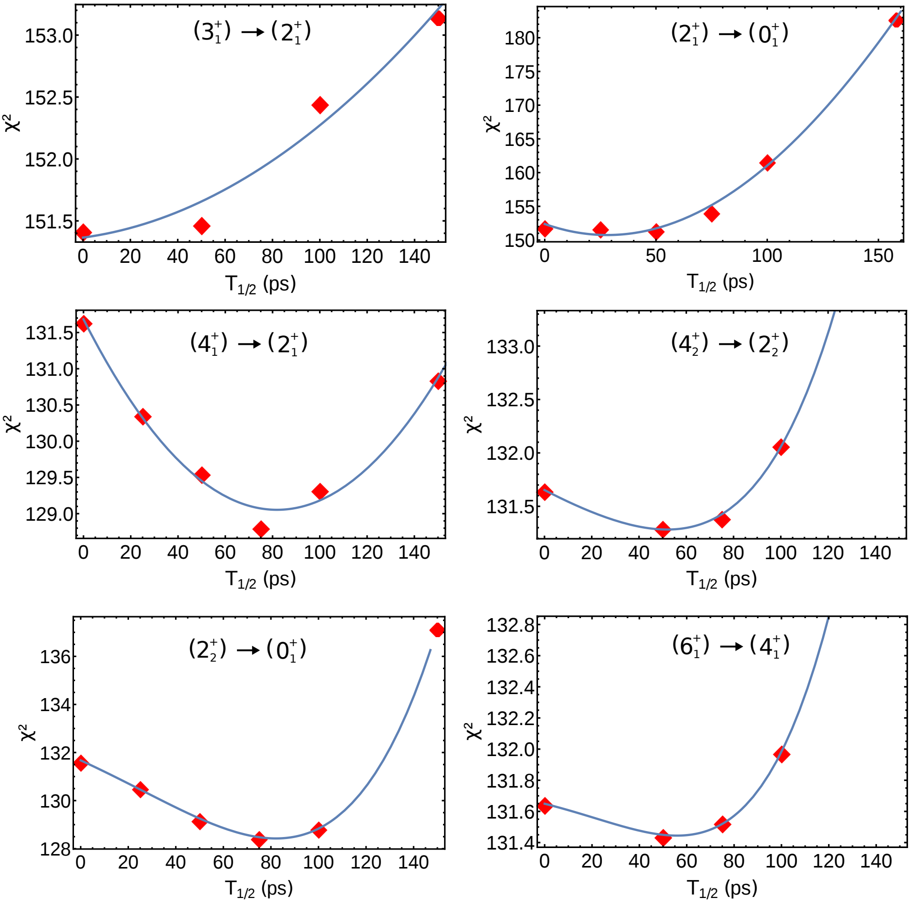

Figure A.11.: Evolution of χ^2 for different simulated level half-lifes $T_{1/2}$. The transition energy corresponds to the labeled decays of ^{86}Ge. The data points are fitted by a second order polynomial function. See section 5.8 for more information.

A.5.3 ^{89}As $(p, 2p)$ ^{88}Ge

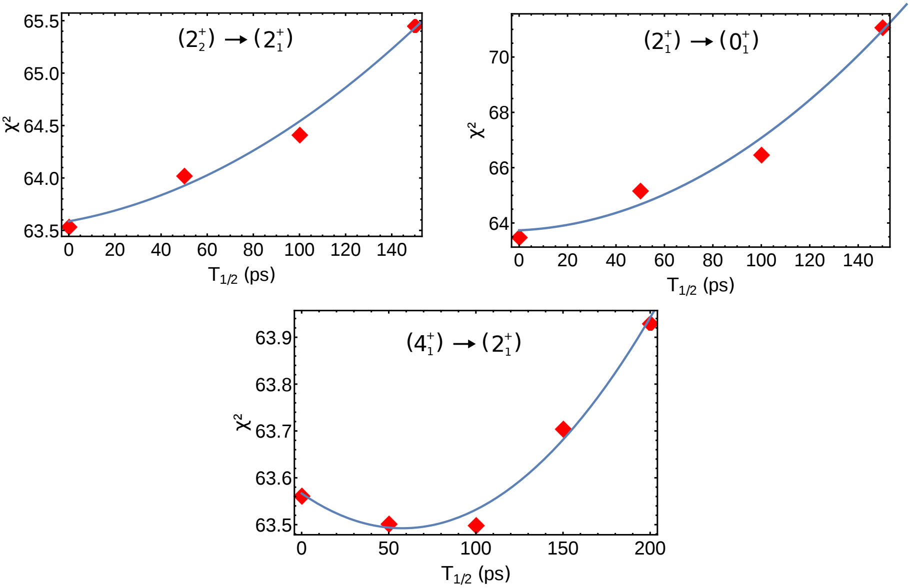

Figure A.12.: Evolution of χ^2 for different simulated level half-lifes $T_{1/2}$. The transition energy corresponds to the labeled decays of ^{88}Ge. The data points are fitted by a second order polynomial function. See section 5.8 for more information.

A.5.4 ^{84}Ge (p,p') ^{84}Ge

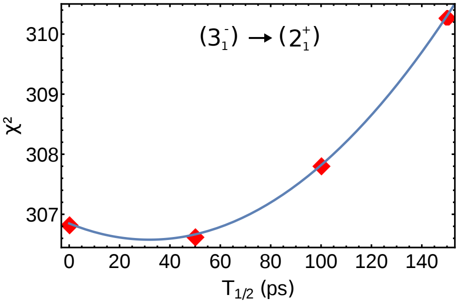

Figure A.13.: Evolution of χ^2 for different simulated level half-lifes $T_{1/2}$. The transition energy corresponds to the labeled decays of ^{84}Ge. The data points are fitted by a second order polynomial function. See section 5.8 for more information.

A.5.5 ^{86}Ge (p,p') ^{86}Ge

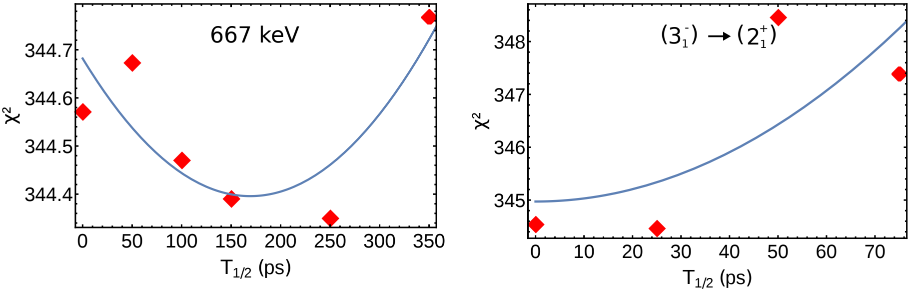

Figure A.14.: Evolution of χ^2 for different simulated level half-lifes $T_{1/2}$. The transition energy of the $(3^-_1) \rightarrow (2^+_1)$ decay of ^{86}Ge is applied in the figure on the right. The γ-ray transition energy of 667 keV is unassigned, hence it is labeled by its energy. The data points are fitted by a second order polynomial function. See section 5.8 for more information.

A.5.6 ^{94}Kr (p, p') ^{94}Kr

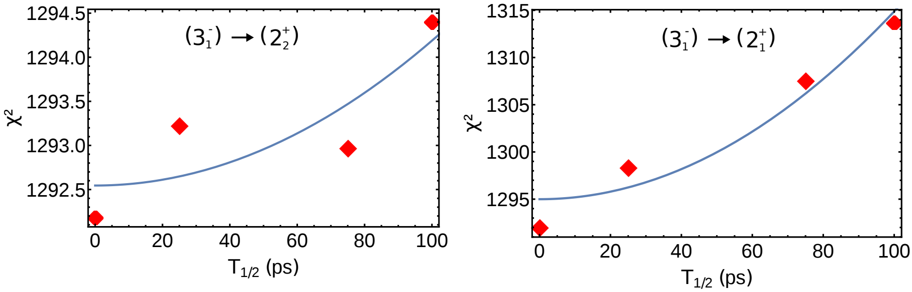

Figure A.15.: Evolution of χ^2 for different simulated level half-lifes $T_{1/2}$. The transition energy corresponds to the labeled decays of ^{94}Kr. The data points are fitted by a second order polynomial function. See section 5.8 for more information.

A.5.7 ^{96}Kr (p, p') ^{96}Kr

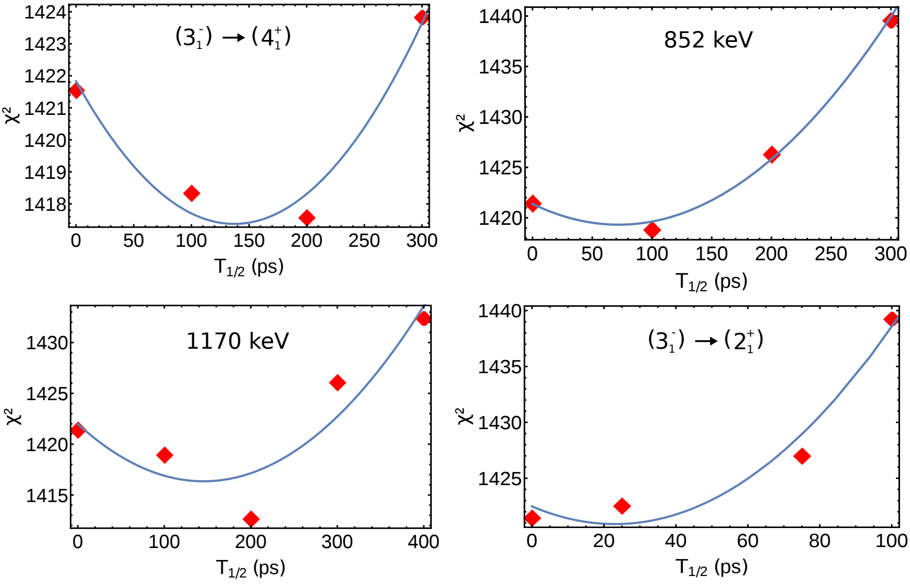

Figure A.16.: Evolution of χ^2 for different simulated level half-lifes $T_{1/2}$. The transition energy corresponds to the labeled decays of ^{96}Kr. In case the transition is unassigned, the figure is labeled by the observed energy. The data points are fitted by a second order polynomial function. See section 5.8 for more information.

A.6 Discarded DALI2 events within the p, p' analysis

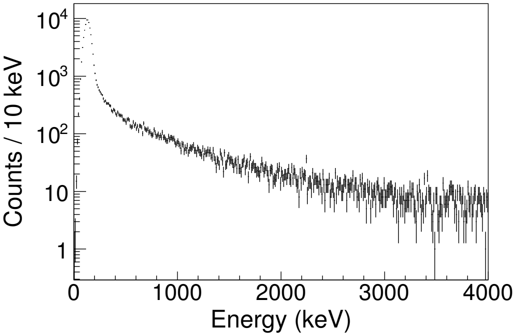

Figure A.17.: Discarded DALI2 events after the reaction ^{84}Ge$(p, p')^{84}$Ge. The spectrum shows the difference of DALI2 events with and without a DALI2 time condition of ± 10 ns. In addition, a DALI2 ID of $53 - 186$ is requested in both cases.

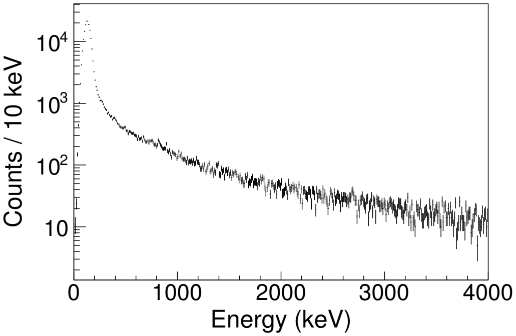

Figure A.18.: Discarded DALI2 events after the reaction ^{86}Ge$(p, p')^{86}$Ge. More details are given in the caption of figure A.17.

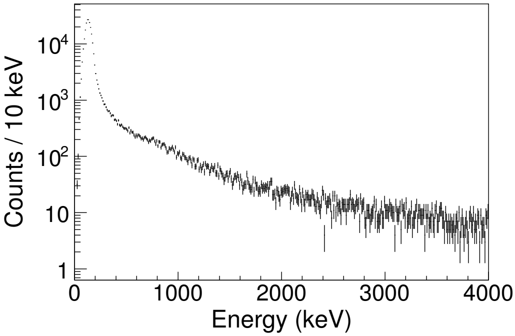

Figure A.19.: Discarded DALI2 events after the reaction ^{94}Kr$(p,p')^{94}$Kr. More details are given in the caption of figure A.17.

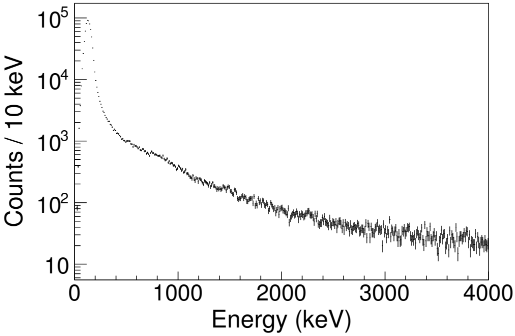

Figure A.20.: Discarded DALI2 events after the reaction ^{96}Kr$(p,p')^{96}$Kr. More details are given in the caption of figure A.17.

B Supplementary data for the results

B.1 Additional DALI2 spectra with different multiplicities

B.1.1 ^{85}Ge (p,pn) ^{84}Ge

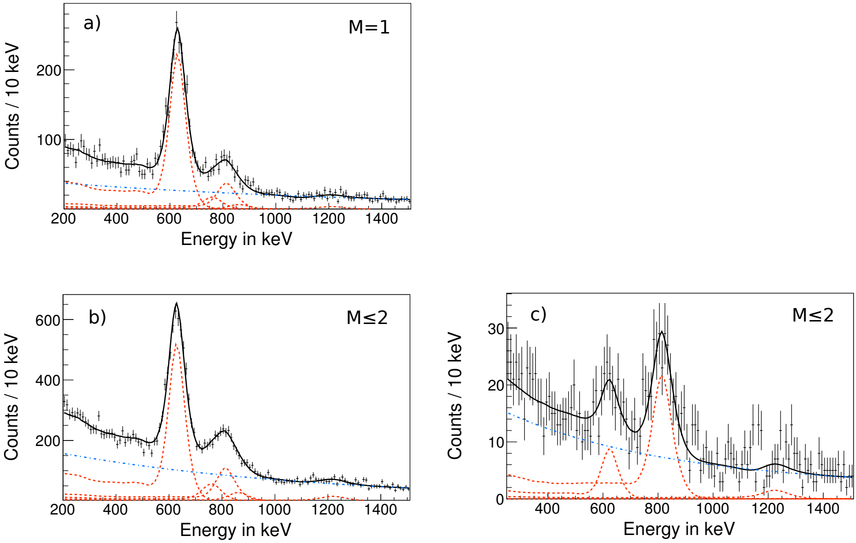

Figure B.1.: Figure a) and b) show a Doppler-corrected DALI2 spectrum after the reaction $^{85}\mathrm{Ge}(p,pn)^{84}\mathrm{Ge}$, while figure c) depicts a gate on the region of the 2_1^+ transition energy. M denotes the multiplicity cutoff.

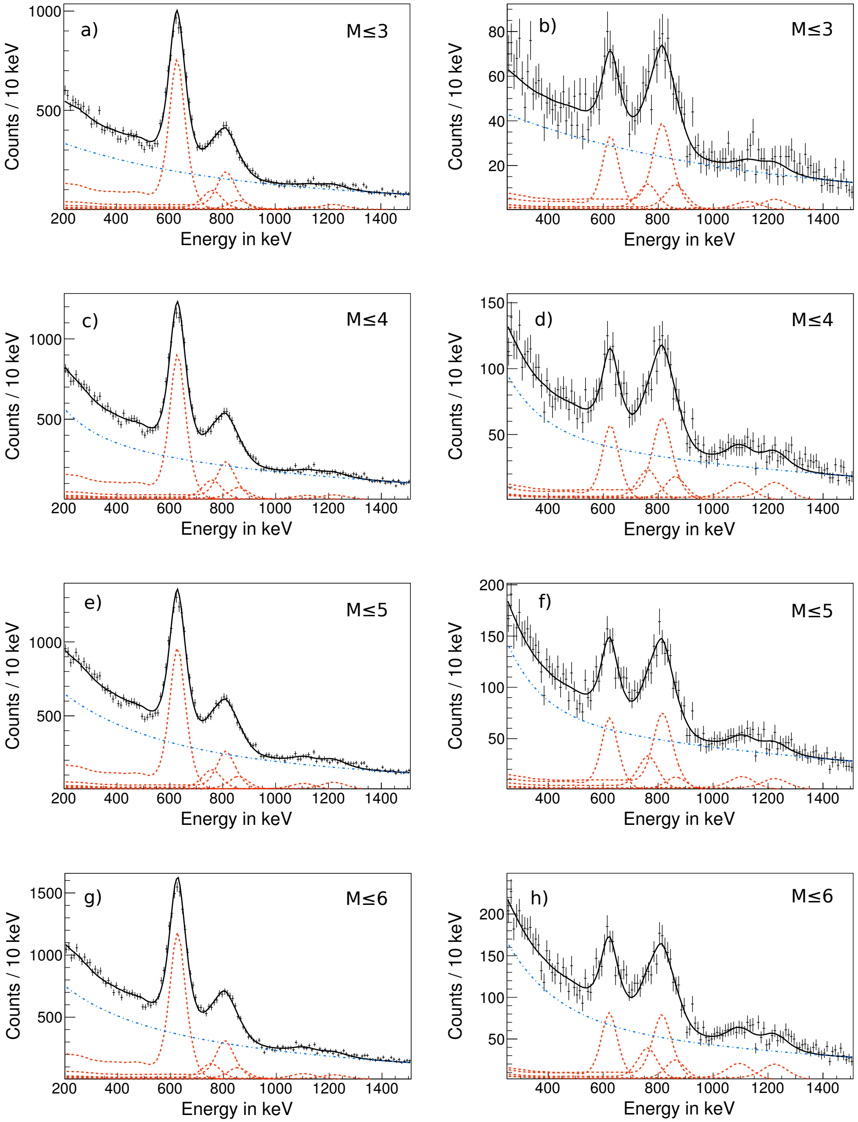

Figure B.2.: Figure a), c), e) and g) show a Doppler-corrected DALI2 spectrum after the reaction ^{85}Ge$(p, pn)^{84}$Ge, while figure b), d), f) and h) depict a gate on the region of the 2_1^+ transition energy. M denotes the multiplicity cutoff.

B.1.2 ^{86}As $(p,2pn)$ ^{84}Ge

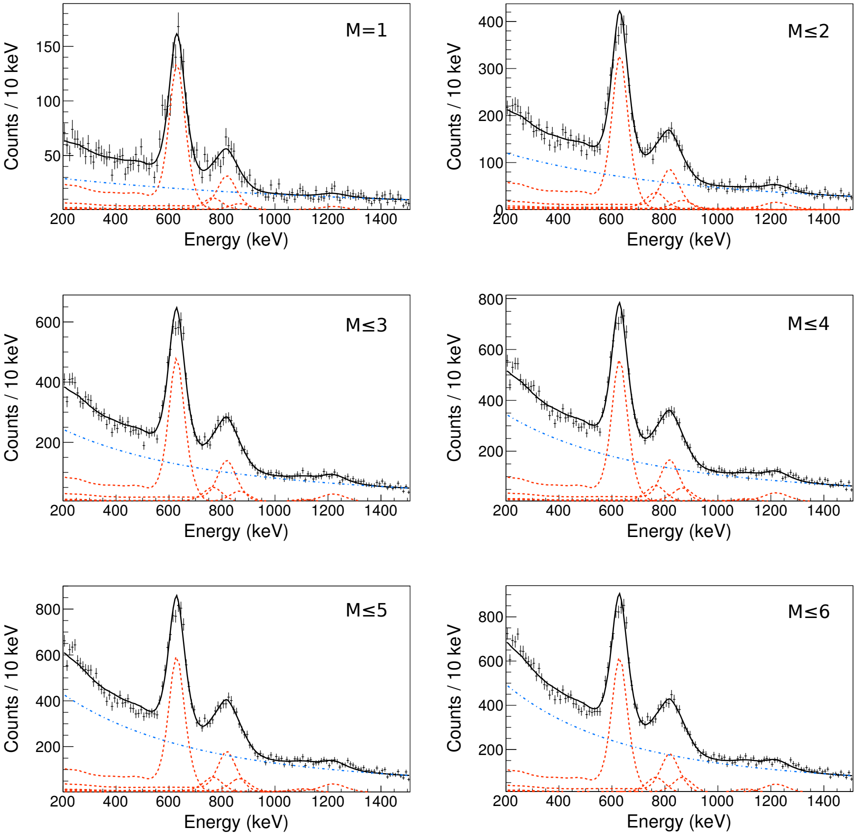

Figure B.3.: Doppler-corrected DALI2 spectra after the reaction ^{86}As$(p,pn)^{84}$Ge with different multiplicity (M) cutoffs.

B.1.3 ^{87}As $(p,2p2n)$ ^{84}Ge

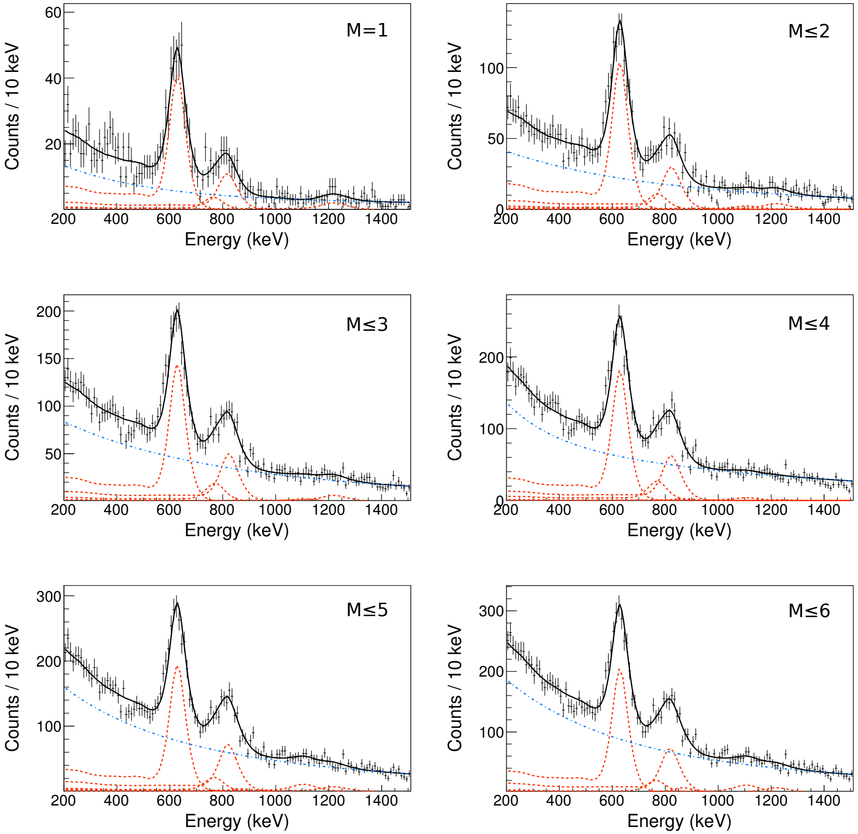

Figure B.4.: Doppler-corrected DALI2 spectra after the reaction ^{87}As$(p,pn)^{84}$Ge with different multiplicity (M) cutoffs.

B.1.4 ^{87}As $(p, 2p)$ ^{86}Ge

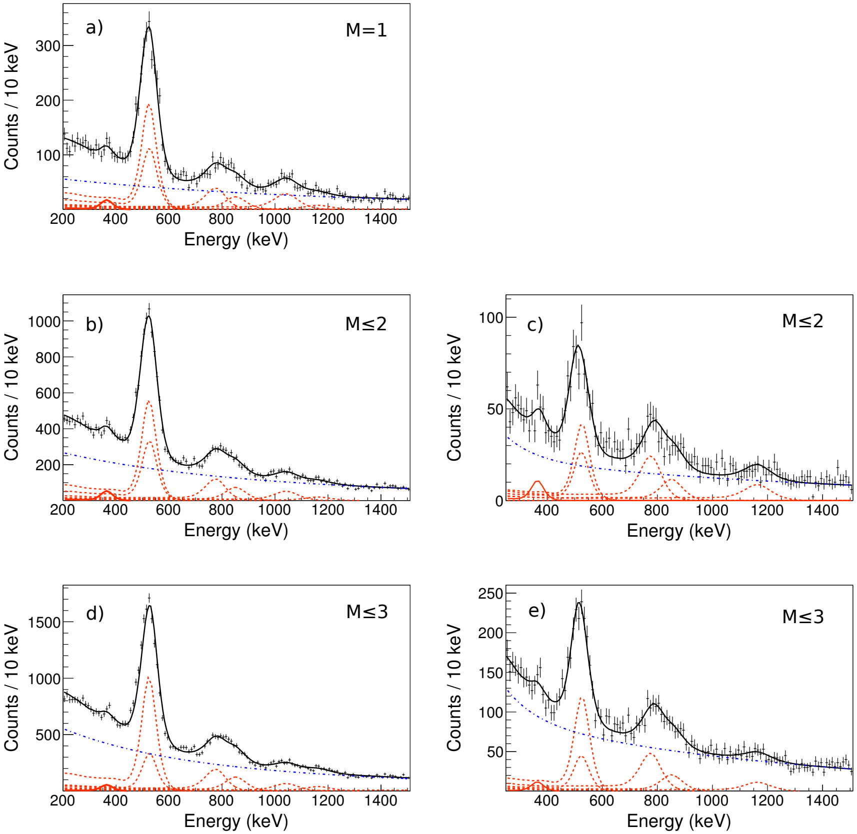

Figure B.5.: Figure a), b) and d) show a Doppler-corrected DALI2 spectrum after the reaction ^{87}As$(p, 2p)^{86}$Ge, while figure c) and e) depict a gate on the region of the 2_1^+ transition energy. M denotes the multiplicity cutoff.

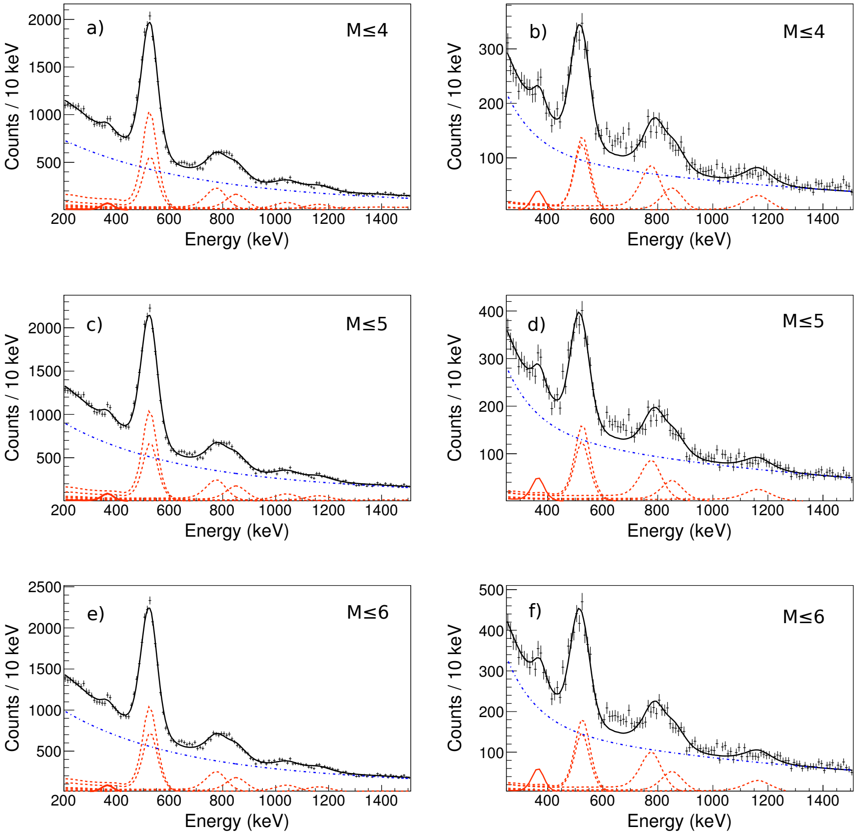

Figure B.6.: Figure a), c) and e) show a Doppler-corrected DALI2 spectrum after the reaction ^{87}As$(p,2p)^{86}$Ge, while figure b), d) and f) depict a gate on the region of the 2_1^+ transition energy. M denotes the multiplicity cutoff.

B.1.5 ^{89}As $(p,2p)$ ^{88}Ge

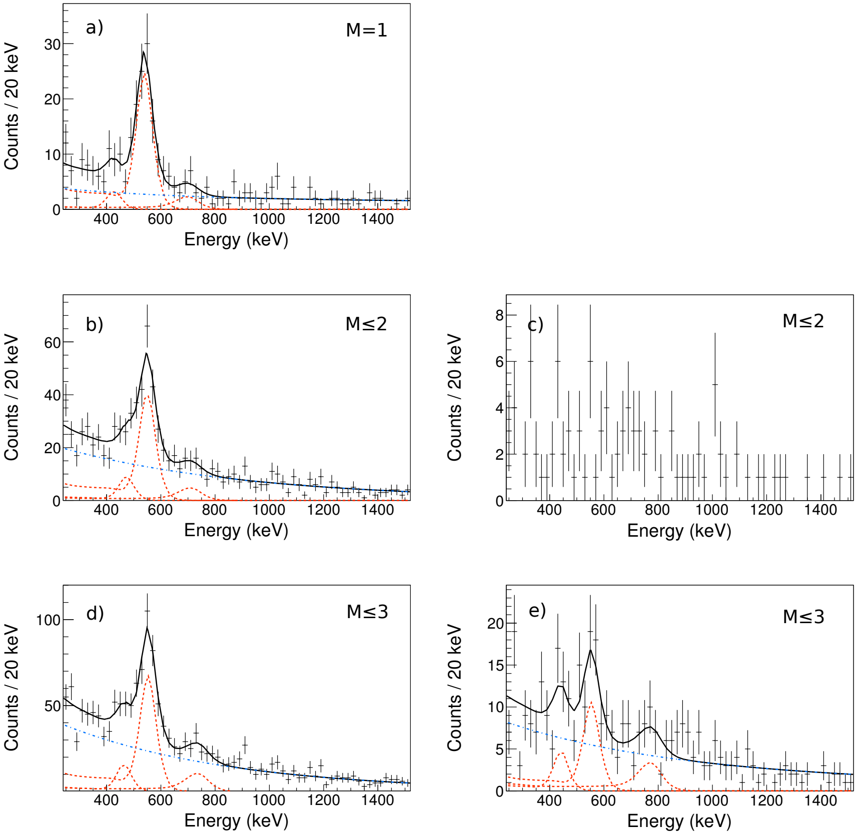

Figure B.7.: Figure a), b) and d) show a Doppler-corrected DALI2 spectrum after the reaction ^{89}As$(p,2p)^{88}$Ge, while figure c) and e) depict a gate on the region of the 2_1^+ transition energy. M denotes the multiplicity cutoff.

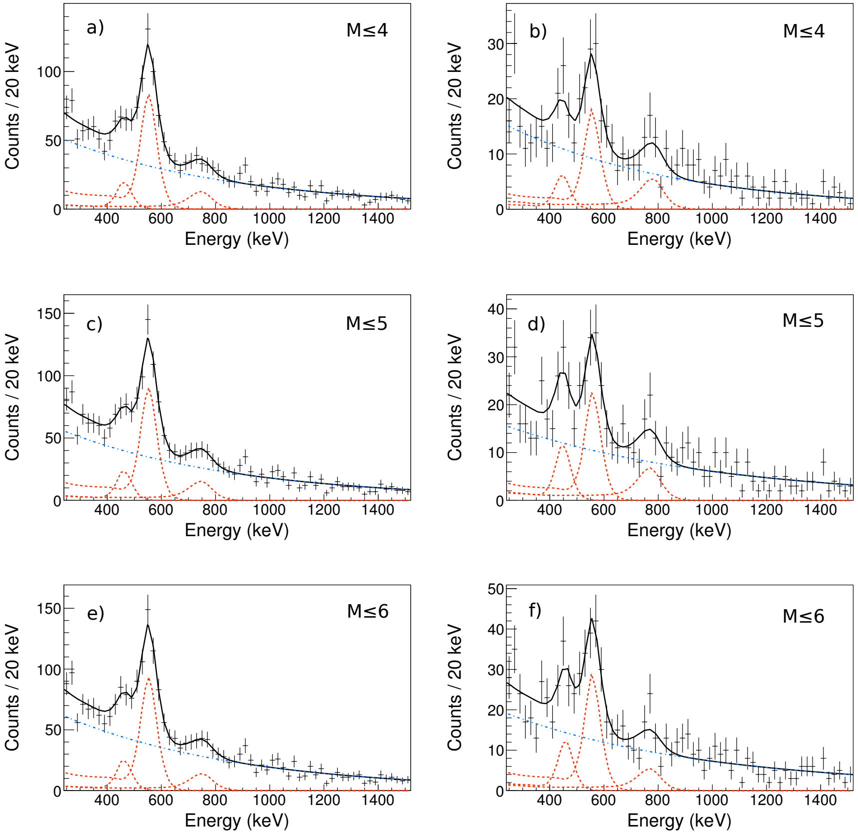

Figure B.8.: Figure a), c) and e) show a Doppler-corrected DALI2 spectrum after the reaction ^{89}As$(p,2p)^{88}$Ge, while figure b), d) and f) depict a gate on the region of the 2_1^+ transition energy. M denotes the multiplicity cutoff.

C Supplementary data for the discussion

C.1 Example of an ECIS-97 input file

```
84Ge, 248MeV/u, KD02                                         card 1
FFFFFtFtFFttttFtFFtFFFFFtFFtFFFFFFFFFFFFFFFFFFFFFF                     card 2
FFFFFFFFFFFFFFFFFFFFFFFFFFFFFFFFFFFFFFFFFFFFFFFFFF                     card 3
    2 20000                                                            card 4
       0.1    100.0                                                    card 5
0.       +   248.1       0.5        1.0      84.0       32.0          nuclear state (g.s)
    0                                                                  number of phonons
2.       +    0.624                                                    nuclear state (2+)
    1    1                                                             number of phonons
    2    0   2.0                                                      phonon description
10.736366  1.211333  0.66530919                                        real volume
14.084413  1.211333  0.66530919                                        im volume
                                                                       real surface
0.0757206  1.2729846 0.5624220                                         im surface
2.2240880  1.0376669 0.5900000                                         real s.o.
                                                                       im s.o.
1.2424046  0.6000000                                                   Coulomb
                                                                       s.o. Coulomb
1.0       10.0       180.
FIN
```

Figure C.1.: ECIS-97 input file for ^{84}Ge.

C.2 Calculation of the deformation length

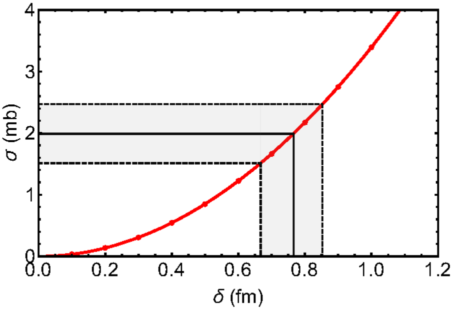

Figure C.2.: Model dependent correlation of the deformation length and the (p,p') cross section of the 2_1^+ state for ^{86}Ge. The red function shows the cross section for different δ obtained by an ECIS-97 calculation. The horizontal line defines the maximal, measured cross section. Using the red function obtained from the ECIS-97 calculation the cross section can be projected to a corresponding range of δ.

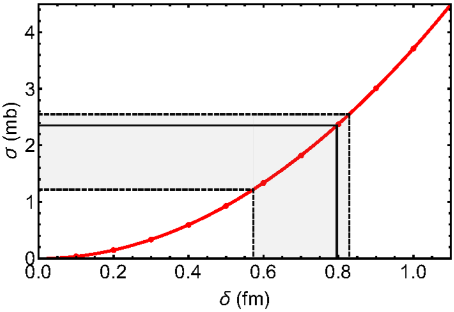

Figure C.3.: Model dependent correlation of the deformation length and the (p,p') cross section of the 2_1^+ state for ^{94}Kr. The red function shows the cross section for different δ obtained by an ECIS-97 calculation. The horizontal lines define the measured cross section with its uncertainties. Using the red function obtained from the ECIS-97 calculation the cross section can be projected to a corresponding range of δ.

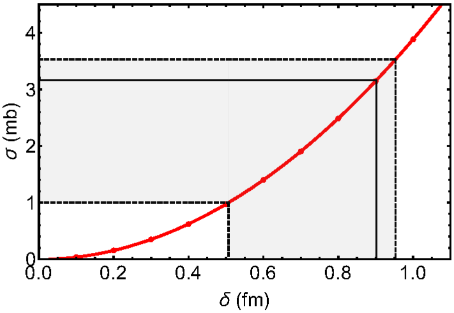

Figure C.4.: Model dependent correlation of the deformation length and the (p,p') cross section of the 2_1^+ state for ^{96}Kr. The red function shows the cross section for different δ obtained by an ECIS-97 calculation. The horizontal lines define the measured cross section with its uncertainties. Using the red function obtained from the ECIS-97 calculation the cross section can be projected to a corresponding range of δ.

Bibliography

[1] E. Rutherford. *LXXIX. The scattering of α and β particles by matter and the structure of the atom*. In: *The London, Edinburgh, and Dublin Philosophical Magazine and Journal of Science* 21.125 (1911), pp. 669–688.

[2] W. Marciano and H. Pagels. *Quantum chromodynamics*. In: *Nature* 279 (1979), 479–483.

[3] S.R. Beane et al. *Nuclear physics from lattice QCD*. In: *Progress in Particle and Nuclear Physics* 66.1 (2011), pp. 1 –40.

[4] R. Machleidt and D.R. Entem. *Chiral effective field theory and nuclear forces*. In: *Physics Reports* 503.1 (2011), pp. 1 –75.

[5] R. Machleidt. *High-precision, charge-dependent Bonn nucleon-nucleon potential*. In: *Phys. Rev. C* 63 (2001), p. 024001.

[6] V. G. J. Stoks et al. *Construction of high-quality NN potential models*. In: *Phys. Rev. C* 49 (1994), pp. 2950–2962.

[7] E. Epelbaum et al. *Ab Initio Calculation of the Spectrum and Structure of* ^{16}O. In: *Phys. Rev. Lett.* 112 (2014), p. 102501.

[8] S.K. Bogner, R.J. Furnstahl, and A. Schwenk. *From low-momentum interactions to nuclear structure*. In: *Progress in Particle and Nuclear Physics* 65.1 (2010), pp. 94 –147.

[9] R. Roth and P. Navrátil. *Ab Initio Study of* ^{40}Ca *with an Importance-Truncated No-Core Shell Model*. In: *Phys. Rev. Lett.* 99 (2007), p. 092501.

[10] S. Binder et al. *Ab initio path to heavy nuclei*. In: *Physics Letters B* 736.Supplement C (2014), pp. 119 –123.

[11] T. Otsuka et al. *Monte Carlo shell model for atomic nuclei*. In: *Progress in Particle and Nuclear Physics* 47.1 (2001), pp. 319 –400.

[12] C.A. Bertulani and V.Yu. Ponomarev. *Microscopic studies on two-phonon giant resonances*. In: *Physics Reports* 321.4 (1999), pp. 139 –251.

[13] M. Bender, P.-H. Heenen, and P.-G. Reinhard. *Self-consistent mean-field models for nuclear structure*. In: *Rev. Mod. Phys.* 75 (2003), pp. 121–180.

[14] A. Bohr and B. R. Mottelson. *Nuclear Structure*. Advanced Book Program, W. A., 1975.

[15] A. S. Davydov and G. F. Filippov. *Collective Excitations of Even-Even Nuclei*. In: *Soviet Physics JETP* 6 (1957).

[16] F. Iachello and A. Arima. *The interacting boson model*. Cambridge University Press, 1987.

[17] N. Pietralla, P. von Brentano, and A.F. Lisetskiy. *Experiments on multiphonon states with proton–neutron mixed symmetry in vibrational nuclei*. In: *Progress in Particle and Nuclear Physics* 60.1 (2008), pp. 225 –282.

[18] *National Nuclear Data Center*. `https://www.nndc.bnl.gov/chart/` Accessed: 2017-12-03.

[19] M. Goeppert-Mayer. *On Closed Shells in Nuclei. II*. In: *Phys. Rev.* 75 (1949), pp. 1969–1970.

[20] O. Haxel, J. H. D. Jensen, and H. E. Suess. *On the "Magic Numbers" in Nuclear Structure*. In: *Phys. Rev.* 75 (1949), pp. 1766–1766.

[21] P. Doornenbal and A. Obertelli. *Shell Evolution and Systematic Search for* 2_1^+ *Energies, Proposal for Nuclear Physics Experiment at RI Beam Factory, RIBF NP-PAC*-13. 2013.

[22] R. F. Casten. *NpNn systematics in heavy nuclei*. In: *Nuclear Physics A* 443.1 (1985), pp. 1 –28.

[23] R. F. Casten and N. V. Zamfir. *The evolution of nuclear structure: the* N_pN_n *scheme and related correlations*. In: *Journal of Physics G: Nuclear and Particle Physics* 22.11 (1996), p. 1521.

[24] E. Browne. In: *Nuclear Data Sheets* 82 (1997), p. 379.

[25] C. M. Baglin. In: *Nuclear Data Sheets* 113 (2012), p. 2187.

[26] D. Abriola and A. A. Sonzogni. In: *Nuclear Data Sheets* 107 (2006), p. 2423.

[27] D. Abriola and A. A. Sonzogni. In: *Nuclear Data Sheets* 109 (2008), p. 2501.

[28] B. Singh and Z. Hu. In: *Nuclear Data Sheets* 98 (2003), p. 335.

[29] B. Singh. In: *Nuclear Data Sheets* 109 (2008), p. 297.

[30] E. A. Mccutchan and A. A. Sonzogni. In: *Nuclear Data Sheets* 115 (2014), p. 135.

[31] A. Negret and B. Singh. In: *Nuclear Data Sheets* 124 (2015), p. 1.

[32] M. Albers et al. *Evidence for a Smooth Onset of Deformation in the Neutron-Rich Kr Isotopes*. In: *Phys. Rev. Lett.* 108 (2012), p. 062701.

[33] A. A. Sonzogni, M. Fadil, and B. Pfeiffer. In: *Nuclear Data Sheets* 110 (2009), p. 2815.

[34] J. K. Tuli. In: *Nuclear Data Sheets* 98 (2003), p. 209.

[35] M. Lebois et al. *Experimental study of ^{84}Ga β decay: Evidence for a rapid onset of collectivity in the vicinity of ^{78}Ni*. In: *Phys. Rev. C* 80 (2009), 044308(R).

[36] S. F. Shen et al. *Stability of triaxial shapes in ground and excited states of even-even nuclei in A 70 region*. In: *Phys. Rev. C* 84 (2011), 044315(R).

[37] D. L. Zhang and B. G. Ding. *Description of the rigid triaxial deformation at low energy in ^{76}Ge with the proton-neutron interacting model IBM2*. In: *Chin. Phys. Lett.* 30.12 (2013), 122101(R).

[38] J. J. Sun et al. *Spectroscopy of ^{74}Ge: From soft to rigid triaxiality*. In: *Phys. Lett. B* 734 (2014), pp. 308–313.

[39] T. Nikšić, P. Marević, and D. Vretenar. *Microscopic analysis of shape evolution and triaxiality in germanium isotopes*. In: *Phys. Rev. C* 89 (2014), p. 044325.

[40] A. S. Davydov and G. F. Filippov. *Rotational States in Even Atomic Nuclei*. In: *Nuclear Physics* 8 (1958), pp. 237–249.

[41] L. Wilets and M. Jean. *Surface Oscillations in Even-Even Nuclei*. In: *Phys. Rev.* 102 (1956), pp. 788–796.

[42] S. W. Ødegård et al. *Evidence for the Wobbling Mode in Nuclei*. In: *Phys. Rev. Lett.* 86 (2001), pp. 5866–5869.

[43] D. J. Hartley et al. *Wobbling mode in* ^{167}Ta. In: *Phys. Rev. C* 80 (2009), p. 041304.

[44] G Schönwaßer et al. *One- and two-phonon wobbling excitations in triaxial ^{165}Lu*. In: *Physics Letters B* 552.1 (2003), pp. 9 –16.

[45] S. Frauendorf and Jie Meng. *Tilted rotation of triaxial nuclei*. In: *Nuclear Physics A* 617.2 (1997), pp. 131 –147.

[46] T. Koike, K. Starosta, and I. Hamamoto. *Chiral Bands, Dynamical Spontaneous Symmetry Breaking, and the Selection Rule for Electromagnetic Transitions in the Chiral Geometry*. In: *Phys. Rev. Lett.* 93 (2004), p. 172502.

[47] K. Starosta et al. *Chirality in odd–odd triaxial nuclei*. In: *Nuclear Physics A* 682.1 (2001), pp. 375 –386.

[48] J. A. Cizewski et al. *Evidence for a New Symmetry in Nuclei: The Structure of* ^{196}Pt *and the O(6) Limit*. In: *Phys. Rev. Lett.* 40 (1978), pp. 167–170.

[49] J. Jolie et al. *Test of the SO(6) selection rule in 196Pt using cold-neutron capture*. In: *Nuclear Physics A* 934.Supplement C (2015), pp. 1 –7.

[50] N. Pietralla et al. *New Information on the Occurrence of the O(6) Symmetry in Nuclei*. In: *EPJ Web of Conferences* 93 (2015), p. 01002.

[51] Y. Toh et al. *Evidence for rigid triaxial deformation at low energy in ^{76}Ge*. In: *Phys. Rev. C* 87 (2013), p. 041304.

[52] K. S. Krane. *Introductory Nuclear Physics*. John Wiley & Sons, 1988.

[53] K. Heyde. *Basic ideas and concepts in nuclear physics : an introductory*. Institute of Physics Publishing, 1994.

[54] J. S. Lilley. *Nuclear Physics: Principles and Applications*. Manchester Physics Series. Wiley, 2001.

[55] R. F. Casten. *Nuclear Structure from a Simple Perspective*. Oxford Studies in Nuclear Physics Series. Oxford University Press, 2005.

[56] T. Mayer-Kuckuk. *Kernphysik: Eine Einführung*. Teubner, 1984.

[57] K. Alder and A. Winther. *The Theory of Coulomb Excitation of Nuclei*. In: *Phys. Rev.* 91 (1953), pp. 1578–1579.

[58] B. V. Carlson. *Optical Model Calculations with the Code ECIS*95. In: *Lecture notes* (2000).

[59] K. S. Hodgson. *The Optical Model of Elastic Scattering*. Oxford University Press, 1963.

[60] K. S. Hodgson. *NUCLEAR REACTIONS AND NUCLEAR STRUCTURE*. Oxford University Press, 1971.

[61] K. S. Hodgson. *THE NUCLEON OPTICAL MODEL*. World Scientific Publishing Co. Pte. Ltd., 1994.

[62] P. E. Hodgson. *The Nuclear Optical Model Introductory Overview*. In: 1997.

[63] F. D. Becchetti and G. W. Greenlees. *Nucleon-Nucleus Optical-Model Parameters, $A > 40$, $E < 50$ MeV*. In: *Phys. Rev.* 182 (1969), pp. 1190–1209.

[64] A.J. Koning and J.P. Delaroche. *Local and global nucleon optical models from 1 keV to 200 MeV*. In: *Nuclear Physics A* 713.3 (2003), pp. 231 –310.

[65] V. F. Weisskopf. *Radiative Transition Probabilities in Nuclei*. In: *Phys. Rev.* 83 (1951), pp. 1073–1073.

[66] J. Suhonen. *From Nucleons to Nucleus: Concepts of Microscopic Nuclear Theory*. Springer: Theoretical and Mathematical Physics, 2007.

[67] A. M. Bernstein, V. R. Brown, and V. A. Madsen. *Neutron and proton transition matrix elements and inelastic hadron scattering*. In: *Physics Letters B* 103.4 (1981), pp. 255 –258.

[68] A. M. Bernstein, V. R. Brown, and V. A. Madsen. *Neutron and Proton Matrix Elements for Low-Lying* 2^+ *Transitions and the Probe Dependence of the Nuclear Deformation Parameter*. In: *Comments Nucl. Part. Phys.* 11.5 (1983), pp. 203–215.

[69] N. Alamanos and A. Gillibert. *Selected Topics in Reaction Studies with Exotic Nuclei*. In: *The Euroschool Lectures on Physics with Exotic Beams, Vol. I*. Ed. by Jim Al-Khalili and Ernst Roeckl. Berlin, Heidelberg: Springer Berlin Heidelberg, 2004, pp. 295–337.

[70] V. A. Madsen, V. R. Brown, and J. D. Anderson. *Differences of deformation parameter* β *for different transition mechanisms; comparison with data*. In: *Phys. Rev. C* 12 (1975), pp. 1205–1211.

[71] A. S. Davydov and V. S. Rostovsky. *Relative Transition Probabilities Between Rotational Levels of Non-Axial Nuclei*. In: *Nuclear Physics* 12 (1959), pp. 58–68.

[72] A. S. Davydov and A. A. Chaban. *Rotation-Vibration Interaction in Non-Axial Even Nuclei*. In: *Nuclear Physics* 20 (1960), pp. 499–508.

[73] A. S. Davydov and G. F. Filippov. *On the Shape of Even-Even Nuclei*. In: *Soviet Physics JETP* 36 (1958).

[74] A. S. Davydov and G. F. Filippov. *Rotational States of Nonaxial Nuclei*. In: *Soviet Physics JETP* 35 (1958).

[75] A. S. Davydov and W. S. Rostovsky. *Transition Probabilities Between the Levels of the Rotational Band of Non-Axial Nuclei*. In: *Soviet Physics JETP* 36 (1959).

[76] H.-J. Wollersheim. *Kernstruktur schnell rotierender Atomkerne*. Frankfurt: habilitation treatises, 2007.

[77] T. R. Rodríguez and J. L. Egido. *Triaxial angular momentum projection and configuration mixing calculations with the Gogny force*. In: *Phys. Rev. C* 81 (2010), p. 064323.

[78] K. Sieja et al. *Laboratory versus intrinsic description of nonaxial nuclei above doubly magic* ^{78}*Ni*. In: *Phys. Rev. C* 88 (2013), p. 034327.

[79] P. Ring and P. Schuck. *The Nuclear Many-Body Problem*. Springer Berlin Heidelberg, 2000.

[80] M. Anguiano, J.L Egido, and L.M Robledo. *Mean-field based approaches to pairing correlations in atomic nuclei*. In: *Physics Letters B* 545.1 (2002), pp. 62 –72.

[81] A. Arima et al. *Collective nuclear states as symmetric couplings of proton and neutron excitations*. In: *Physics Letters B* 66.3 (1977), pp. 205 –208.

[82] A. Obertelli et al. *MINOS: A vertex tracker coupled to a thick liquid-hydrogen target for in-beam spectroscopy of exotic nuclei*. In: *The European Physical Journal A* 50.1 (2014), p. 8.

[83] S. Takeuchi et al. *DALI2: A NaI(Tl) detector array for measurements of γ rays from fast nuclei*. In: *Nuclear Instruments and Methods in Physics Research Section A: Accelerators, Spectrometers, Detectors and Associated Equipment* 763 (2014), pp. 596 –603.

[84] T. Kubo et al. *BigRIPS separator and ZeroDegree spectrometer at RIKEN RI Beam Factory*. In: *Progress of Theoretical and Experimental Physics* 2012.1 (2012), p. 03C003.

[85] H. Okuno, N. Fukunishi, and O. Kamigaito. *Progress of RIBF accelerators*. In: *Progress of Theoretical and Experimental Physics* 2012.1 (2012), p. 03C002.

[86] H. Okuno et al. *Charge strippers for Radioisotope Beam Factory at RIKEN*. In: *Journal of Radioanalytical and Nuclear Chemistry* 299.2 (2014), pp. 945–949.

[87] N. Fukuda et al. *Identification and separation of radioactive isotope beams by the BigRIPS separator at the RIKEN RI Beam Factory*. In: *Nuclear Instruments and Methods in Physics Research Section B: Beam Interactions with Materials and Atoms* 317, Part B (2013), pp. 323 –332.

[88] H. Kumagai et al. *Development of Parallel Plate Avalanche Counter (PPAC) for BigRIPS fragment separator*. In: *Nuclear Instruments and Methods in Physics Research Section B: Beam Interactions with Materials and Atoms* 317, Part B (2013), pp. 717 –727.

[89] H. Kumagai et al. *Delay-line PPAC for high-energy light ions*. In: *Nuclear Instruments and Methods in Physics Research Section A: Accelerators, Spectrometers, Detectors and Associated Equipment* 470.3 (2001), pp. 562 –570.

[90] K. Kimura et al. *High-rate particle identification of high-energy heavy ions using a tilted electrode gas ionization chamber*. In: *Nuclear Instruments and Methods in Physics Research Section A: Accelerators, Spectrometers, Detectors and Associated Equipment* 538.1–3 (2005), pp. 608 –614.

[91] A. Obertelli et al. *MINOS : a H2 target and vertex-tracker device for in-beam gamma spectroscopy at relativistic energies*. In: *RIBF Construction Proposal NP112-RIBF95* (2011).

[92] C. Santamaria. *Quest for new nuclear magic numbers with MINOS*. PhD thesis. Université Paris-Sud XI, 2015.

[93] S. Takeuchi et al. *DALI2: A NaI(Tl) detector array for measurements of γ rays from fast nuclei*. In: *Nuclear Instruments and Methods in Physics Research Section A: Accelerators, Spectrometers, Detectors and Associated Equipment* 763 (2014), pp. 596 –603.

[94] M. L. Cortés Sua. *Inelastic scattering of Ni and Zn isotopes off a proton target*. PhD thesis. Technische Universität Darmstadt, 2016.

[95] C. M. Shand. *Shell Evolution Beyond $N = 50$ and $Z = 28$: Spectroscopy of $^{81,82,83,84}Zn$*. PhD thesis. University of Surrey, 2016.

[96] P.-A. Söderström et al. *Installation and commissioning of EURICA – Euroball-RIKEN Cluster Array*. In: *Nuclear Instruments and Methods in Physics Research Section B: Beam Interactions with Materials and Atoms* 317, Part B (2013), pp. 649 –652.

[97] Y. Giomataris et al. *MICROMEGAS: a high-granularity position-sensitive gaseous detector for high particle-flux environments*. In: *Nuclear Instruments and Methods in Physics Research Section A: Accelerators, Spectrometers, Detectors and Associated Equipment* 376.1 (1996), pp. 29 –35.

[98] I. Giomataris et al. *Micromegas in a bulk*. In: *Nuclear Instruments and Methods in Physics Research Section A: Accelerators, Spectrometers, Detectors and Associated Equipment* 560.2 (2006), pp. 405 –408.

[99] V. P. C. Hough. *Method and means for recognizing complex patterns*. In: *United States Patent Office* 3,069,654 (1962).

[100] S. Agostinelli et al. GEANT4 - *a simulation toolkit*. In: *Nuclear Instruments and Methods in Physics Research Section A* 506 (2003), pp. 250–303.

[101] K. Moschner. private communication. 2017.

[102] R. Grzywacz et al. *Identification of μs-isomers produced in the fragmentation of a ^{112}Sn beam*. In: *Physics Letters B* 355.3 (1995), pp. 439 –446.

[103] E. Browne and J. K. Tuli. In: *Nuclear Data Sheets* 108 (2007), p. 2173.

[104] E. Browne and J. K. Tuli. In: *Nuclear Data Sheets* 114 (2013), p. 1849.

[105] E.A. Mccutchan and A.A. Sonzogni. In: *Nuclear Data Sheets* 115 (2014), p. 135.

[106] W. R. Leo. *Techniques for Nuclear and Particle Physics Experiments*. Springer-Verlag, 1994.

[107] O. B. Tarasov and D. Bazin. *LISE++: Radioactive beam production with in-flight separators*. In: *Nuclear Instruments and Methods in Physics Research Section B: Beam Interactions with Materials and Atoms* 266.19 (2008), pp. 4657 –4664.

[108] P. Doornenbal. *Manual of a GEANT4 Simulation Code for γ-Ray Detectors used in the RIKEN-RIBF Facility*. `http://www.nishina.riken.jp/collaboration/SUNFLOWER/misc/download/stores/manual.pdf` Accessed: 2017-09-03.

[109] K. Weise et al. *Bayesian decision threshold, detection limit and confidence limits in ionising-radiation measurement*. In: *Radiation Protection Dosimetry* 121.1 (2006), pp. 52–63.

[110] A. Korgul et al. *Experimental study of the $\beta - \gamma$ and $\beta - n\gamma$ decay of the neutron-rich nucleus ^{85}Ga*. In: *Phys. Rev. C* 88 (2013), p. 044330.

[111] J. A. Winger et al. *New subshell closure at $N = 58$ emerging in neutron-rich nuclei beyond ^{78}Ni*. In: *Phys. Rev. C* 81 (2010), p. 044303.

[112] K. Kolos et al. *Probing nuclear structures in the vicinity of ^{78}Ni with $\beta-$ and $\beta n-$ decay spectroscopy of ^{84}Ga*. In: *Phys. Rev. C* 88 (2013), p. 047301.

[113] P. Doornenbal et al. *In-Beam γ-Ray Spectroscopy of $^{34,36,38}\mathrm{Mg}$: Merging the N=20 and N=28 Shell Quenching*. In: *Phys. Rev. Lett.* 111 (2013), p. 212502.

[114] H. Iwasaki et al. *Evolution of Collectivity in $^{72}\mathrm{Kr}$: Evidence for Rapid Shape Transition*. In: *Phys. Rev. Lett.* 112 (2014), p. 142502.

[115] D. Bazin et al. *New Direct Reaction: Two-Proton Knockout from Neutron-Rich Nuclei*. In: *Phys. Rev. Lett.* 91 (2003), p. 012501.

[116] P. Fallon et al. *Two-proton knockout from $^{32}\mathrm{Mg}$: Intruder amplitudes in $^{30}\mathrm{Ne}$ and implications for the binding of $^{29,31}\mathrm{F}$*. In: *Phys. Rev. C* 81 (2010), p. 041302.

[117] K. Miernik et al. *Large β-Delayed One and Two Neutron Emission Rates in the Decay of ^{86}Ga*. In: *Phys. Rev. Lett.* 111 (2013), p. 132502.

[118] S. Chen et al. *Low-lying structure and shape evolution in neutron-rich Se isotopes*. In: *Phys. Rev. C* 95 (2017), 041302(R).

[119] B. Singh. In: *Nuclear Data Sheets* 74,63 (1995).

[120] T. Rzaca-Urban et al. *Shapes of the neutron-rich* $^{88-94}$*Kr nuclei*. In: *The European Physical Journal A - Hadrons and Nuclei* 9.2 (2000), pp. 165–169.

[121] J. Dudouet et al. $^{96}_{36}\mathrm{Kr}_{60}$ *– Low-Z Boundary of the Island of Deformation at* $N = 60$. In: *Phys. Rev. Lett.* 118 (2017), p. 162501.

[122] T. Otsuka and N. Yoshida. *User's manual of the program NPBOS (JAERI-M–85-094)*. Japan. 1985.

[123] K. Sieja. private communication. 2017.

[124] T. R. Rodríguez. private communication. 2017.

[125] A. F. Lisetskiy et al. *New* $T = 1$ *effective interactions for the* $f_{5/2}\ p_{3/2}\ p_{1/2}\ g_{9/2}$ *model space: Implications for valence-mirror symmetry and seniority isomers*. In: *Phys. Rev. C* 70 (2004), p. 044314.

[126] E. Caurier et al. *Collectivity in the light xenon isotopes: A shell model study*. In: *Phys. Rev. C* 82 (2010), p. 064304.

[127] K. Sieja et al. *Description of proton-neutron mixed-symmetry states near* ^{132}Sn *within a realistic large scale shell model*. In: *Phys. Rev. C* 80 (2009), p. 054311.

[128] K. Sieja and F. Nowacki. *Three-body forces and persistence of spin-orbit shell gaps in medium-mass nuclei: Toward the doubly magic* ^{78}*Ni*. In: *Phys. Rev. C* 85 (2012), p. 051301.

[129] M. Lettmann et al. *Triaxiality of neutron-rich* ^{84,86,88}Ge *from low-energy nuclear spectra*. In: *Phys. Rev. C* 96 (2017), p. 011301.

[130] M. Borrajo, T. R. Rodríguez, and J. L. Egido. *Symmetry conserving configuration mixing method with cranked states*. In: *Physics Letters B* 746.Supplement C (2015), pp. 341 –346.

[131] N.V. Zamfir and R.F. Casten. *Signatures of* γ *softness or triaxiality in low energy nuclear spectra*. In: *Physics Letters B* 260.3 (1991), pp. 265 –270.

[132] E. Padilla-Rodal et al. $B(E2)\uparrow$ *Measurements for Radioactive Neutron-Rich Ge Isotopes: Reaching the* $N = 50$ *Closed Shell*. In: *Phys. Rev. Lett.* 94 (2005), p. 122501.

[133] T. Togashi et al. *Quantum Phase Transition in the Shape of Zr isotopes*. In: *Phys. Rev. Lett.* 117 (2016), p. 172502.

List of Figures

List of Tables

List of Publications

Publications in refereed journals

B. Alikhani, A. Givechev, A. Heinz, P.R. John, J. Leske, M. Lettmann, O. Möller, N. Pietralla, C. Röder.
Compton polarimetry with a 36-fold segmented HPGe-detector of the AGATA-type.
Nucl. Instr. Meth. A 675, 144 (2012).

C. Santamaria, C. Louchart, A. Obertelli, V. Werner, P. Doornenbal, F. Nowacki, G. Authelet, H. Baba, D. Calvet, F. Château, A. Corsi, A. Delbart, J.-M. Gheller, A. Gillibert, T. Isobe, V. Lapoux, M. Matsushita, S. Momiyama, T. Motobayashi, M. Niikura, H. Otsu, C. Péron, A. Peyaud, E. C. Pollacco, J.-Y. Roussé, H. Sakurai, M. Sasano, Y. Shiga, S. Takeuchi, R. Taniuchi, T. Uesaka, H. Wang, K. Yoneda, F. Browne, L. X. Chung, Zs. Dombradi, S. Franchoo, F. Giacoppo, A. Gottardo, K. Hadynska-Klek, Z. Korkulu, S. Koyama, Y. Kubota, J. Lee, M. Lettmann, R. Lozeva, K. Matsui, T. Miyazaki, S. Nishimura, L. Olivier, S. Ota, Z. Patel, N. Pietralla, E. Sahin, C. Shand, P.-A. Söderström, I. Stefan, D. Steppenbeck, T. Sumikama, D. Suzuki, Zs. Vajta, J. Wu, Z. Xu.
Extension of the $N = 40$ Island of Inversion towards $N = 50$: Spectroscopy of ^{66}Cr, ^{70,72}Fe.
Phys. Rev. Lett. 115, 192501 (2015)

Zs. Podolyák, C. M. Shand, N. Lalović, J. Gerl, D. Rudolph, T. Alexander, P. Boutachkov, M. L. Cortés, M. Górska, I. Kojouharov, N. Kurz, C. Louchart, E. Merchán, C. Michelagnoli, R. M. Pérez-Vidal, S. Pietri, D. Ralet, M. Reese, H. Schaffner, Ch. Stahl, H. Weick, F. Ameil, G. de Angelis, T. Arici, R. Carroll, Zs. Dombrádi, A. Gadea, P. Golubev, M. Lettmann, C. Lizarazo, D. Mahboub, H. Pai, Z. Patel, N. Pietralla, P. H. Regan, L. G. Sarmiento, O. Wieland, E. Wilson, B. Birkenbach, B. Bruyneel, I. Burrows, L. Charles, E. Clément, F. C. L. Crespi, D. M. Cullen, P. Désesquelles, J. Eberth, V. González, T. Habermann, L. Harkness-Brennan, H. Hess, D.

S. Judson, A. Jungclaus, W. Korten, M. Labiche, A. Maj, D. Mengoni, D. R. Napoli, A. Pullia, B. Quintana, G. Rainovski, P. Reiter, M. D. Salsac, E. Sanchis, and J. J. Valiente Dóbon.
Role of the Δ Resonance in the Population of a Four-Nucleon State in the ^{56}Fe → ^{54}Fe Reaction at Relativistic Energies.
Phys. Rev. Lett. 117, 222302 (2016).

M. Lettmann, V. Werner, N. Pietralla, P. Doornenbal, A. Obertelli, T.R. Rodríguez, K. Sieja, G. Authelet, H. Baba, D. Calvet, F. Château, S. Chen, A. Corsi, A. Delbart, J.-M. Gheller, A. Giganon, A. Gillibert, V.Lapoux, T. Motobayashi, M. Niikura, N. Paul, J.-Y. Roussé, H. Sakurai, C. Santamaria, D. Steppenbeck, R. Taniuchi, T. Uesaka, T. Ando, T. Arici, A. Blazhev, F. Browne, A. Bruce, R. Carroll, L.X. Chung, M.L. Cortés, M. Dewald, B. Ding, F. Flavigny, S. Franchoo, M. Górska, A. Gottardo, A. Jungclaus, J. Lee, B.D. Linh, J. Liu, Z. Liu, C. Lizarazo, S. Momiyama, K. Moschner, S. Nagamine, N. Nakatsuka, C.R. Nita, C. Nobs, L. Olivier, Z. Patel, Zs. Podolyák, M. Rudigier, T. Saito, C. Shand, P.-A. Söderström, I. Stefan, V. Vaquero, K. Wimmer, and Z. Xu.
Triaxiality of neutron-rich ^{84,86,88}Ge from low-energy nuclear spectra.
Phys. Rev. C 96, 011301(R) (2017).

N. Paul, A. Corsi, A. Obertelli, P. Doornenbal, G. Authelet, H. Baba, B. Bally, M. Bender, D. Calvet, F. Château, S. Chen, J.-P. Delaroche, A. Delbart, J.-M. Gheller, A. Giganon, A. Gillibert, M. Girod, P.H. Heenen, V. Lapoux, J. Libert, T. Motobayashi, M. Niikura, T. Otsuka, T.R. Rodríguez, J.-Y. Roussé, H. Sakurai, C. Santamaria, N. Shimizu, D. Steppenbeck, R. Taniuchi, T. Togashi, Y. Tsunoda, T. Uesaka, T. Ando, T. Arici, A. Blazhev, F. Browne, A.M. Bruce, R. Carroll, L.X. Chung, M.L. Cortés, M. Dewald, B. Ding, F. Flavigny, S. Franchoo, M. Górska, A. Gottardo, A. Jungclaus, J. Lee, M. Lettmann, B.D. Linh, J. Liu, Z. Liu, C. Lizarazo, S. Momiyama, K. Moschner, S. Nagamine, N. Nakatsuka, C.R. Nita, C.R. Nobs, L. Olivier, Z. Patel, Zs. Podolyák, M. Rudigier, T. Saito, C . Shand, P.-A. Söderström, I. Stefan, V. Vaquero, V. Werner, K. Wimmer, and Z. Xu.
Are There Signatures of Harmonic Oscillator Shells Far from Stability? First Spectroscopy of ^{110}Zr.
Phys. Rev. Lett. 118, 032501 (2017).

C. Stahl, J. Leske, M. Lettmann, N. Pietralla.
APCAD-Analysis program for the continuous-angle DSAM.
Computer Physics Communications 214, 174 (2017).

R. Stegmann, C. Stahl, G. Rainovski, N. Pietralla, C. Stoyanov, M.P. Carpenter, R.V.F. Janssens, M. Lettmann, T. Möller, O. Möller, V. Werner, S. Zhu.
Identification of the one-quadrupole phonon $2^+_{1,ms}$ state of ^{204}Hg.
Physics Letters B 770, 77 (2017).

S. Chen, P. Doornenbal, A. Obertelli, T. R. Rodríguez, G. Authelet, H. Baba, D. Calvet, F. Château, A. Corsi, A. Delbart, J.-M. Gheller, A. Giganon, A. Gillibert, V. Lapoux, T. Motobayashi, M. Niikura, N. Paul, J.-Y. Roussé, H. Sakurai, C. Santamaria, D. Steppenbeck, R. Taniuchi, T. Uesaka, T. Ando, T. Arici, A. Blazhev, F. Browne, A. M. Bruce, R. Caroll, L. X. Chung, M. L. Cortés, M. Dewald, B. Ding, F. Flavigny, S. Franchoo, M. Górska, A. Gottardo, A. Jungclaus, J. Lee, M. Lettmann, B. D. Linh, J. Liu, Z. Liu, C. Lizarazo, S. Momiyama, K. Moschner, S. Nagamine, N. Nakatsuka, C. R. Nita, C. Nobs, L. Olivier, R. Orlandi, Z. Patel, Zs. Podolyak, M. Rudigier, T. Saito, C. Shand, P.-A. Söderström, I. Stefan, V. Vaquero, V. Werner, K. Wimmer, Z. Xu.
Low-lying structure and shape evolution in neutron-rich Se isotopes.
Phys. Rev. C 95, 041302(R) (2017).

F. Flavigny, P. Doornenbal, A. Obertelli, M. P. Delaroche, M. Girod, J. Libert, T.R. Rodríguez, G. Authelet, H. Baba, D. Calvet, F. Château, S. Chen, A. Corsi, A. Delbart, J.-M. Gheller, A. Giganon, A. Gillibert, V. Lapoux, T. Motobayashi, M. Niikura, N. Paul, J.-Y. Roussé, H. Sakurai, C. Santamaria, D. Steppenbeck, R. Taniuchi, T. Uesaka, T. Ando, T. Arici, A. Blazhev, F. Browne, A. Bruce, R. Carroll, L.X. Chung, M.L Cortés, M. Dewald, B. Ding, S. Franchoo, M. Górska, A. Gottardo, A. Jungclaus, J. Lee, M. Lettmann, B. D. Linh, J. Liu, Z. Liu, C. Lizarazo, S. Momiyama, K. Moschner, S. Nagamine, N. Nakatsuka, C. R. Nita, C. Nobs, L. Olivier, R. Orlandi, Z. Patel, Zs. Podolyák, M. Rudigier, T. Saito, C. Shand, P.-A. Söderström, I. Stefan, V. Vaquero, V. Werner, K. Wimmer, and Z. Xu.
Shape Evolution in Neutron-Rich Krypton Isotopes Beyond $N = 60$: First Spectroscopy of ^{98,100}Kr.
Phys. Rev. Lett. 118, 242501 (2017).

C.M. Shand, Zs. Podolyák, M. Górska, P. Doornenbal, A. Obertelli, F. Nowacki, T. Otsuka, K. Sieja, J.A. Tostevin, Y. Tsunoda, G. Authelet, H. Baba, D. Calvet, A. Château, S. Chen, A. Corsi, A. Delbart, J.M. Gheller, A. Giganon, A. Gillibert, T. Isobe, V. Lapoux, M. Matsushita, S. Momiyama, T. Motobayashi, M. Niikura, H. Otsu, N. Paul, C. Péron, A. Peyaud, E. C. Pollacco, J.-Y. Roussé, H. Sakurai, C. Santamaria, M. Sasano, Y. Shiga, D. Steppenbeck, S. Takeuchi, R. Taniuchi, T. Uesaka, H. Wang, K. Yoneda, T. Ando, T. Arici, A. Blazhev, F. Browne, A. M. Bruce, R. J. Carroll, L. X. Chung, M.L. Cortés, M. Dewald, B. Ding, Zs. Dombrádi, F. Flavigny, S. Franchoo, F. Giacoppo, A. Gottardo, K. Hadynska-Klek, A. Jungclaus, Z. Korkulu, S. Koyama, Y. Kubota, J. Lee, M. Lettmann, B. D. Linh, J. Liu, Z. Liu, C. Lizarazo, C. Louchart, R. Lozeva, K. Matsui, T. Miyazaki, K. Moschner, M. Nagamine, N. Nakatsuka, S. Nishimura, C. R. Nita, C. R. Nobs, L. Olivier, S. Ota, R. Orlandi, Z. Patel, P. H. Regan, M. Rudigier, E. Sahin, T. Saito, P.-A. Söderström, I. Stefan, T. Sumikama, D. Suzuki, Zs. Vajta, V. Vaquero, V. Werner, K. Wimmer, J. Wu, Z. Y. Xu.
Shell evolution beyond $Z = 28$, $N = 50$: Spectroscopy of ^{81,82,83,84}Zn.
Physics Letters B 773, 492 (2017).

L. Olivier, S. Franchoo, M. Niikura, Z. Vajta, D. Sohler, P. Doornenbal, A. Obertelli, Y. Tsunoda, T. Otsuka, G. Authelet, H. Baba, D. Calvet, F. Château, A. Corsi, A. Delbart, J.-M. Gheller, A. Gillibert, T. Isobe, V. Lapoux, M. Matsushita, S. Momiyama, T. Motobayashi, H. Otsu, C. Péron, A. Peyaud, E. C. Pollacco, J.-Y. Roussé, H. Sakurai, C. Santamaria, M. Sasano, Y. Shiga, S. Takeuchi, R. Taniuchi, T. Uesaka, H. Wang, K. Yoneda, F. Browne, L. X. Chung, Z. Dombradi, F. Flavigny, F. Giacoppo, A. Gottardo, K. Hadynska-Klek, Z. Korkulu, S. Koyama, Y. Kubota, J. Lee, M. Lettmann, C. Louchart, R. Lozeva, K. Matsui, T. Miyazaki, S. Nishimura, K. Ogata, S. Ota, Z. Patel, E. Sahin, C. Shand, P.-A. Söderström, I. Stefan, D. Steppenbeck, T. Sumikama, D. Suzuki, V. Werner, J. Wu, Z. Xu.
Persistence of the $Z = 28$ Shell Gap Around ^{78}Ni: First Spectroscopy of ^{79}Cu.
Phys. Rev. Lett. 119, 192501 (2017).

N. Lalovic, D. Rudolph, Zs. Podolyak, L. Sarmiento, E. C. Simpson, T. Alexander, M. L. Cortes Sua, J. Gerl, P. Golubev, F. Ameil, T. Arici, C. Bauer, D. Bazzacco, M. A Bentley, P. Boutachkov, M. Bowry, C. Fahlander, A. Gadea, J. Gellanki, A. Givechev, N. Goel, M. Gorska, A. Gottardo, E. Gregor, G. Guastalla, T. Habermann, M. Hackstein, A. Jungclaus, I. Kojouharov, R. Kumar, N. Kurz, M. Lettmann, C. Lizarazo, C. Louchart-Henning, E. Merchan, C. Michelagnoli, T. Moeller, K. Moschner, Z. Patel, N. Pietralla, S. Pietri, D. Ralet, M. Reese, P. H. Regan, P. Reiter, H. Schaffner, P. P. Singh, C. Stahl, R. Stegmann, O. Stézowski, J. Taprogge, P. Thoele, A. Wendt,

O. Wieland, E. Wilson, R. Wood, H.-J. Wollersheim, B. Birkenbach, B. Bruyneel, I. Burrows, E. Clement, P. Desesquelles, C. Domingo-Pardo, J. Eberth, V. G. Millan, H. Hess, J. Jolie, D. Judson, R. Menegazzo, D. Mengoni, D. Napoli, A. Pullia, B. Q. Arnes, G. I. Rainovski, M.-D. Salsac, E. Sanchis, J. Simpson, J. J. Valiente Dobón
Study of Isomeric States in ^{198,200,202,206}Pb and ^{206}Hg Populated in Fragmentation Reactions.
Journal of Physics G (Accepted Manuscript online 23 January 2018).

Publications in conference proceedings

T. Alexander, Zs. Podolyak, M. L. Cortes, J. Gerl, D. Rudolph, L. Sarmiento, F. Ameil, T. Arici, D. Bazzacco, Ch. Bauer, M. A. Bentley, A. Blazhev, M. Bowry, P. Boutachkov, R. Carroll, C. Fahlander, A. Gadea, J. Gellanki, W. Gelletly, A. Givechev, N. Goel, P. Golubev, M. Gorska, A. Gottardo, E. Gregor, G. Guastalla, T. Habermann, M. Hackstein, A. Jungclaus, I. Kojouharov, W. Korten, S. Kumar, N. Kurz, N. Lalovic, M. Lettmann, C. Lizarazo, C. Louchart, S. Mandal, E. Merchan, C. Michelagnoli, Th. Moeller, K. Moschner, Z. Patel, N. Pietralla, S. Pietri, D. Ralet, M. Reese, P. H. Regan, P. Reiter, H. Schaffner, P. Singh, C. Stahl, R. Stegmann, O. Stezowksi, J. Taprogge, P. Thoele, P. M. Walker, O. Wieland, A. Wendt, E. Wilson, R. Wood, H.-J. Wollersheim.
Isomeric Ratios in ^{206}Hg.
Acta Physica Polonica. Series B 46, 601 (2015)

D. Kocheva, R. Stegmann, G. Rainovski, J. Jolie, N. Pietralla, C. Stahl, P. Petkov, A. Blazhev, A. Hennig, C. Bauer, Th. Braunroth, M.P. Carpenter, L. Cortes, A. Dewald, M. Djongolov, C. Fransen, K. Gladnishki, R.V.F. Janssens, V. Karayonchev, M. Lettmann, C.J. Lister, J. Litzinger, Th. Möller, C. Möller-Gatermann, M. Scheck, Ph. Scholz, C. Schramm, P. Thöle, V. Werner, D. Wölk, S. Zhu and P. Van Isacker.
Search for mixed-symmetry states of nuclei in the vicinity of the double-magic nucleus ^{208}Pb.
EPJ Web of Conferences 107, 03004 (2016).

V. Werner, C. Santamaria, C. Louchart, A. Obertelli, P. Doornenbal, F. Nowacki, G. Authelet, H. Baba, D. Calvet, F. Château, A. Corsi, A. Delbart, J.-M. Gheller, A. Gillibert, T. Isobe, V. Lapoux, M. Matsushita, S. Momiyama, T. Motobayashi, M. Niikura, H. Otsu, C. Péron, A. Peyaud, E.C. Pollacco, J.-Y. Roussé, H. Sakurai, M. Sasano, Y. Shiga, S. Takeuchi, R. Taniuchi, T. Uesaka, H. Wang, K. Yoneda,

F. Browne, L.X. Chung, Zs. Dombradi, S. Franchoo, F. Giacoppo, A. Gottardo, K. Hadynska-Klek, Z. Korkulu, S. Koyama, Y. Kubota, J. Lee, M. Lettmann, R. Lozeva, K. Matsui, T. Miyazaki, S. Nishimura, L. Olivier, S. Ota, Z. Patel, N. Pietralla, E. Sahin, C. Shand, P.-A. Söderström, I. Stefan, D. Steppenbeck, T. Sumikama, D. Suzuki, Zs. Vajta, J. Wu and Z. Xu.
Collectivity of neutron-rich Cr and Fe toward $N = 50$.
EPJ Web of Conferences 107, 03007 (2016).

R. Stegmann, C. Stahl, G. Rainovski, N. Pietralla, T. Möller, M. Lettmann, R. V. F. Janssens, M. Carpenter and S. Zhu.
Investigation of the mixed-symmetric one-quadrupole phonon $2^+_{1,ms}$ state of the heavy nucleus ^{204}Hg.
Journal of Physics: Conference Series 724, 012047 (2016).

M. L. Cortés, P. Doornenbal, A. Obertelli, N. Pietralla, V. Werner, G. Authelet, H. Baba, D. Calvet, F. Château, A. Corsi, A. Delbart, J.-M. Gheller, A. Gillibert, T. Isobe, V. Lapoux, C. Louchart, M. Matsushita, S. Momiyama, T. Motobayashi, M. Niikura, H. Otsu, C. Péron, A. Peyaud, E. C. Pollacco, J.-Y. Roussé, H. Sakurai, C. Santamaria, M. Sasano, Y. Shiga, S. Takeuchi, R. Taniuchi, T. Uesaka, H. Wang, K. Yoneda, F. Browne, L. X. Chung, Zs. Dombradi, S. Franchoo, F. Giacoppo, A. Gottardo, K. Hadynska-Klek, Z. Korkulu, S. Koyama, Y. Kubota, J. Lee, M. Lettmann, R. Lozeva, K. Matsui, T. Miyazaki, S. Nishimura, L. Olivier, S. Ota, Z. Patel, E. Sahin, C. M. Shand, P.-A. Söderström, I. Stefan, D. Steppenbeck, T.Sumikama, D. Suzuki, Zs. Vajta, J. Wu and Z. Xu.
Inelastic scattering of ^{72,74}Ni off a proton target.
Journal of Physics: Conference Series 724, 012008 (2016).

Acknowledgements

Auch wenn eine Doktorarbeit die Arbeit eines Einzelnen widerspiegelt, haben viele Personen zu ihrem Gelingen beigetragen. Ihnen soll an dieser Stelle gedankt werden.

Zuerst möchte ich mich bei Norbert Pietralla dafür bedanken, dass er mich in seine Arbeitsgruppe aufgenommen hat und mir diese Arbeit ermöglichte. Ich bin Ihm sehr dankbar, dass er sich immer Zeit für meine Anliegen und Fragen nahm. Durch seine Begeisterung für die Kernphysik war er mir zu jeder Zeit Antrieb und Ansporn.

Ein besonderer Dank gilt Christian, der mich am ersten Tag im Institut an die Hand nahm. Die energischen Diskussion über Arbeit sowie Alltag haben mich stets weiter gebracht. Gerne denke ich an gemeinsame Erlebnisse auf Strahlzeiten und Konferenzen zurück.

Für wertvolle Ratschläge und viele arbeitsbezogene sowie private Gespräche/Diskussionen und dafür, dass sie immer ein offenes Ohr für mich hatten, möchte ich mich bei Oliver und Volker bedanken.

Zu Beginn meines Studiums lernte ich Christina, Johann und Torsten kennen. Mit ihnen, der sogenannten "Bachelorgang", habe ich bis zum heutigen Tag alle Höhen und Tiefen des Studiums durchlebt. Ich bin froh, sie zu meinen Freunden zählen zu können.

Meinen Kollegen aus Raum 210 (dieser ist unschwer an der Giraffe auf dem Türschild zu erkennen) bin ich nicht zuletzt für das angenehme Arbeitsklima sehr dankbar. Mit Cesar, Liliana und Waldemar war es immer möglich, über aktuelle Themen beruflich sowie privat zu sprechen.

Viele prägende Erfahrungen und Eindrücke konnte ich auf verschiedenen Strahlzeiten und Konferenzen sammeln. Diese Erlebnisse teilte ich unter anderem mit Johannes, Marcus, P.-A., Pavlos, Robert und Thomas. Vielen Dank für diese Zeit.

Für die angenehme Arbeitsatmosphäre bin ich der gesamten Arbeitsgruppe sehr dankbar. Namentlich möchte ich mich bei Andreas, Antonio, Lars, Philipp N., Ruben, Ralph, Tobias B. und Tobias K. für die Einblicke in ihren Themenbereich, durch regelmäßige Gespräche, bedanken.

Für das Korrekturlesen meiner Arbeit ein herzliches Dankeschön an: Jessica, Johann, Johannes, Michael, Oliver, Pavlos, Tomas, Vanessa, Volker und Waldemar.

Nicht zuletzt möchte ich mich besonders bei meiner Familie bedanken. Meine Großeltern Edith und Gerhard sowie Gretel und Walter, meine Eltern Birgit

und Christian, mein Bruder Michael und meine Freundin Jessica haben mich in jeder Situation meines beruflichen Wertegangs unterstützt und mir Mut gemacht. Speziell in schwierigen Situationen haben sie für den nötigen Ausgleich gesorgt und mich wieder "auf Kurs" gebracht.

Diese Arbeit wurde durch die finanzielle Unterstützung des BMBF unter der Fördernummer 05P15RDFN1 ermöglicht.

Lebenslauf

Persönliche Daten

Name	Marc Lettmann
Geburtsdatum	02.08.1985
Geburtsort	Darmstadt
Staatsangehörigkeit	deutsch
Familienstand	ledig

Schulausbildung

1992 - 1996	Mittelpunktschule Gadernheim
1996 - 2006	Altes Kurfürstliches Gymnasium Bensheim
2006	Abitur

Zivildienst

2006 - 2007	Hessisches Forstamt Groß-Gerau Revierförsterei Kühkopf-Knoblochsaue

Hochschulausbildung

2007 - 2011	TU Darmstadt B.Sc. Physik *Entwicklung eines Tracking-Algorithmus für das DAGATA-Polarimeter durch Analyse simulierter Daten*
2011 - 2013	TU Darmstadt M.Sc. Physik *Differentielle, winkelkontinuierliche DSAM für relativistische Ionenstrahlen*
seit September 2013	TU Darmstadt Promotionsstudium Arbeitsgruppe Prof. Dr. Dr. h.c. N. Pietralla

Erklärung zur Dissertation

Hiermit versichere ich, die vorliegende Dissertation ohne Hilfe Dritter nur mit den angegebenen Quellen und Hilfsmitteln angefertigt zu haben. Alle Stellen, die aus Quellen entnommen wurden, sind als solche kenntlich gemacht. Diese Arbeit hat in gleicher oder ähnlicher Form noch keiner Prüfungsbehörde vorgelegen.

Darmstadt, den 1.2.2018

(Marc Lettmann, M.Sc.)